On the Estimation of Exhaust Gas Recirculation Flow and Waste Heat Recovery Tradeoffs Based on Differential Pressure Measurements

by

Rani Kiwan

A dissertation submitted in partial fulfillment
of the requirements for the degree of
Doctor of Philosophy
(Mechanical Engineering)
in The University of Michigan
2019

Doctoral Committee:

Professor Anna Stefanopoulou, Chair
Professor Andre Boehman
Professor Heath Hofmann
Assistant Research Scientist Robert Middleton

Rani Kiwan

rkiwan@umich.edu

ORCID iD: 0000-0002-9429-5211

PREFACE

The EGR estimation work was funded and supported by Ford Motor Company.

The information, data, or work presented herein was funded in part by the Advanced Research Projects Agency-Energy (ARPA-E), U.S. Department of Energy, under Award Number DE-AR0000659. The views and opinions of authors expressed herein do not necessarily state or reflect those of the United States Government or any agency thereof.

TABLE OF CONTENTS

LIST OF FIGURES

Figure

LIST OF TABLES

Table

ABSTRACT

Both exhaust gas recirculation (EGR) and waste heat recovery (WHR) are attractive technologies for more efficient spark ignition (SI) engines. The fuel economy (FE) benefit of cooled external EGR on SI engines is well established, and preliminary 1^{st} law analysis of engine energy flows indicates the large potential for efficiency improvements with WHR. Nevertheless, both technologies face major challenges that need to be addressed to become viable solutions for more efficient SI engines.

Cooled external EGR improves SI engine efficiency under wide range of conditions. However, inaccurate estimation of the EGR fraction in the intake manifold can be detrimental as it can lead to inaccurate air charge estimation, knock and misfire. Accurate EGR estimation based on a differential pressure (ΔP) measurement is needed but currently very challenging at the low ΔP's due to pressure pulsations and inertial effects. While some systems are capable of increasing ΔP across the EGR valve or EGR orifice to improve EGR estimation, the higher ΔP is undesirable as it can increase pumping losses and force EGR valve operation at lower lifts leading to harder valve actuation and control. EGR estimation accuracy at low ΔP can be improved by fast sampling of the ΔP signal and using the newly derived approximations of the unsteady compressible flow orifice equation. Both experimental data from a modified Ford 1.6 L EcoBoost engine with added LP and HP-EGR loops, and simulation predictions from its GT-Power models are used to evaluate the estimation methods. A sampling frequency of at least 1 kHz reduces the $\overline{\Delta P}$ lower bound required to keep the LP and HP-EGR estimation error within a target $\pm 1\%$ from 12.7 and 27.9 to 1.9 and 2.9 kPa respectively. The LP $\overline{\Delta P}$ lower bound can be further reduced to 1.1 kPa with variable filtering, but the sampling frequency requirement is increased to ≈ 3 kHz to achieve the full benefit.

The impact of gauge-line distortions and EGR valve area offset errors are also evaluated. An extension of a preexisting lumped parameter model is proposed to estimate the actual ΔP from the distorted measurement. Simulation results show that the proposed model is able to correct for the gauge-line errors under modeled pressure measurement noise. Valve area offset errors are shown to have substantial

impact on the EGR estimation error especially for the HP-EGR case. A novel online calibration method for the HP-EGR valve area using preexisting engine sensors is developed and shown to have promise for implementation.

The second part of this thesis studies the limitations and challenges of WHR through electric turbo-generation. Insights into the tradeoffs between exhaust energy recovery and increased pumping losses from the flow restriction of the electric turbo-generator (eTG) are provided and assessed using thermodynamic principles and with a detailed GT-Power engine model. The additional pumping losses are load independent and cannot be offset by the eTG power at low loads. Engine simulations are used to predict the influence of the increased back pressure on pumping work, in-cylinder residuals and combustion. The eTG is detrimental at the high loads as it requires more spark retard to mitigate the increased knocking tendency. The eTG benefit is therefore restricted to mid-loads. The reduction in fuel consumption (FC) possible over various drive cycles is estimated based on the steady-state efficiency of frequently visited operating points assuming all recovered energy can be reused at a representative engine efficiency. Fuel consumption reductions of $\approx 1.2\%$ are projected for the combined cycle.

CHAPTER I

Introduction

1.1 Background

Light duty vehicles account for 60% of the Greenhouse Gas (GHG) emissions of the transportation sector [1], which in turn, is responsible for 27% of all GG emissions in the U.S [2]. In Europe, the transportation sector is also responsible for 27% of GG emissions with 72% of these emissions coming from road vehicles [3]. Regulating the Greenhouse Gas emissions, or alternatively, the fuel economy (FE) of passenger vehicles is an integral part to fighting and reducing the impact of climate change. The Corporate Average Fuel Economy (CAFE) standards sets the fleet FE target for new passenger vehicles sold in the US by 2025 at 54.5 mpg - nearly double of 2010's 27.5 mpg target [1]. Higher fuel economy targets also apply to new vehicles sold in Europe [4]. An overview of worldwide fuel economy regulations can be found elsewhere [5].

With the internal combustion engine (ICE) projected to be a part of most vehicle powertrains in the near future [5, 6], advanced engine solutions and concepts play an important role in achieving the challenging future FE targets. The engine technologies currently being researched are numerous and span various fields [7]. This thesis will focus on some of the challenges facing two of the advanced engine concepts: external external exhaust gas recirculation (EGR) and waste heat recovery (WHR) on spark ignited (SI) engines. The FE benefit of cooled external EGR on SI-ICE is verified through simulations and experiments by several works in the literature [8–14], while preliminary 1st law analysis of engine energy flows indicates the large potential for efficiency improvements with WHR given that 30 to 37% of the fuel energy is lost in the exhaust [15]. Nevertheless, both technologies face major challenges resulting in limited market penetration onto production SI engines. The challenge of accurate EGR estimation prevents achieving the full EGR FE benefit, and previous studies

of WHR on light duty engines do not show considerable FE gains on relevant drive cycles [16, 17].

1.2 Exhaust Gas Recirculation Challenges

In order to meet the current FE targets, production SI engines are progressively being downsized and turbocharged. The smaller displacement reduces pumping and relative frictional losses, while turbocharging increases the engine power density to compensate for the reduced displacement and maintain engine performance. Unfortunately, the extent of feasible downsizing and boosting is constrained in part by spark knock. Knock can be mitigated by retarding the spark timing, and the higher exhaust temperatures resulting from the retarded combustion phasing can be avoided through fuel enrichment. However, both sub-optimal combustion phasing and fuel enrichment penalize efficiency [8, 13, 14].

While internal EGR is found to increase the knocking tendency as a result of its high temperature [18], several studies have shown the knock mitigation properties of cooled external EGR [8–14]. Kumano *et al.* [10] reported a half crank-angle (CA) degree advance of the 50% burn crank-angle (CA_{50}) for every 1% of cooled EGR added at the knock-limited regions; smaller knock mitigation benefits can be observed at the very high loads [19]. In addition to its knock mitigating benefits improving the combustion phasing, cooled EGR also reduces the exhaust gas temperature decreasing the need of fuel enrichment [8–14]. Cooled external EGR can be also used to reduce pumping losses at lower loads, but this can be achieved though internal EGR as well. As result, fuel consumption improvements up to 5% are reported in the literature [9, 12]. Alternatively, cooled EGR can permit more aggressive downsizing, further shifting the typical engine operation into more efficient regions [13].

External EGR can be implemented through a low pressure (LP) or high pressure (HP) system on turbocharged engines. A LP configuration has EGR taken downstream of the turbocharger turbine and reintroduced upstream of the turbocharger compressor. On a HP system, the EGR extraction and introduction points are instead pre-turbine and post-throttle respectively. Zhong *et al.* [20] reported that LP-EGR is more suitable at the low engine speeds prevalent under normal driving conditions, whereas the HP configuration is the better alternative at higher RPM's. With a HP-EGR system, EGR introduction requires higher compressor pressure ratios at the same compressor flows. This can move the compressor operation closer or into the surge regions. This limitation is reduced

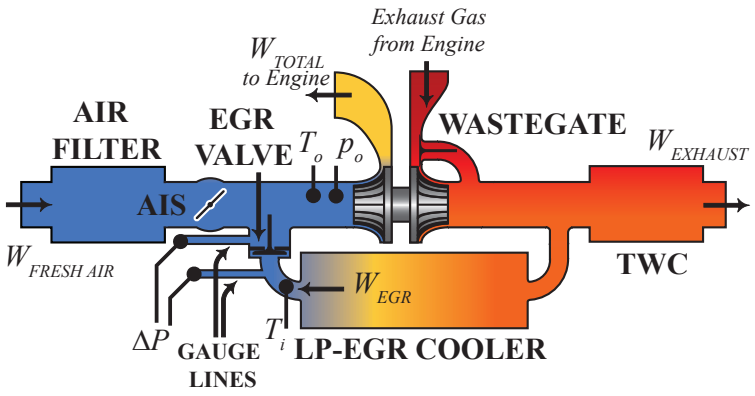

Figure 1.1: LP-EGR configuration showing the flow rates and sensor measurements of interest.

with LP-EGR as the compressor flow is increased with EGR along with the increased pressure ratio. However, an increased compressor flow is undesirable at higher speeds as it brings the compressor operation closed to choking making a HP system the more convenient option.

Regardless of the configuration, miscalculation of EGR fraction can be detrimental to engine efficiency and emissions. EGR estimation errors result in air-charge estimation errors which impact emissions control. A 1% EGR error leads to an additional 1 to 1.33% equivalence ratio error on top of the preexisting errors during transients for EGR percentages between 0 and 25% respectively; the resulting cumulative error can exceed the acceptable thresholds to meet emissions. Also, excessive EGR fractions can result in misfire and partial burning [21], and insufficient EGR can cause knock. Therefore, EGR flow must be accurately estimated and controlled. Unfortunately, EGR estimation is problematic and has been a topic of interest in the scientific community for some time. In 1997, Azzoni *et al.* [22] proposed a model for estimating EGR flow rate based on sensors available at the time, and this topic continues to be addressed [23–27]. According to Liu *et al.* [23] and Brewbaker [24], the accuracy of EGR mass flow rate estimations made with the steady orifice equation suffers from the unsteady pulsating nature of the EGR flow along with the typically small pressure differentials (ΔP) across the EGR valve. The distortion of the ΔP signal in pressure gauge-line under pulsating conditions further adds another source of error [28]. On the other hand, solely relying on feedback control through an intake air Oxygen (IAO2) sensor to achieve the desired EGR fraction is

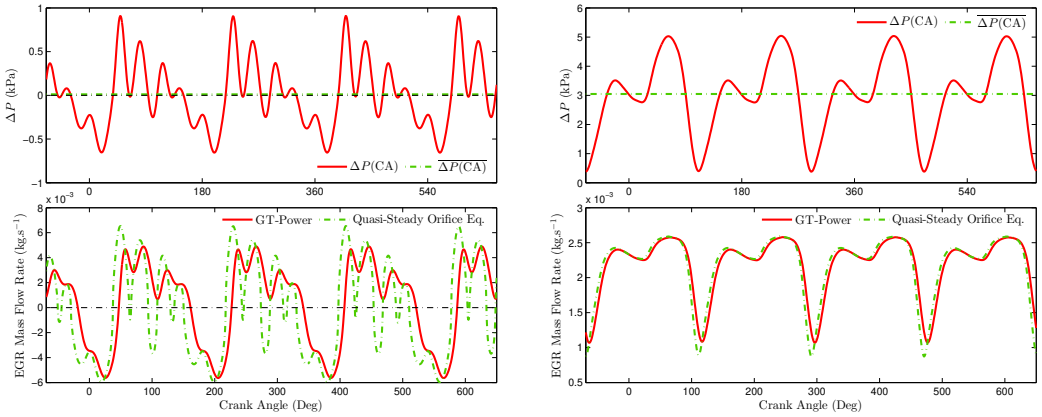

(a) 5.7 mm EGR valve lift and 81° (almost wide open) AIS throttle angle

(b) 0.56 mm EGR valve lift and 6° AIS throttle angle

Figure 1.2: Simulated LP-EGR pressure pulsations and mass flow rates for 2 cases at 2000 RPM and 2 bar BMEP; estimated EGR mass flow rate using a steady orifice equation (quasi-steady) is shown as well.

not possible due to the inherent long transport delays between the EGR valve and the EGR measurement present in a LP system [27]. In a HP system, the measured Oxygen concentrations are susceptible to errors due the presence of fuel in the intake manifold and possible insufficient mixing for a HP system.

The state-of-the-art solution for the EGR estimation problem is to introduce a larger ΔP across the EGR valve. This can be achieved by throttling the air intake system (AIS) on a LP-EGR system (Fig. 1.1), and is shown to considerably improve the LP-EGR percentage estimate [23, 24]. Fig. (1.2) shows the simulated pressure pulsations and EGR mass flow rate for two sample cases[1]. Both correspond to the same engine speed and load: 2000 RPM and 2 bar BMEP. The estimated EGR flow based on the crank-angle (CA) resolved ΔP signal using the quasi-steady compressible flow orifice equation is presented as well. Fig. (1.2(a)) depicts a case with a near wide open air intake system (AIS) throttle, resulting in a near-zero averaged differential pressure ($\overline{\Delta P}$) across the EGR valve ($\approx$ 0.01 kPa) and significant pulsations of $\approx$ 1.6 kPa, peak to trough. It can be seen that the mass flow rate reversal lags behind the ΔP sign reversal due to the flow inertia (e.g. at $\approx 400°$ CA). In some cases, the sign reversal of ΔP is not followed by a mass flow reversal (e.g. at $\approx 450°$ CA). However, this inertial effect is not captured by the quasi-steady compressible orifice equation, resulting in a 6.2% error in the estimated percentage of EGR (Fig. (1.2(a))).

[1]The simulation details are presented in Chapter II.

Throttling the AIS to 6° increased $\overline{\Delta P}$ to $\approx$ 3 kPa and significantly reduced the ratio of the pressure pulsation peak-to-peak amplitude to $\overline{\Delta P}$ (Fig. (1.2(b))). A better agreement between the simulated and estimated EGR mass flow rate is observed in this case, which lacks flow reversal with an estimated EGR error of 0.35%.

While the additional throttling can provide sufficient EGR estimation accuracy to avoid poor emissions control, it can increase the engine pumping losses reducing the overall FE benefit. On a HP-EGR system, the $\overline{\Delta P}$ can be increased by simultaneously throttling the turbine wastegate and engine throttle body resulting in additional pumping losses. The increase in pumping mean effective pressure (ΔPMEP) is approximately the same as the required $\overline{\Delta P}$ increase across the HP-EGR valve. The percent relative engine efficiency loss can then be approximated as 100ΔPMEP/BMEP. A relative efficiency loss of $\approx$ 0.1 and $\approx$ 0.067% per 1 kPa of additional HP-EGR valve $\overline{\Delta P}$ is expected at loads between $\approx$ 10 and $\approx$ 15 bar BMEP where the EGR valve $\overline{\Delta P}$ is the lowest and the HP-EGR estimation is most problematic.

On a LP-EGR system, the increased $\overline{\Delta P}$ across the LP-EGR valve is accompanied by an increase in the engine throttle body opening under throttled conditions. Both intake and exhaust manifold pressures are maintained resulting in no additional pumping losses. Under boosted conditions however, the turbocharger compressor is required to do more work to provide the same boost with a throttled AIS. Pumping losses are increased as a higher exhaust pressure is required to achieve the same intake manifold pressure. The ΔP across the turbocharger compressor (ΔP_{COMP}) increases by same amount as the required increase in the LP-EGR $\overline{\Delta P}$; the resulting increase in the ΔP across the turbocharger turbine (ΔP_{TURB}) is a function of the turbocharger efficiency. Fig. (1.3(a)) shows the ratio of the ΔP_{TURB} to ΔP_{COMP} for the 1.6 L Ford EcoBoost engine obtained from experimental data. The percent relative engine efficiency loss can be estimated as 100ΔPMEP/BMEP where ΔPMEP $\approx \Delta P_{TURB}$. Fig. (1.3(b)) shows relative engine efficiency losses between $\approx$ 0.1 and $\approx$ 0.05% per 1 kPa increase in LP-EGR valve $\overline{\Delta P}$ in the boosted region.

Furthermore, imposing a larger ΔP across the EGR valve requires smaller EGR valve lifts and therefore more challenging valve actuation. Another possible approach to tackle the EGR estimation problem is by being conservative with the desired EGR percentage and/or amount of spark advance such that unstable combustion and knock are avoided in case of under-estimating and over-estimating respectively. This solution may not address the impact of EGR estimation error on air-charge estimation and emissions control. Similar to increasing EGR ΔP, this solution does not allow

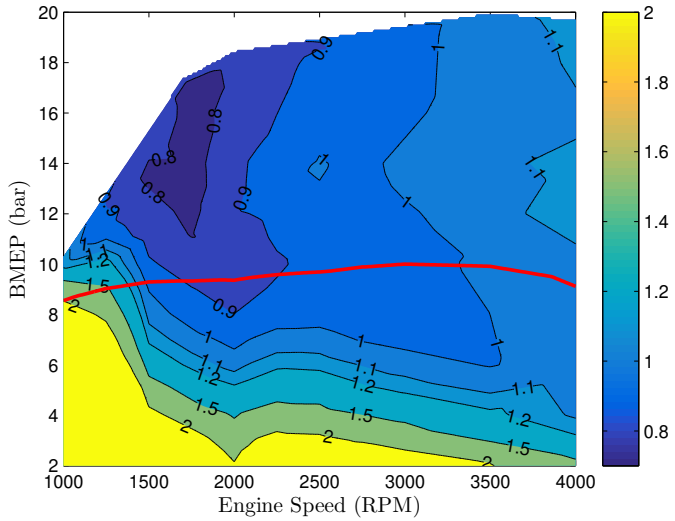

(a) Turbine ΔP to compressor ΔP ratio

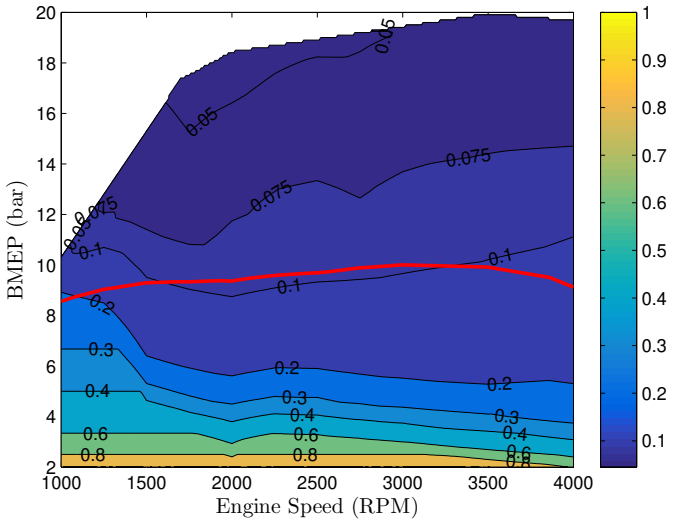

(b) Relative efficiency loss (%) per additional 1 kPa $\overline{\Delta P}$ across the LP-EGR valve

Figure 1.3: (a) Ratio of ΔP across the TC turbine to ΔP across the compressor, and (b) percent relative efficiency loss due to a 1 kPa increase in LP-EGR valve $\overline{\Delta P}$ for a 1.6 L Ford EcoBoost engine. The red lines correspond to the boundary above which the engine is boosted.

us to exploit the maximum possible benefit of cooled external EGR.

In order to achieve the full FE benefit of EGR, it is desirable to improve the EGR estimation accuracy under minimal EGR differential pressures instead of increasing the ΔP across the EGR valve as recommended in the literature [23, 24]. The possibility of reducing the EGR valve ΔP without sacrificing estimation accuracy is investigated in this work.

1.3 Waste Heat Recovery Challenges

With engine exhaust gases accounting for 30 to 37% of the fuel energy [15], exhaust waste heat recovery (WHR) seems to be one aspect of the internal combustion engine with the potential of significant efficiency gains. While traditional turbochargers (TC) capture part of the waste heat in the exhaust, the amount of recovered energy at a given engine operating point is restricted by the compressor power demand to meet the desired load. The attempt to recover more power through the TC turbine will overspeed the compressor resulting in higher loads than demanded. Therefore, there exists room for additional improvements by implementing more flexible dedicated WHR systems. Several WHR technologies and concepts are available. These include turbo-compounding, Rankine cycles and thermoelectric systems [15, 29, 30]. In addition to exhaust energy, some systems can incorporate heat from the engine coolant for WHR [31]. While little energy can be extracted from thermoelectric systems, Rankine cycles are bulky and harder to package. This makes turbo-compounding the more convenient candidate for light-duty vehicle applications.

WHR though turbo-compounding incorporates a waste heat turbine or expander installed in the exhaust path where exhaust energy is partially recovered through an additional expansion process external to the engine. Mechanical turbo-compounding (MTC) is achieved by the addition of a WHR turbine mechanically or hydraulically coupled to the engine's crankshaft. The use of MTC dates back to the late 1940's when first introduced on aircraft piston engines. Their introduction on heavy-duty commercial vehicles came later during the early 1990's [29]. With mechanical turbo-compounding, the WHR expander operates at a fixed speed-ratio to the crank. This restriction can lead to a non-optimal speed for the WHR turbine, or even add energy to the exhaust gases instead of regeneration under some operating conditions. Electric turbo-compounding, or electric turbo-generation, where the WHR expander is coupled to an electric generator, provides more flexibility over the expander speed. With an electric turbo-generator (eTG), the WHR expander can be operated at more

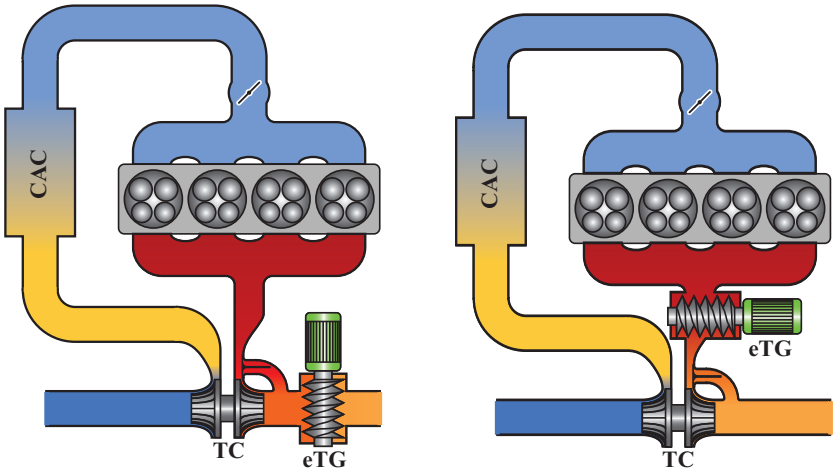

Figure 1.4: Turbocharged engine with *(Left)* Low Pressure eTG and *(Right)* High Pressure eTG.

optimal speeds over the engine operating range (restrictions on the electric machine and expander speeds still apply) [29]. The downside to this approach is however the extra-cost and efficiency losses in the electrical path.

When applied to turbocharged engines, electric turbo-compounding can take various configurations [32]:

1. Serial turbo-compounding where the eTG is added in series with the turbocharger (TC) turbine (Fig. 1.4).

2. Parallel turbo-compounding where the WHR expander is added in parallel to the TC turbine (in the wastegate).

3. Electrically assisted turbo-compounding where an electric machine is attached to the TC shaft.

Turbo-compounding for heavy-duty (HD) diesel engines has been investigated for some time. Various studies reporting fuel consumption benefits up to 6% can be found in the literature [30, 33–36]. Recently, interest in applying the same technology on light-duty applications has surfaced. Briggs *et al.* [37] investigated the benefits of turbo-generation on a 2.4 L turbocharged diesel engine. The WHR turbine was operated at peak efficiency by setting the appropriate generator speed. Up to 3% reduction in brake specific fuel consumption (BSFC) was reported at a selection of frequently visited engine operating points. Lu *et al.* [38] investigated the benefits of mechanical turbo-compounding at full load on a 2.0 L gasoline engine with a variably driven supercharger, and reported reductions in BSFC increasing with engine speed

(up to 8% at 6000 RPM). Mamat *et al.* [39] designed a low pressure turbine for WHR capable of operating at isentropic efficiencies above 70% at low pressure ratios in the vicinity of 1.1. The turbine was operated at a predetermined speed of 50,000 RPM, and its power was maintained at 1kW by controlling the wastegate. BSFC improvements up to 2.73% were observed. Ismail *et al.* [16] showed that turbo-compounding will have a negative impact on a light-duty diesel engine at the urban operating conditions, although WHR gains at the high-speed high-load regions were possible. Dijkstra *et al.* [17] reported no significant fuel savings at frequently visited points during the New European Driving Cycle (NEDC) with turbo-compounding applied to a naturally-aspirated light duty gasoline engine.

Different approaches for operating the WHR expander can be found in the literature. Despite that more than 30% of the fuel energy is lost in the exhaust [15], small improvements and even negative impacts at operating points visited during typical daily driving are reported. A better understanding of the thermodynamic and practical limits of WHR turbo-compounding systems is required to determine the optimal approach to operate the WHR devices, and determine the true potential of the technology.

1.4 Dissertation Contributions

1.4.1 EGR Estimation

- *Determine the optimal pressure sensor configuration for EGR estimation.*

  To estimate the EGR flow using an orifice equation, knowledge of the inlet and outlet valve pressures is needed. Three possible pressure sensor configurations can be used to obtain both pressure readings: (1) inlet and outlet absolute pressure sensors, (2) an inlet absolute pressure sensor and a ΔP sensor and (3) an outlet absolute pressure sensor and a ΔP sensor. The outlet pressure reading can be obtained from existing engine pressure sensors (compressor inltet pressure for LP-EGR and intake manifold pressure for HP-EGR), so option (2) was eliminated as it requires the addition of two new pressure sensors. Option (3), outlet pressure and ΔP sensors, was found to be the optimal configuration as it both requires only one fast-sampled measurement and produces lower EGR estimation errors.

- *Determine the optimal sampling frequency for the ΔP sensor measurement to avoid the non-linearity error with the use of the quasi-steady compressible flow*

orifice equation.

The orifice equation is highly non-linear especially at the low ΔP regions, so fast-sampling of the ΔP signal is required to avoid the non-linearity error. Using GT-Power simulations and experimental studies, the LP and HP-EGR estimation error was evaluated using instantaneous ΔP sampled at different frequencies in comparison to an average ΔP measurement. A sampling frequency of at least 1 kHz was found to eliminate the non-linearity error and reduce the LP and HP $\overline{\Delta P}$ lower bound required to keep the EGR estimation error within a target $\pm 1\%$ from 12.7 and 27.9 to 1.9 and 2.9 kPa respectively.

- *Derive an unsteady compressible flow orifice equation to correct for the inertial error.*

  At $\overline{\Delta P}$'s below $\approx 2-3$ kPa, the use of a quasi-steady orifice equation results in a significant inertial error. An unsteady incompressible flow orifice equation derived from the 1-D momentum equation under the assumption of constant density can be found in the literature [28, 40, 41]. Assuming an isentropic flow instead, an unsteady compressible flow orifice equation was derived to capture the inertial effects present under high pulsating EGR flows. Various assumptions to simplify the newly derived unsteady compressible flow orifice equation were evaluated individually. Simulation results showed that the LP and HP-EGR estimation error can satisfy the target $\pm 1\%$ for all simulated $\overline{\Delta P}$ using the unsteady formulation.

- *Determine the optimal ΔP sensor filtering with the quasi-steady compressible orifice equation that can approximate the unsteady compressible flow orifice equation for less computationally expensive implementation.*

  Estimating the EGR flow using the unsteady orifice equation can be computationally expensive as it involves solving a 1^{st} order non-linear dynamic system. Approximating the unsteady orifice equation using the quasi-steady orifice equation with filtered ΔP was considered. An example of using a lag filter on the pressure signal to mimic the inertial effects while using steady flow formulations or maps can be found in the literature [42]. Grietzer *et al.* [42] introduced a lag in the pressure ratio to account for transient effects in compressors during surge. To investigate if a similar phenomena is observed for pulsating EGR flows, the impact filtering of the ΔP signal on the EGR estimation error was investigated. Both 1^{st} order low pass filters with fixed and variable bandwidths were considered. The

variable bandwidth was shown analytically to be dependent on valve area and ΔP. Experimental data shows that the LP $\overline{\Delta P}$ can be reduced from 1.9 to 1.1 kPa with variable filtering. The sampling frequency requirement was increased to ≈ 3 kHz.

- *Correct for the gauge line distortions of the ΔP measurement by modifying a preexisting lumped parameter model.*

  Pressure sensing lead lines, or gauge-lines, are part of the ΔP measurement systems (Fig. 1.1). These gauge-lines are necessary to protect the ΔP sensor from excessive temperatures, or due to space constraints and packaging restrictions [28]. The impact of gauge-line distortion of the ΔP signal was investigated on the LP-EGR estimation error using GT-Power simulations. The lumped parameter model developed by Nagao and Ikegami [43] to approximate (absolute) pressure distortions in the gauge-lines was extended to correct for gauge-line related distortions of a differential pressure measurement. The modified lumped parameter model was shown to be able to compensate for the gauge-line error under modeled measurement noise.

- *Propose and evaluate a novel approach for HP-EGR valve area online calibration.*

  Changes over time in the valve area due to the accumulation of Carbon deposits can be detrimental to the EGR estimation accuracy. These changes can be modeled as area offset errors. Simulations showed that these offset error are especially detrimental to the EGR estimation error at low valve lifts. Imposing a lower bound on valve lift to avoid low lift operation causing unacceptable EGR estimation errors prevented EGR operation at low to mid-loads for a HP-EGR system. A novel online calibration method for the HP-EGR valve area was developed and assessed. The proposed method does not require additional engine sensors and has the potential to correct for area offset errors.

1.4.2 Waste Heat Recovery

- *Perform an analytical study to provide a better understanding of the intrinsic limitations and behavior of an engine-eTG system.*

  An analytical study using the ideal Otto cycle was conducted to assess the main tradeoff between the recovered energy and increased pumping losses due to the WHR expander. The increase in pumping losses due to the expander's additional back pressure was found to be independent of engine load. On the

other hand, the WHR expander's power was proportional to the engine mass flow rate and exhaust temperature, and therefore, an increasing function of engine load. As a result, there exists a minimum load below which the eTG power (using realistic device efficiencies) is insufficient to offset the additional pumping losses.

It was also observed that the net recovered power (NRP), defined as the difference between the eTG power and the additional pumping, is not necessarily a monotonic function of back pressure. There exists an optimal back pressure at which the eTG's NRP is maximized. Furthermore, the NRP curves at the high loads are truncated and do not exhibit a peak; the maximum NRP is restricted by the engine's ability to maintain the desired load at high back pressures. The optimal eTG operation is a function of how the engine interacts with the eTG, and does not necessarily occur at the WHR expander's peak efficiency or at the same expander speed for all engine operating points.

- *Perform a detailed 1-D simulation to capture additional limitations of the system that are not captured in the analytical study.*

  GT-Power simulations were performed to validate the trends observed from the analytical study. The simulation results show a minimum load below which the eTG is detrimental to the engine as predicted. This minimum load decreases with RPM due to the higher exhaust temperatures, and therefore higher eTG powers, present at higher engine speeds.

  To capture the eTG's impact on combustion, the knock-limited optimal spark timing was determined for each case by adjusting spark timing subject to an EGR sensitive knock constraint. The increased back pressure traps more in-cylinder residuals and requires higher gross indicated loads for the same demanded brake load. The result is less optimal spark timing to avoid knock, which along with the additional pumping, makes the eTG detrimental to the engine at the high loads as well, thereby limiting the eTG benefit to the mid-loads. Finally, steady-state drive cycle simulations were performed, and show an eTG benefit of 1.0/1.2% on Ford Fusion and Escape over combined cycle.

1.5 Dissertation Organization

In Chapter II the derivation of a compressible flow unsteady orifice equation is presented. The performance of the unsteady orifice equation is compared against the

traditional steady orifice equation using ideal temperature and pressure measurements from GT-Power LP and HP-EGR simulations.

The practical aspects of implementing the EGR estimation algorithm are considered in Chapter III. The optimal sensor configuration is determined first. Less computationally expensive approximations of the compressible flow unsteady orifice equation are then evaluated using both simulation and experimental data. Finally, the ΔP sampling frequency requirement is determined.

In Chapter IV, the impact of gauge-line distortions on the LP-EGR estimation error is studied using GT-Power simulations. A method for compensating for the gauge-line errors is then proposed and evaluated.

EGR valve area offset errors are studied in Chapter V. The feasibility of imposing a lower bound on valve lift to avoid problematic low lift operation regions is investigated. An online calibration method for the HP-EGR valve area is then developed and assessed.

Chapter VI covers the second part of this thesis on electric turbo-generation. An analytical study using the ideal Otto cycle is conducted to assess the main tradeoff between the recovered energy and increased pumping losses due the WHR expander. More realistic 1-D engine simulations are performed to capture the effects of engine speed, combustion phasing and engine heat transfer, and used to estimate drive cycle fuel economy improvements.

Finally, conclusions and future work are presented in Chapter VII.

CHAPTER II

Modeling Pulsating Flow through a Valve

In this chapter, the accuracy of the traditional *steady* compressible flow orifice equation (OE) to estimate EGR flow is evaluated using GT-Power simulations. To better model the pulsating flow across an EGR valve or orifice, an *unsteady* compressible flow orifice equation was derived from the 1-D isentropic momentum equation using minimal assumptions. The performance of the derived unsteady formulation was evaluated against 1-D engine simulation results. Additional assumptions were considered to simplify the unsteady orifice equation. The validity of these assumptions was justified by comparing the accuracy of the simplified formulations to the original equation. The performance of the derived unsteady formulation is also compared to that of the traditional *steady* compressible flow equation.

A description of the 1-D engine models with LP and HP-EGR is provided first, and used to evaluate the accuracy of the steady compressible flow orifice equation.A summary of previous literature on the incompressible flow case is then provided; the derivations for the compressible flow case are presented afterwards.

2.1 1-D Engine Simulations

Two engine models of the Ford 1.6 L I4 EcoBoost were considered to evaluate the performance of the various flow formulations used to estimate the EGR flow across the EGR valve in both LP and HP-EGR configurations.

2.1.1 Engine Simulations with LP-EGR

A 1-D gas dynamic simulation that solves continuity, 1-D momentum, and energy equations for compressible flows over a staggered grid was employed to investigate

the LP-EGR flow on the Ford 1.6 L I4 EcoBoost engine. A fast-running GT-Power model, where air and exhaust path elements like intake and exhaust manifolds are lumped into single volumes, was used. The model is a modified version of a 1.6 L EcoBoost GT-Power model provided by Ford Motor Company. It incorporates variable valve timing (VVT) on both intake and exhaust cams, and uses a semi-predictive combustion model that takes into account the impact of EGR on burn rates.

The EGR poppet valve was modeled using the GT-Power orifice template. The orifice discharge coefficient in the model was imposed using the limited valve manufacturer steady-flow bench data that was available. The valve effective area (A_e), or alternatively the discharge coefficients (C_D), computed based on the provided flow data at pressure differentials of 2 and 5 kPa show a considerable pressure dependence (Fig. (2.1)). At low valve lifts, a larger effective area is observed at lower ΔP; this trend reserves at higher lifts ($\gtrsim$ 1 mm). Due to the lack of flow data at ΔP's other than 2 and 5 kPa, the imposed effective area in GT-Power was linearly interpolated between 2 and 5 kPa; the forward flow effective area at (positive) ΔP's below 2 kPa or above 5 kPa was set to the same-lift effective area at 2 and 5 kPa respectively. The reverse flow effective area (at negative ΔP's) was assumed to be symmetric to its forward flow counterpart.

The GT-Power orifice template can account for pressure recovery following the orifice throat. This is automatically achieved by solving the momentum equation. The steady and unsteady orifice flow formulations presented in Sections 2.4 and 2.5 do not account for the pressure recovery phenomenon. As a result, the flow estimates using the orifice equations, with the pressure ratio defined as downstream pressure (instead of throat pressure) divided by the upstream pressure, do not match those from GT-Power with identical imposed effective area even under steady flow conditions [44].

It would be undesirable to use the throat pressure as a measurement in practice under reversing flow conditions as this would require three pressure measurements: valve inlet, valve outlet and throat pressures. The valve inlet and throat pressures would be needed to compute the pressure ratio under forward flow conditions, while the valve outlet and throat pressures would be required for the reverse flow instances. On the other hand, while extending the flow formulations to include a physical model to account the pressure recovery phenomenon would not require measuring the throat pressure, it would result in undesirable complexity. A simpler way to account for the effect of pressure recovery without the need to measure the throat pressure is by

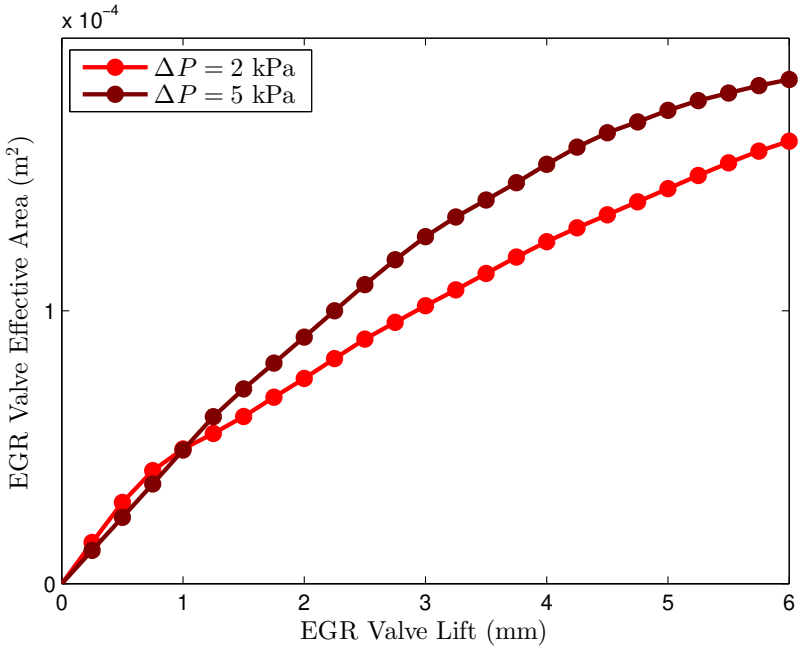

Figure 2.1: EGR valve effective area ($A_e = C_D A_T$) computed from the valve manufacturer data provided for ΔP of 2 and 5 kPa showing significant pressure dependence.

using a pressure-dependent effective area (A_e), or equivalently, a pressure-dependent discharge coefficient (C_D). In fact, a pressure-dependent effective area is observed when steady flow experimental data is fitted to the steady orifice equation (Fig. (2.1)). The GT-Power manual recommends setting the 'pressure recovery choice attribute' to 'Isentropic - No Recovery' when the effective area is imposed by the user using experimental data [44].

The EGR valve lift and AIS throttle angle were swept independently for a range of engine speeds and brake mean effective pressures (BMEP). Target BMEP's were achieved by adjusting the intake throttle and turbocharger wastegate while maintaining same equivalence ratio. EGR valve openings of 5% and 10% through 100% at 10% increments were considered. The AIS openings were increased from 1% to 5% with step sizes of 0.5%; coarser step sizes of 5% were used for openings up to 100%. This provides a range of possible EGR percentages where similar EGR percentages are obtained through different combinations of valve lift and ΔP at each simulated speed-load point. BMEP values between 2 and 20 bar, along with engine speeds between 1000 and 3000 RPM were chosen for this study. Cases where the desired load cannot be achieved, or where obtained the EGR percentage exceeds

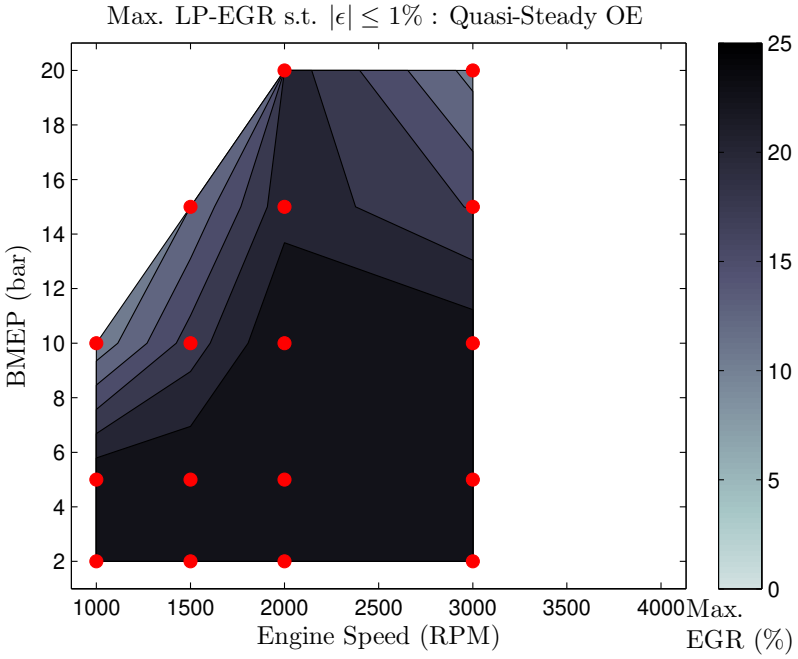

Figure 2.2: Contours of maximum achievable LP-EGR; simulated points are shown as solid red circles.

25%, were discarded. Figure (2.2) shows the simulated speed-load points along with the contours of maximum achievable EGR percentage.

2.1.2 Engine Simulations with HP-EGR

A GT-Power model of the Ford 1.6 L I4 EcoBoost engine with an added HP-EGR loop was used to investigate HP-EGR flow estimation. Similar to the engine model with an added LP-EGR loop described in the previous subsection, this model is fast-running, incorporates VVT on both intake and exhaust cams, and uses a semi-predictive combustion model that takes into account the impact of EGR on burn rates. The semi-predictive combustion model includes a Weibe function where the 0-90 burn duration $\Delta\theta_{90}$ and shape factor n are obtained using the correlation from Bonetesta *et al.* [45]:

$$\begin{cases} \Delta\theta_{90} = A_1 \left(\dfrac{1}{\rho_{ST}}\right)^{A_2} \left(1 - \dfrac{A_3}{\sqrt{S_P}}\right) \left(\dfrac{1}{1 - A_4 x_r^{A_5}}\right)^{A_6} \left(A_7\theta_{ST}^2 + A_8\theta_{ST} + 1\right) \\ n = A_9 \left(\dfrac{1}{\sqrt{S_P}}\right)^{A_{10}} \left(\dfrac{1}{1 + \sqrt{\theta_{ST}}}\right)^{A_{11}} (1 - A_{12} x_r) \end{cases} \tag{2.1}$$

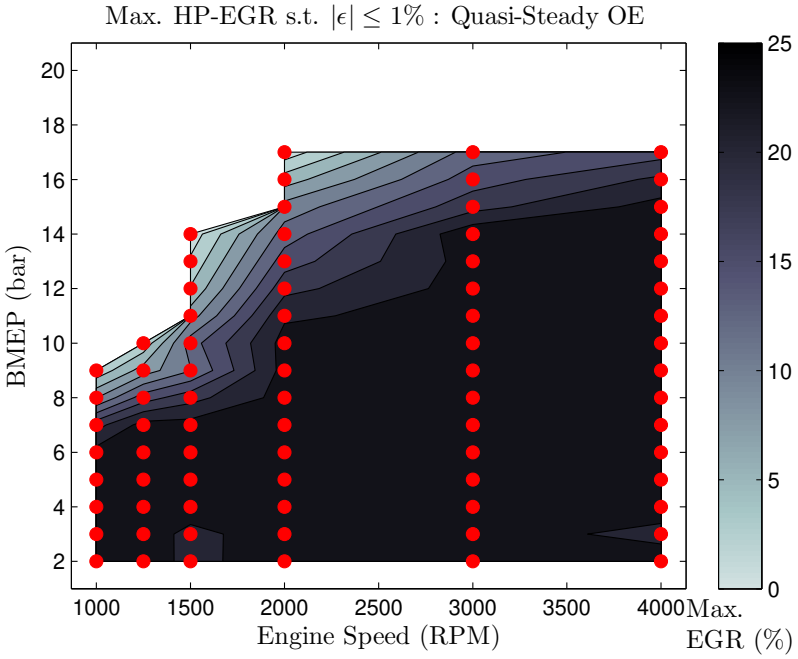

Figure 2.3: Contours of maximum achievable HP-EGR; simulated points are shown as solid red circles.

where ρ_{ST} is the in-cylinder gas density at spark, S_P is the mean piston speed, θ_{ST} is the spark timing, and x_r is the in-cylinder residuals (total of internal and external EGR). The fit parameters A_1 through A_{12} were recalibrated to the 1.6 L EcoBoost engine data. Maps for intake and exhaust cam timings, and boost reserve were obtained from experimental data. The knock-limited maximum brake torque (MBT) spark timing was determined by adjusting spark timing subject to an EGR sensitive knock constraint given by a Livengood-Wu [46] ignition delay integral with the Arrhenius ignition delay (τ_{ign}) expression developed by Hoepke *et al.* [11]:

$$\tau_{\text{ign}} = A \left(\frac{p}{T}\right)^{-a} (1 - x_r)^{-b} \exp\left(\frac{E}{T}\right) \tag{2.2}$$

where p and T denote the pressure and temperature of the end gas. The knock model calibration for parameters a, b and A and E was performed by Hoepke for an research octane number (RON) of 97 [11]; a retuned value of E by Middleton was used here [47]. The ignition delay τ_{ign} can be obtained for different octane numbers using $\tau_{\text{ign}} \propto (\text{ON})^{3.402}$ [11]. Various model-predicted parameters including brake specific fuel consumption (BSFC) and intake and exhaust manifold pressures were verified against experimental data. Finally, the EGR poppet valve model used is identical to

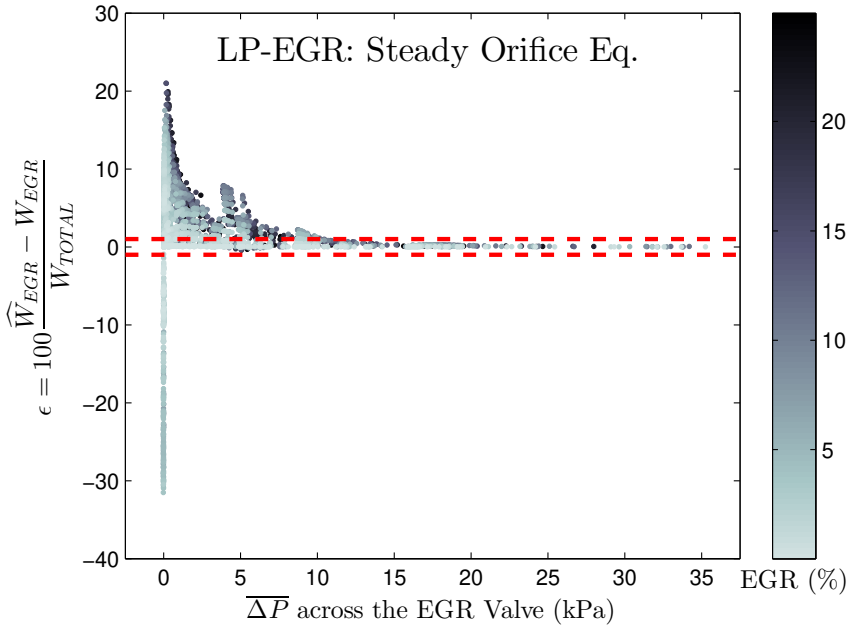

Figure 2.4: LP-EGR estimation error for the compressible flow steady orifice equation.

that described in the previous subsection.

Engine speeds between 1000 and 4000 RPM, and engine loads between 2 and 17 bar BMEP were chosen for the HP-EGR study (Fig. (2.3)). At each speed load point, the EGR percentage was swept from 1 to 25%. Target EGR percentages were achieved using the GT-Power EGR controller template to dictate the EGR valve lift. Cases where the desired load or desired EGR percentage cannot be attained (due to the inability to sustain the target load at a given EGR percentage, or the inability to flow the target EGR amount with fully open EGR valve) were discarded. Cases where the turbocharger compressor operates in the surge region were also omitted. It should be noted here that the LP-EGR simulations have two actuators to control the EGR flow: EGR valve lift and AIS throttle angle, compared to only EGR valve lift in the case of HP-EGR. The additional independent variable in the LP-EGR configuration required the use of coarser speed-load grid (Fig. (2.2)) compared to the speed-load grid used for the HP-EGR simulations (Fig. (2.3)).

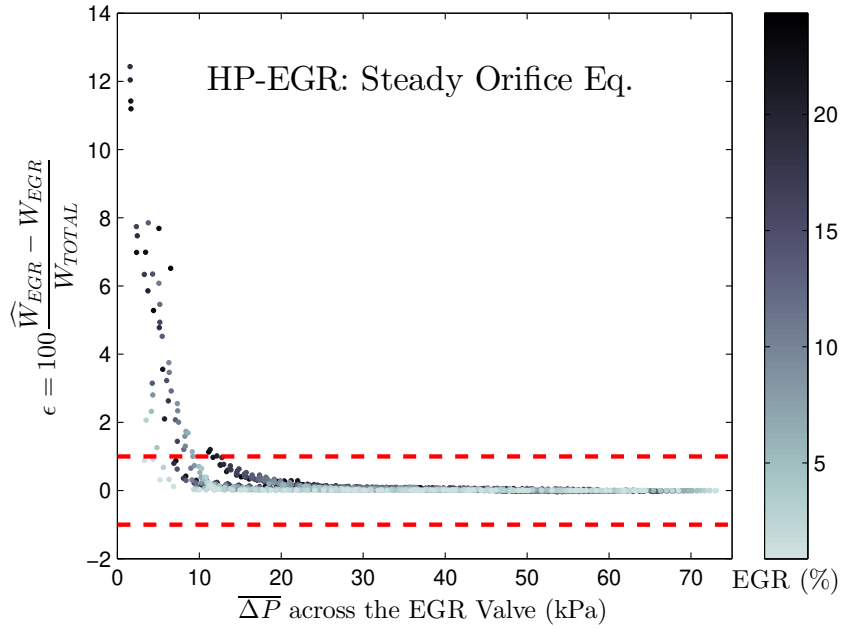

Figure 2.5: HP-EGR estimation error for the compressible flow steady orifice equation.

2.2 Compressible Flow Steady Orifice Equation

The compressible flow steady orifice equation can be used to estimate the EGR flows on engine application [48]:

$$W = \widetilde{\Psi}(p_i, p_o, T_i, T_o) = \begin{cases} A_e \dfrac{p_i}{\sqrt{RT_i}} \widetilde{P}_r^{\frac{1}{\gamma}} \sqrt{\dfrac{2\gamma}{\gamma - 1}\left(1 - \widetilde{P}_r^{\frac{\gamma-1}{\gamma}}\right)}, \text{ if } p_i \geq p_o \\ -A_e \dfrac{p_o}{\sqrt{RT_o}} \widetilde{P}_r^{\frac{1}{\gamma}} \sqrt{\dfrac{2\gamma}{\gamma - 1}\left(1 - \widetilde{P}_r^{\frac{\gamma-1}{\gamma}}\right)}, \text{ if } p_i < p_o \end{cases} \tag{2.3}$$

where W is the mass flow rate, A_e is the effective area, p_i is the inlet pressure, p_o is the outlet pressure, T_i is the inlet temperature, T_o is outlet temperature, R is the gas constant, γ is the ratio of specific heats, and $\widetilde{P}_r$ is the pressure ratio:

$$\widetilde{P}_r(p_i, p_o) = \begin{cases} \max\left[\dfrac{p_o}{p_i}, P_{r,CR}\right], \text{ if } p_i \geq p_o \\ \max\left[\dfrac{p_i}{p_o}, P_{r,CR}\right], \text{ if } p_i < p_o \end{cases} \tag{2.4}$$

The simplest flow estimate is obtained with the steady orifice equation and averaged input pressures and temperatures. Averaging the input parameters results in a non-linearity error given the non-linearity of the compressible flow orifice equation: $\overline{\widetilde{\Psi}(p_i, p_o, T_i, T_o)} \neq \widetilde{\Psi}(\overline{p_i}, \overline{p_o}, \overline{T_i}, \overline{T_o})$. This error can be especially large if $p_i \approx p_o$. The lack of dynamics in the steady orifice equations also results in an inertial error. Figures (2.4) and (2.5) show the LP and HP-EGR estimation error in the case where the steady orifice equation is used with averaged input parameters to compute an estimated EGR flow ($\widehat{W}_{EGR}$). The EGR estimation error (ϵ) is then calculated as:

$$\epsilon = 100 \frac{\widehat{W}_{EGR} - W_{EGR}}{W_{TOTAL}}. \tag{2.5}$$

where W_{EGR} and W_{TOTAL} are the EGR and total engine flow from GT-Power. Errors up to $\approx 30\%$ and $\approx 12\%$ can be observed for the LP and HP-EGR configuration respectively. An accuracy requirement of $|\epsilon| \leq 1\%$ is provided by Ford; this would limit the additional equivalence ratio errors to 1.33% for EGR percentages up to 25%. This accuracy requirement is not achieved for LP and HP $\overline{\Delta P}$'s below 10.1 and 9.2 kPa respectively.

2.3 Compressible Flow Quasi-Steady Orifice Equation

A better approximation of the flow is obtained by using the instantaneous crank angle (CA) resolved input parameters in the steady orifice equation. This assumes quasi-steady conditions where, at any instant, the estimated flow is approximated by the resulting steady flow if the current input parameters were held constant. Figures (2.6) and (2.7) show a significant improvement in the LP and HP-EGR estimation error with the quasi-steady orifice equation as the non-linearity error is avoided. However, the impact of the inertial can be observed in the LP-EGR case where the estimation error exceeds the $\pm 1\%$ bounds at the low $\overline{\Delta P}$ (< 1.4 kPa). The inertial error in the simulated HP-EGR cases is small where the lowest simulated $\overline{\Delta P}$ is 1.5 kPa. Accounting for the inertial effects using the unsteady orifice equation is needed for improved accuracy at the low ΔP conditions.

2.4 Incompressible Flow Unsteady Orifice Equation

McKee et al. [28] and Gajan et al. [40] investigated the sources of pulsating flow estimation errors present using the steady incompressible orifice equation $W \propto \sqrt{\Delta P}$

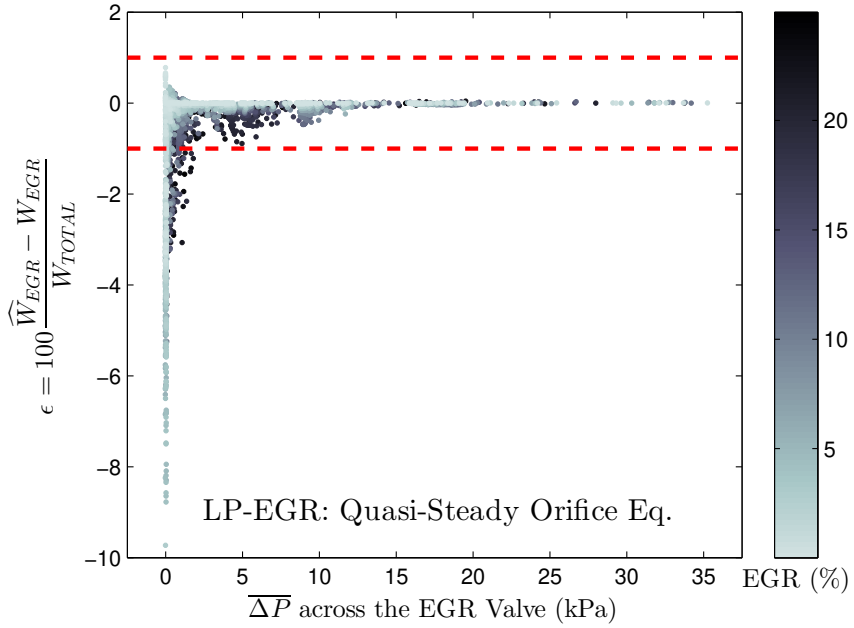

Figure 2.6: LP-EGR estimation error for the compressible flow quasi-steady orifice equation.

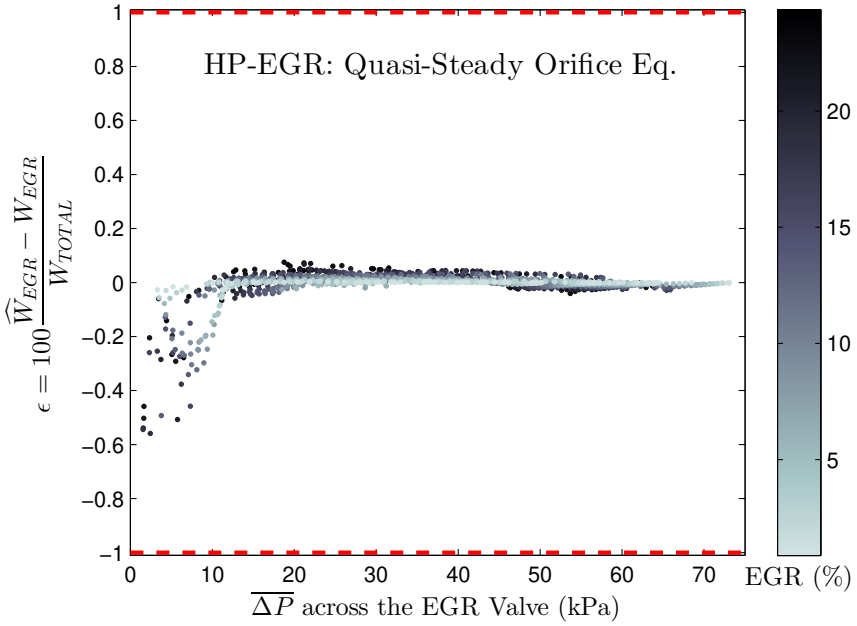

Figure 2.7: HP-EGR estimation error for the compressible flow quasi-steady orifice equation.

where W is the mass flow rate. Errors include the square root error (SRE) and the inertial error. The SRE is a result of the non-linearity of the square root function and accounts for the majority of the error when the averaged ΔP is used in the incompressible orifice equation. The averaging in the ΔP measurement can be due to a low frequency response ΔP transducer with built-in damping to attenuate fluctuations. Avoiding the SRE requires computing the mean of the square root of a rapidly sampled ΔP signal [28, 40]. Consequently, the averaged flow is estimated with reasonable accuracy if the assumption of a quasi-steady flow holds. This is true when the Strouhal number $S_t = f d_e / \overline{U} << 1$ where f is the pulsation frequency, d_e is valve effective diameter, and $\overline{U}$ is the bulk mean velocity [40]. Otherwise, the inertia component should be accounted for:

$$\frac{\partial u}{\partial t} + u\frac{\partial u}{\partial x} + \frac{1}{\rho}\frac{\partial p}{\partial x} = 0 \tag{2.6}$$

where u is the velocity, ρ is the density, and p is the pressure. According to McKee et al. [28] and Gajan et al. [40], integrating Eq. (2.6) with respect to x (from upstream the valve to the valve throat) with the assumption of an incompressible fluid results in:

$$2A_e^2 \rho K \frac{d}{dt} W + W^2 = 2A_e^2 \rho \Delta P\,(t) \tag{2.7}$$

where A_e is the effective area (flow cross-sectional area multiplied with the discharge coefficient $C_D A_T$). The term K is independent of the pulsations [40], and $K dW/dt$ accounts for the inertial effects. Other errors discussed by McKee et al. [28] and Gajan et al. [28, 40] include flow coefficient shifts, gauge-line amplification or attenuation, and pressure transducer response.

Depending on the value of ΔP, the assumption of an incompressible fluid ($\rho =$ constant) can be inappropriate for the flow across the EGR valve. Relative steady-state flow errors greater than 5% can be observed for a $\Delta P > 8.4$ kPa (at 1 bar upstream pressure) if the incompressible orifice equation is used. The compressible flow case is considered next.

2.5 Compressible Flow Usteady Orifice Equation

It is common practice in engine modeling to estimate flow through valves (e.g. throttle and poppet valves) and orifices with the steady compressible isentropic flow orifice equation. The effect of non-ideal behaviors resulting from irreversibility is accounted for by introducing the discharge coefficient, C_D [48]. Using the same logic,

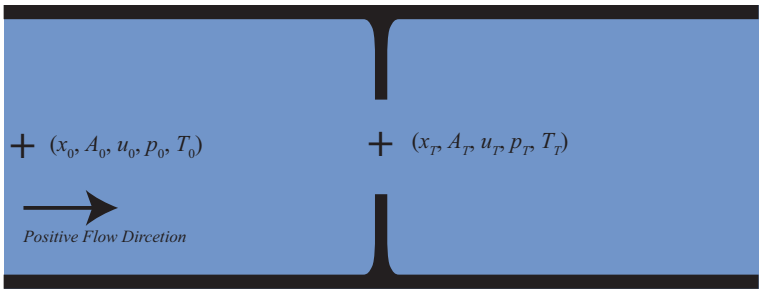

Figure 2.8: Orifice diagram showing parameters of interest.

an isentropic process:

$$\rho = \rho_0 \left(\frac{p}{p_0} \right)^{\frac{1}{\gamma}} \tag{2.8}$$

can be assumed for a flow from upstream of the valve or orifice (x_0) to the valve or orifice throat (x_T) where $x_0 < x_T$ and the flow is in the positive x-direction (Fig. (2.8); adjustments for reverse flow (in the negative x-direction) is considered afterwards. The 1-D momentum equation for compressible and inviscid flow expressed in the non-conservative form (Eq. (2.6)) can be rewritten as:

$$\frac{\partial u}{\partial t} + u\frac{\partial u}{\partial x} + \frac{p_0^{\frac{1}{\gamma}}}{\rho_0}\frac{1}{p^{\frac{1}{\gamma}}}\frac{\partial p}{\partial x} = 0 \tag{2.9}$$

Integrating from x_0 to x_T with pressures p_0 and p_T at x_0 and x_T respectively gives:

$$\int_{x_0}^{x_T} \frac{\partial u}{\partial t} dx + \frac{u_T^2}{2} - \frac{u_0^2}{2} + \frac{p_0^{\frac{1}{\gamma}}}{\rho_0} \int_{p_0}^{p_T} p^{-\frac{1}{\gamma}} dp = 0 \tag{2.10}$$

Realizing that:

$$u = \frac{W}{\rho A} = \frac{W}{\rho_0 A}\left(\frac{p_0}{p} \right)^{\frac{1}{\gamma}} \tag{2.11}$$

where A is the cross-sectional area at x, Eq. (2.10) can be rewritten as:

$$\int_{x_0}^{x_T} \frac{1}{A}\frac{\partial}{\partial t}\left(\frac{W(x) p_0^{\frac{1}{\gamma}}}{\rho_0 p^{\frac{1}{\gamma}}} \right) dx + \frac{W_T^2}{2A_T^2\rho_0^2}\left(\frac{p_0}{p_T} \right)^{\frac{2}{\gamma}} - \frac{W_0^2}{2A_0^2\rho_0^2} = \frac{p_0^{\frac{1}{\gamma}}}{\rho_0}\frac{\gamma}{\gamma - 1}\left(p_0^{\frac{\gamma-1}{\gamma}} - p_T^{\frac{\gamma-1}{\gamma}} \right) \tag{2.12}$$

Assuming the variation of the mass flow rate with x from x_0 to x_T is negligible: $W(x) \approx W$, and defining the pressure ratio (P_r) across the valve or orifice as:

$$P_r = \frac{p_T}{p_0}, \tag{2.13}$$

gives:

$$\int_{x_0}^{x_T} \frac{1}{A}\frac{\partial}{\partial t}\left(\frac{W p_0^{\frac{1}{\gamma}}}{\rho_0 p^{\frac{1}{\gamma}}}\right) dx + P_r^{\frac{-2}{\gamma}} \frac{W^2}{2A_T^2\rho_0^2}\left(1 - \frac{A_T^2}{A_0^2}P_r^{\frac{2}{\gamma}}\right) = \frac{p_0}{\rho_0}\frac{\gamma}{\gamma-1}\left(1 - P_r^{\frac{\gamma-1}{\gamma}}\right) \tag{2.14}$$

Rearranging Eq. (2.14) gives:

$$2A_T^2\rho_0^2 P_r^{\frac{2}{\gamma}} \int_{x_0}^{x_T} \frac{1}{A}\frac{\partial}{\partial t}\left(\frac{W p_0^{\frac{1}{\gamma}}}{\rho_0 p^{\frac{1}{\gamma}}}\right) dx + W^2\left(1 - \frac{A_T^2}{A_0^2}P_r^{\frac{2}{\gamma}}\right) = A_T^2\rho_0 p_0 P_r^{\frac{2}{\gamma}}\frac{2\gamma}{\gamma-1}\left(1 - P_r^{\frac{\gamma-1}{\gamma}}\right) \tag{2.15}$$

Applying the ideal gas law:

$$\rho = \frac{p}{RT} \tag{2.16}$$

to the right hand side of Eq. (2.15) gives:

$$2A_T^2\rho_0^2 P_r^{\frac{2}{\gamma}} \int_{x_0}^{x_T} \frac{1}{A}\frac{\partial}{\partial t}\left(\frac{W p_0^{\frac{1}{\gamma}}}{\rho_0 p^{\frac{1}{\gamma}}}\right) dx + W^2\left(1 - \frac{A_T^2}{A_0^2}P_r^{\frac{2}{\gamma}}\right) = \Psi^2(P_r, p_0, T_0) \tag{2.17}$$

where $\Psi(P_r, p_0, T_0)$ is steady compressible-flow orifice equation:

$$\Psi(P_r, p_0, T_0) = A_T\frac{p_0}{\sqrt{RT_0}}P_r^{\frac{1}{\gamma}}\sqrt{\frac{2\gamma}{\gamma-1}\left(1 - P_r^{\frac{\gamma-1}{\gamma}}\right)} \tag{2.18}$$

The integral term in Eq. (2.17) accounts for the inertial effects. However, by dropping the intertial term, Eq. (2.17) deos not simply reduce to the steady compressible-flow orifice formulation: $W = \Psi(P_r, p_0, T_0)$ unless the throat area is significantly smaller than the area upstream of the valve or orifice: $A_T \ll A_0$. It is convenient here to define:

$$C_0 = \left(1 - \frac{A_T^2}{A_0^2}P_r^{\frac{2}{\gamma}}\right)^{-1} \tag{2.19}$$

where C_0 can be viewed as correction factor for cases where the assumption $A_T \ll A_0$ does not hold, or alternatively, the cases where the momentum of the incoming flow is not negligible (and the assumption $u_0 \approx 0$ is inaccurate). Now, Eq. (2.17) can be

rewritten as:

$$2C_0A_T^2\rho_0^2P_r^{\frac{2}{\gamma}}\int_{x_0}^{x_T}\frac{1}{A}\frac{\partial}{\partial t}\left(\frac{Wp_0^{\frac{1}{\gamma}}}{\rho_0 p^{\frac{1}{\gamma}}}\right)dx+W^2=C_0\Psi^2(P_r,p_0,T_0) \tag{2.20}$$

The integral term in Eq. (2.20) can be simplified by first applying the product rule on the partial derivative term inside the integral:

$$\int_{x_0}^{x_T}\frac{1}{A}\frac{\partial}{\partial t}\left(\frac{Wp_0^{\frac{1}{\gamma}}}{\rho_0 p^{\frac{1}{\gamma}}}\right)dx=\int_{x_0}^{x_T}\frac{1}{A}p_0^{\frac{1}{\gamma}}p^{-\frac{1}{\gamma}}\frac{\partial}{\partial t}\left(\frac{W}{\rho_0}\right)dx+\int_{x_0}^{x_T}\frac{1}{A}\frac{W}{\rho_0}\frac{\partial}{\partial t}\left(p_0^{\frac{1}{\gamma}}p^{-\frac{1}{\gamma}}\right)dx \tag{2.21}$$

Eq. (2.21) can be simplified by taking some of the terms independent of x out of the integral:

$$\int_{x_0}^{x_T}\frac{1}{A}\frac{\partial}{\partial t}\left(\frac{Wp_0^{\frac{1}{\gamma}}}{\rho_0 p^{\frac{1}{\gamma}}}\right)dx=\frac{d}{dt}\left(\frac{W}{\rho_0}\right)\int_{x_0}^{x_T}\frac{1}{A}\left(\frac{p}{p_0}\right)^{-\frac{1}{\gamma}}dx+\frac{W}{\rho_0}\int_{x_0}^{x_T}\frac{1}{A}\frac{\partial}{\partial t}\left(\frac{p}{p_0}\right)^{-\frac{1}{\gamma}}dx \tag{2.22}$$

The two integrals on the right hand side can be simplified by assuming that $(p/p_0)^{-1/\gamma}$ varies monotonically with x from 1 at x_0 to $P_r=p_T/p_0$ at x_T:

$$\begin{cases}\left(\dfrac{p}{p_0}\right)^{-\frac{1}{\gamma}}=1-f(x)+f(x)P_r^{-\frac{1}{\gamma}}\\[2ex]\dfrac{\partial}{\partial t}\left(\dfrac{p}{p_0}\right)^{-\frac{1}{\gamma}}=f(x)\dfrac{d}{dt}P_r^{-\frac{1}{\gamma}}\end{cases} \tag{2.23}$$

where $f(x)$ is a monotonic function in x with $f(x_0)=0$ and $f(x_T)=1$. This gives:

$$\begin{cases}\displaystyle\int_{x_0}^{x_T}\frac{1}{A}\left(\frac{p}{p_0}\right)^{-\frac{1}{\gamma}}dx=\int_{x_0}^{x_T}\frac{1-f(x)}{A}dx+P_r^{-\frac{1}{\gamma}}\int_{x_0}^{x_T}\frac{f(x)}{A}dx\\[2ex]\displaystyle\int_{x_0}^{x_T}\frac{1}{A}\frac{\partial}{\partial t}\left(\frac{p}{p_0}\right)^{-\frac{1}{\gamma}}dx=\frac{d}{dt}P_r^{-\frac{1}{\gamma}}\int_{x_0}^{x_T}\frac{f(x)}{A}dx\end{cases} \tag{2.24}$$

Defining tunable parameters K and $\widetilde{K}$:

$$\begin{cases} K = 2\int\limits_{x_0}^{x_T} \dfrac{1-f(x)}{A}dx \\ \widetilde{K} = 2\int\limits_{x_0}^{x_T} \dfrac{f(x)}{A}dx \end{cases}, \tag{2.25}$$

and substituting back in Eq. (2.22) gives:

$$2\int\limits_{x_0}^{x_T} \frac{1}{A}\frac{\partial}{\partial t}\left(\frac{W p_0^{\frac{1}{\gamma}}}{\rho_0 p^{\frac{1}{\gamma}}}\right)dx = \frac{d}{dt}\left(\frac{W}{\rho_0}\right)\left(K + \widetilde{K}P_r^{-\frac{1}{\gamma}}\right) + \frac{W}{\rho_0}\widetilde{K}\frac{d}{dt}P_r^{-\frac{1}{\gamma}} \tag{2.26}$$

Applying the product rule to $d(W/\rho_0)/dt$, and rearranging, Eq. (2.26) can be rewritten as:

$$\begin{aligned} 2\int\limits_{x_0}^{x_T} \frac{1}{A}\frac{\partial}{\partial t}\left(\frac{W p_0^{\frac{1}{\gamma}}}{\rho_0 p^{\frac{1}{\gamma}}}\right)dx = {} & \frac{1}{\rho_0}\frac{dW}{dt}\left(K + \widetilde{K}P_r^{-\frac{1}{\gamma}}\right) \\ & + \frac{W}{\rho_0}\left(\widetilde{K}\frac{d}{dt}P_r^{-\frac{1}{\gamma}} - \frac{d}{dt}\log\rho_0\left(K + \widetilde{K}P_r^{-\frac{1}{\gamma}}\right)\right) \end{aligned} \tag{2.27}$$

Substituting Eq. (2.27) back in Eq. (2.20) gives:

$$\begin{aligned} & C_0 A_T^2 \Phi\left[\left(K + \widetilde{K}P_r^{-\frac{1}{\gamma}}\right)\frac{dW}{dt} + \left(\widetilde{K}\frac{d}{dt}P_r^{-\frac{1}{\gamma}} - \frac{d}{dt}\log\frac{p_0}{RT_0}\left(K + \widetilde{K}P_r^{-\frac{1}{\gamma}}\right)\right)W\right] + W^2 \\ & = C_0\Psi^2(P_r, p_0, T_0) \end{aligned} \tag{2.28}$$

where:

$$\Phi\left(P_r, p_0, T_0\right) = \rho_0 P_r^{\frac{2}{\gamma}} = \frac{p_0}{RT_0}P_r^{\frac{2}{\gamma}}. \tag{2.29}$$

The above derivation was performed for forward flow where $x_0 < x_T$. When the flow reverses direction, the upstream pressure p_0 and temperature T_0 then refer to the pressure and temperature at some $x_0 > x_T$, and the integration of Eq. (2.9) should be carried out from x_T to x_0 resulting in the replacement of W^2 and Ψ^2 in Eq. (2.28) by $-W^2$ and $-\Psi^2$ respectively. Also, the deviations from the ideal flow conditions can be modeled by replacing the actual throat area (A_T) by the effective area: $A_e = C_D A_T$ where C_D is the discharge coefficient. To account for non ideal

effects in both forward and reverse flow conditions, Eq. (2.28) is rewritten as:

$$C_0 A_e^2 \widetilde{\Phi} \left[\left(K + \widetilde{K} \widetilde{P}_r^{-\frac{1}{\gamma}} \right) \frac{dW}{dt} + \left(\widetilde{K} \frac{d}{dt} \widetilde{P}_r^{-\frac{1}{\gamma}} - \frac{d}{dt} \log \frac{p_0}{RT_0} \left(K + \widetilde{K} \widetilde{P}_r^{-\frac{1}{\gamma}} \right) \right) W \right] + W |W| = C_0 \widetilde{\Psi} \left| \widetilde{\Psi} \right| \tag{2.30}$$

where:

$$\widetilde{\Psi}(p_i, p_o, T_i, T_o) = \begin{cases} A_e \dfrac{p_i}{\sqrt{RT_i}} \widetilde{P}_r^{\frac{1}{\gamma}} \sqrt{\dfrac{2\gamma}{\gamma - 1} \left(1 - \widetilde{P}_r^{\frac{\gamma-1}{\gamma}} \right)}, \text{ if } p_i \geq p_o \\ -A_e \dfrac{p_o}{\sqrt{RT_o}} \widetilde{P}_r^{\frac{1}{\gamma}} \sqrt{\dfrac{2\gamma}{\gamma - 1} \left(1 - \widetilde{P}_r^{\frac{\gamma-1}{\gamma}} \right)}, \text{ if } p_i < p_o \end{cases}, \tag{2.31}$$

$$\widetilde{\Phi}(p_i, p_o, T_i, T_o) = \begin{cases} \dfrac{p_i}{RT_i} \widetilde{P}_r^{\frac{2}{\gamma}}, \text{ if } p_i \geq p_o \\ \dfrac{p_o}{RT_o} \widetilde{P}_r^{\frac{2}{\gamma}}, \text{ if } p_i < p_o \end{cases}, \tag{2.32}$$

and:

$$\widetilde{P}_r(p_i, p_o) = \begin{cases} \max \left[\dfrac{p_o}{p_i}, P_{r,CR} \right], \text{ if } p_i \geq p_o \\ \max \left[\dfrac{p_i}{p_o}, P_{r,CR} \right], \text{ if } p_i < p_o \end{cases} \tag{2.33}$$

The subscripts i and o in Eq. (2.31) through (2.33) denote valve (or orifice) inlet and outlet respectively, and $P_{r,CR}$ in Eq. (2.33) denotes the critical pressure ratio below which choking conditions are encountered. The critical pressure ratio can be expressed in terms of the ratio of specific heats (γ) [21]:

$$P_{r,CR} = \left(\frac{2}{\gamma + 1} \right)^{\frac{\gamma}{\gamma - 1}} \tag{2.34}$$

Previous literature shows lower values for choking pressure compare to Eq. (2.34). Proposed methods to address this issue can be found in the literature [49, 50].

It should be noted here that the pressure ratio used in Eq. (2.28) is defined as throat pressure divided by upstream pressure; however, the pressure ratio used in Eq. (2.30) is defined as downstream pressure divided by upstream pressure. These two definitions are not identical due the pressure recovery that occurs downstream of the valve or orifice throat; the downstream pressure is higher than the throat pressure. While it is more practical to use the upstream and downstream pressures, the impact of pressure recovery can be corrected for by using a pressure dependent

discharge coefficient (C_D), and therefore, a pressure dependent effective area (A_e). More details on pressure recovery is presented in the following section.

2.6 Evaluation of the Unsteady Compressible Flow Formulation

In Section 2.5, an unsteady compressible-flow orifice equation (Eq. (2.30)) was derived with minimal assumptions. In this section, the LP and HP-EGR simulations described in Section 2.1 are used to evaluate the aforementioned unsteady orifice equation (Eq. (2.30)) and any possible simplifications resulting from the following assumptions:

1. *Negligible upstream velocity* ($u_0 \approx 0$): This assumption is justifiable if the upstream area is significantly larger than the valve's throat area ($A_0 \gg A_e$). As a result the term C_0 in Eq. (2.30) is set to 1.

2. *Negligible density variation with time* ($\partial\rho/\partial t \approx 0$): Due to the variation of pressure and temperature with time, the density of the flow also varies with time. But the relative variation in density $((\partial\rho/\partial t)/\overline{\rho})$[1] is small compared to the relative variation in flow $((dW/dt)/\overline{W})$ especially at the low ΔP's with flow reversal where the inertial effects are significant.

3. *Negligible dependence of the coefficient of the transient term* (dW/dt) *on the pressure ratio* ($\widetilde{K} \approx 0$): This also follows from the relative variation in pressure with time $((\partial p/\partial t)/\overline{p})$ being small compared to the relative variation in flow (see Eq. (2.23) through (2.25)).

While the effective area A_e values imposed in the GT-Power simulations can be used directly in the unsteady orifice equation (Eq. (2.30)) to estimate $\widehat{W}_{EGR}$, the K and $\widetilde{K}$ terms are unknown and need to be fitted. The K and $\widetilde{K}$ values that minimize the sum of squares of the difference between the right and left hand sides of Eq. (2.30) were first computed using the CA resolved W_{EGR} predicted by GT-Power, then fitted as a function of the EGR valve lift using a 3$^{\text{rd}}$ order polynomial with zero y-intercept. Figures (2.9(a)) through (2.16(a)) show the LP and HP-EGR estimation errors plotted against the average ΔP across the EGR valve. The target EGR estimation error bound of $\pm 1\%$ is satisfied for all $\overline{\Delta P}$ with and without the aforementioned simplifying assumptions. Figures (2.9) through (2.16) also show the K and $\widetilde{K}$ fits for both EGR configurations.

[1] The over-bar is used to denote averaged quantities.

As a result, a simplified compressible flow unsteady orifice equation can be obtained by applying all three simplifying assumptions:

$$A_e^2\widetilde{\Phi}(p_i, p_o, T_i, T_o)K\frac{dW}{dt} + W\,|W| = \widetilde{\Psi}\left|\widetilde{\Psi}\right|(p_i, p_o, T_i, T_o) \tag{2.35}$$

Eq. (2.35) will be used as the unsteady orifice equation for the rest of this work. Figures (2.17(a)) and (2.18(a)) show the LP and HP-EGR estimation errors for Eq. (2.35) respectively.

Figures (2.19) and (2.20) show LP and HP-EGR estimation error at the maximum achievable EGR percentage for each simulated speed-load point. LP-EGR estimation errors up to 13.2, 3.0 and 0.6% are obtained with the steady, quasi-steady and unsteady orifice equations. The largest improvements of the unsteady formulations are observed at the low loads and low speeds where the $\overline{\Delta P}$ across the LP-EGR valve is minimal. Estimation errors up to 7.8, 0.6 and 0.2% are observed for the HP-EGR case with the steady, quasi-steady and unsteady formulations. The largest improvements of the quasi-steady and unsteady orifice equations are observed near the naturally-aspirated and slightly boosted regions where the difference between the intake and exhaust manifold pressures is minimal leading to low $\overline{\Delta P}$ across the HP-EGR.

2.7 Summary and Conclusions

This chapter investigates the impact of the steady, quasi-steady and the newly derived unsteady flow formulations on the LP and HP-EGR estimation errors using GT-Power simulations. Errors exceeding the target ±1% are observed with the steady orifice equation for average $\overline{\Delta P}$ below 10.1 and 9.2 kPa for the LP and HP-EGR systems. The large estimation errors are mainly due the non-linearity error resulting from using average pressures and temperatures. If instantaneous inputs are used instead (quasi-steady formulation), the LP and HP-EGR estimation errors are significantly reduced. While a $\overline{\Delta P}$ lower bound[2] of 1.4 kPa is required to keep the LP-EGR estimation error within ±1%, all HP-EGR estimation errors lie within the target error bound (lowest simulated $\overline{\Delta P}$ of 1.5 kPa). To get the LP-EGR estimation errors at the low $\overline{\Delta P}$ (< 1.4 kPa) within the ±1% bounds, inertial effects should be accounted for using the newly derived compressible flow unsteady orifice equation.

[2]The $\overline{\Delta P}$ lower bounds are defined for all cases such that 99.7% (3 σ) of the EGR estimation errors are within the specified error bound.

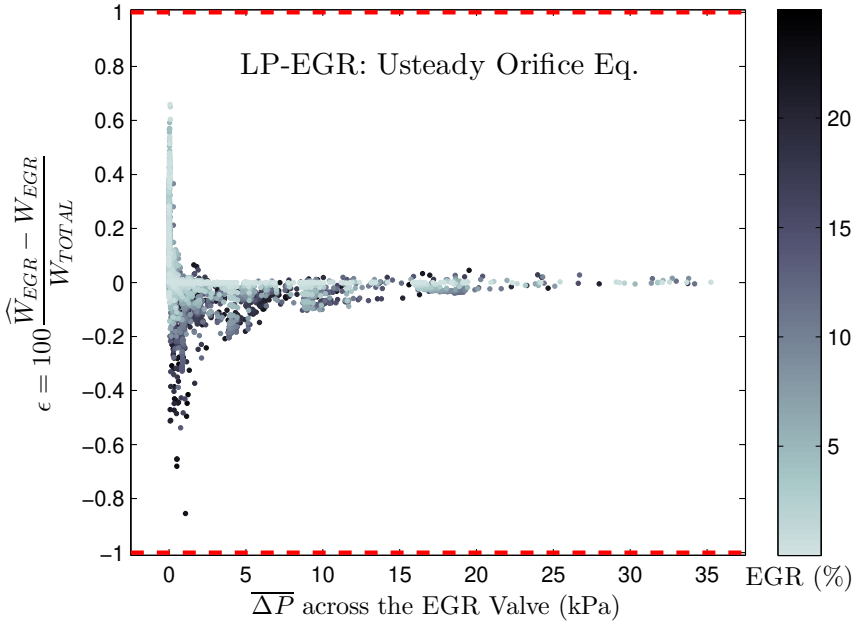

(a) LP-EGR Estimation Error

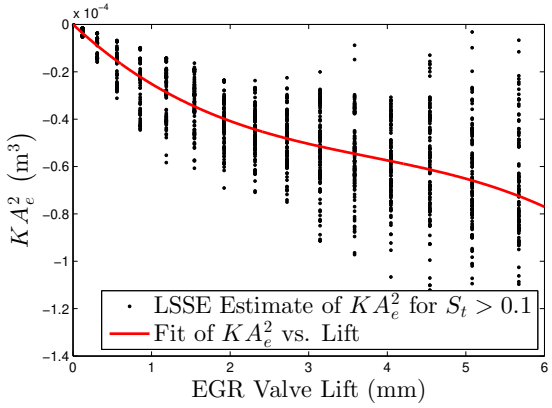

(b) K Fit

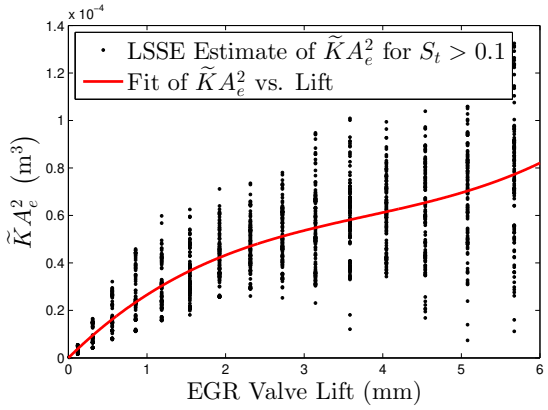

(c) $\widetilde{K}$ Fit

Figure 2.9: LP-EGR estimation error and K and $\widetilde{K}$ fits for the compressible flow unsteady orifice equation. Target EGR estimation error bounds are shown as dashed red lines.

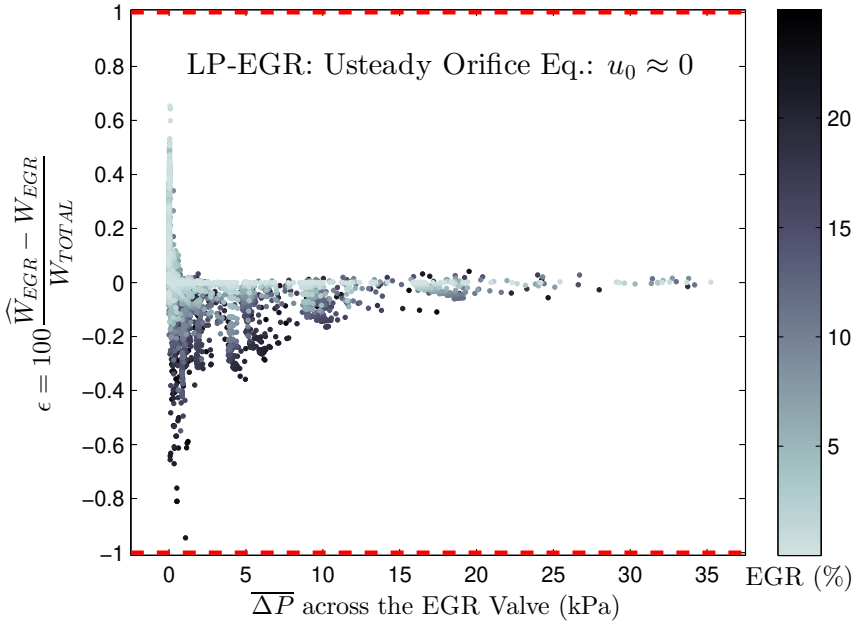

(a) LP-EGR Estimation Error

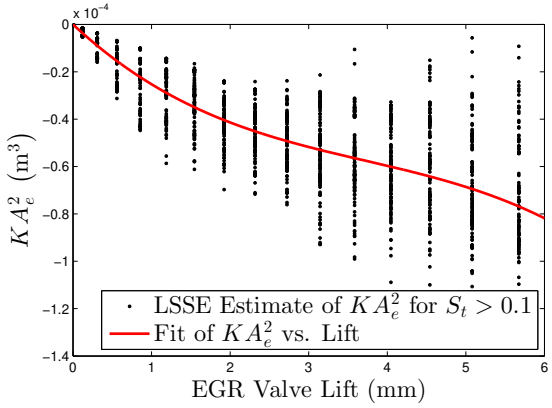

(b) K Fit

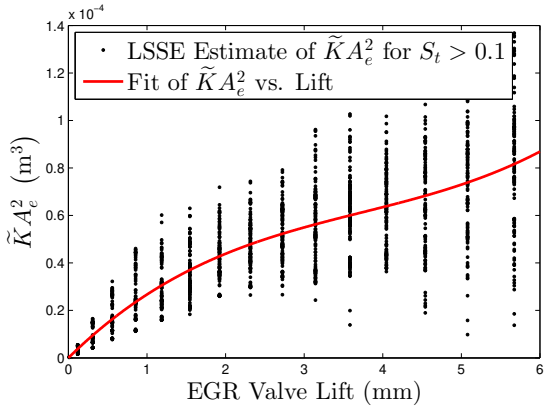

(c) $\widetilde{K}$ Fit

Figure 2.10: LP-EGR estimation error and K and $\widetilde{K}$ fits for the compressible flow unsteady orifice equation with the $u_0 \approx 0$ assumption. Target EGR estimation error bounds are shown as dashed red lines.

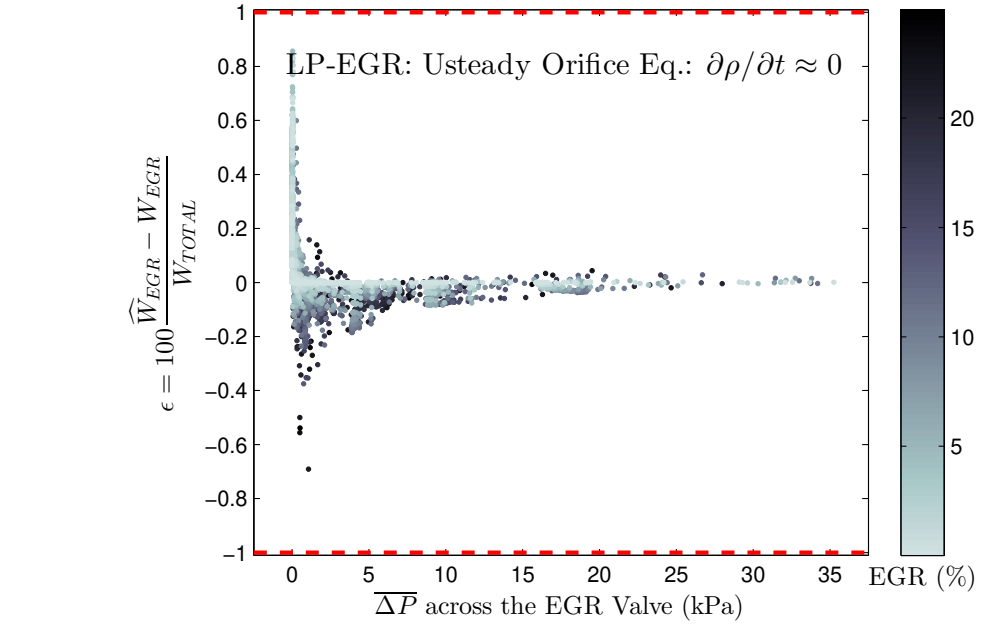

(a) LP-EGR Estimation Error

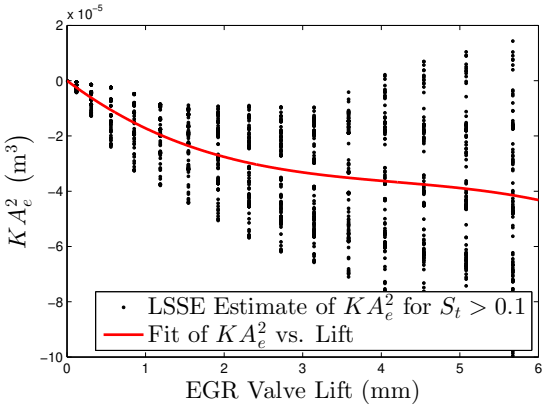

(b) K Fit

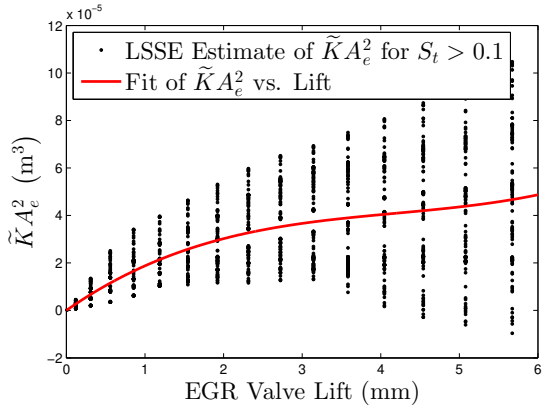

(c) $\widetilde{K}$ Fit

Figure 2.11: LP-EGR estimation error and K and $\widetilde{K}$ fits for the compressible flow unsteady orifice equation with the $\partial\rho/\partial t \approx 0$ assumption. Target EGR estimation error bounds are shown as dashed red lines.

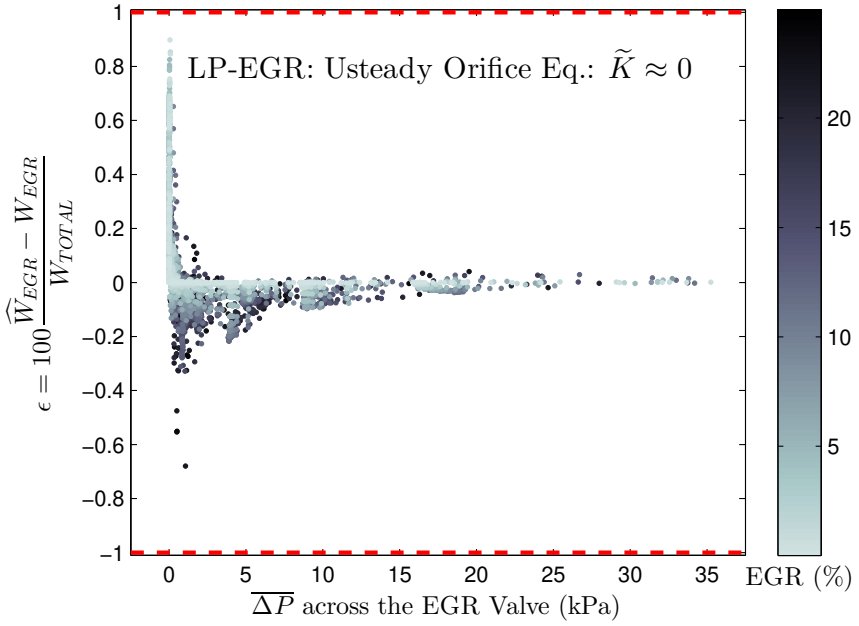

(a) LP-EGR Estimation Error

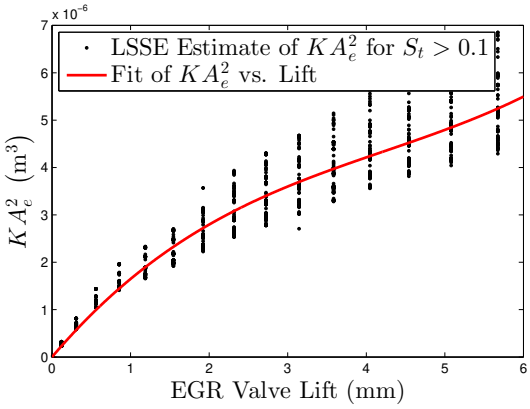

(b) K Fit

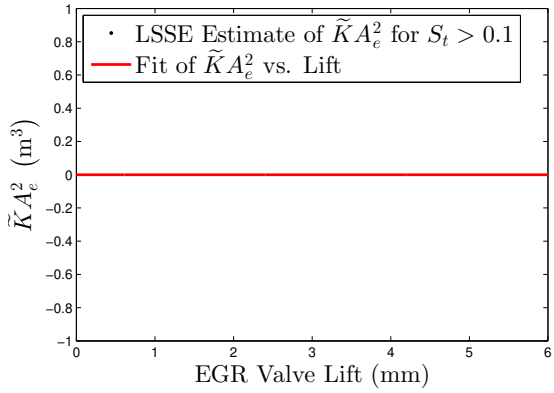

(c) $\widetilde{K}$ Fit

Figure 2.12: LP-EGR estimation error and K and $\widetilde{K}$ fits for the compressible flow unsteady orifice equation with the $\widetilde{K} \approx 0$ assumption. Target EGR estimation error bounds are shown as dashed red lines.

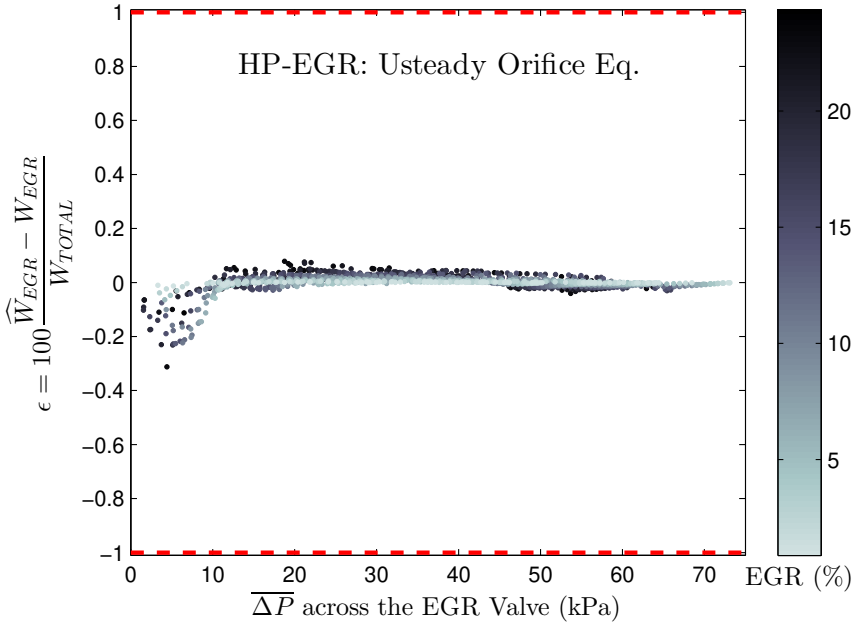

(a) HP-EGR Estimation Error

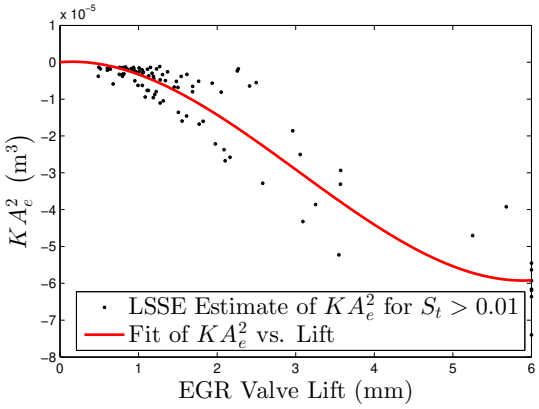

(b) K Fit

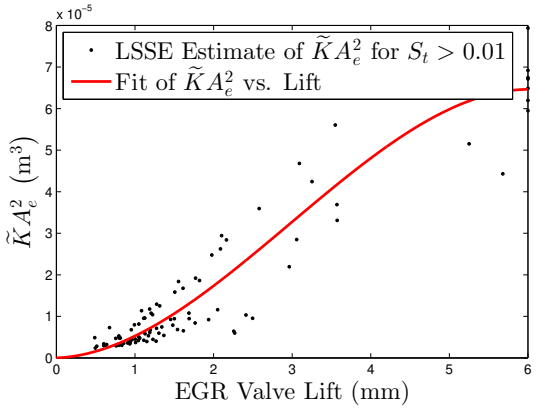

(c) $\widetilde{K}$ Fit

Figure 2.13: HP-EGR estimation error and K and $\widetilde{K}$ fits for the compressible flow unsteady orifice equation. Target EGR estimation error bounds are shown as dashed red lines.

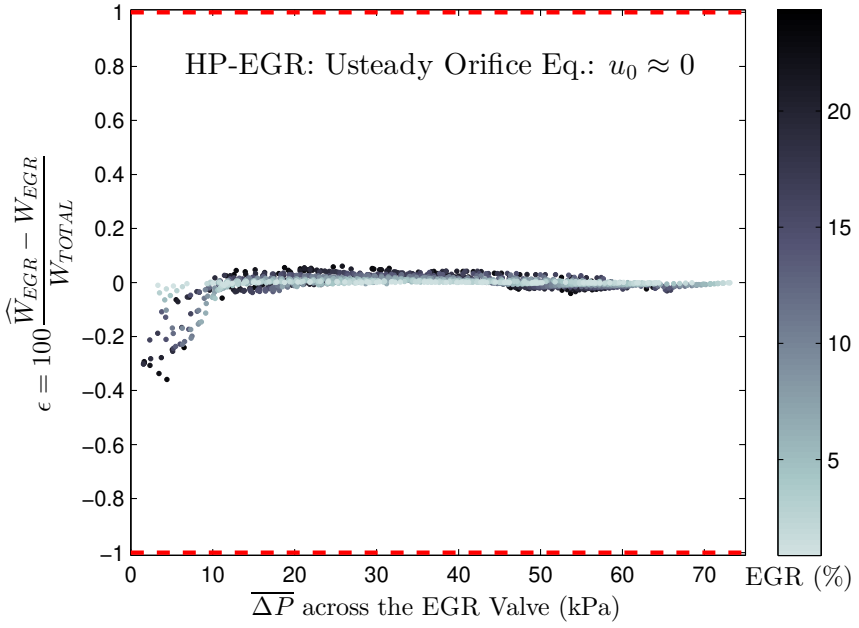

(a) HP-EGR Estimation Error

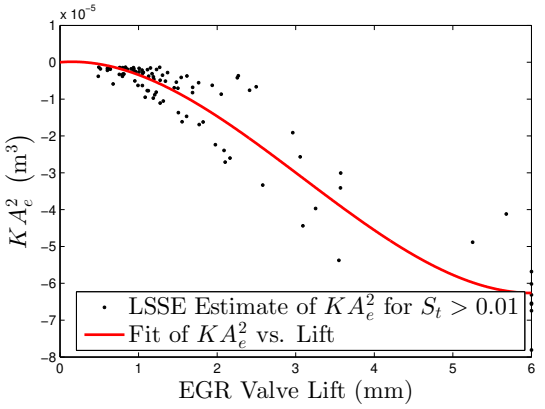

(b) K Fit

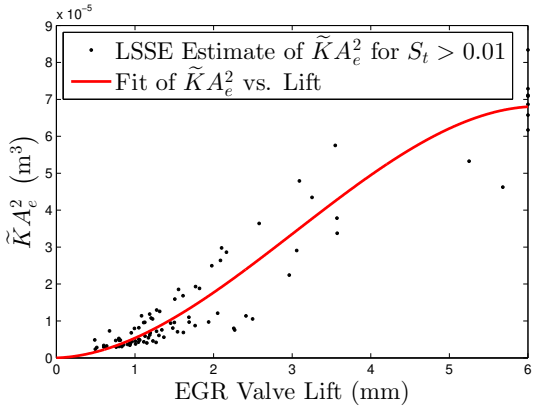

(c) $\widetilde{K}$ Fit

Figure 2.14: HP-EGR estimation error and K and $\widetilde{K}$ fits for the compressible flow unsteady orifice equation with the $u_0 \approx 0$ assumption. Target EGR estimation error bounds are shown as dashed red lines.

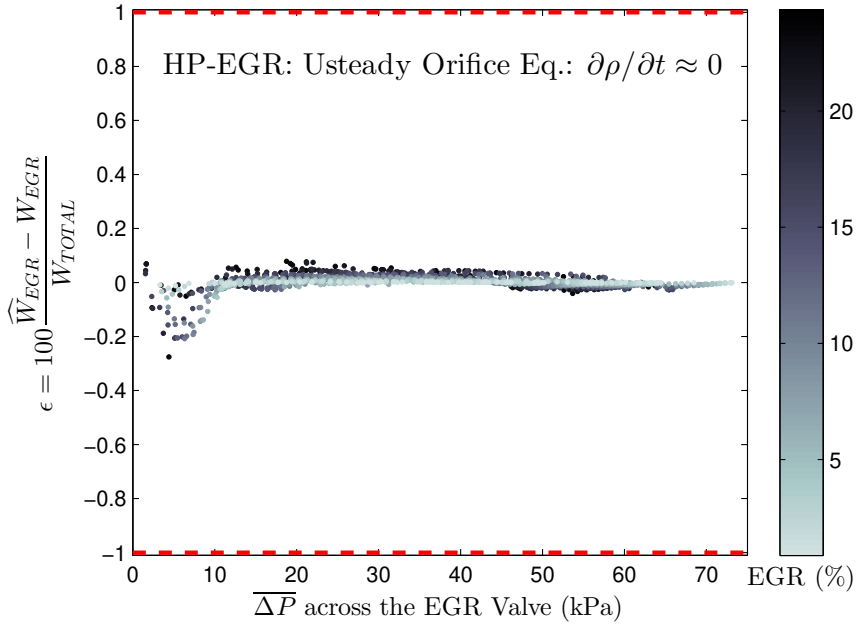

(a) HP-EGR Estimation Error

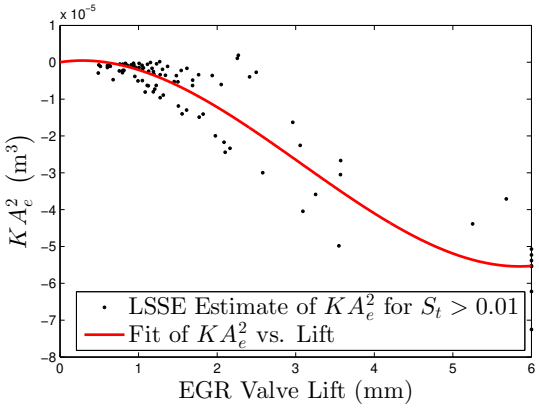

(b) K Fit

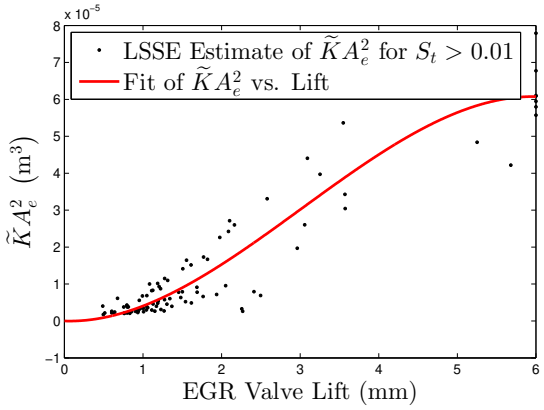

(c) $\widetilde{K}$ Fit

Figure 2.15: HP-EGR estimation error and K and $\widetilde{K}$ fits for the compressible flow unsteady orifice equation with the $\partial\rho/\partial dt \approx 0$ assumption. Target EGR estimation error bounds are shown as dashed red lines.

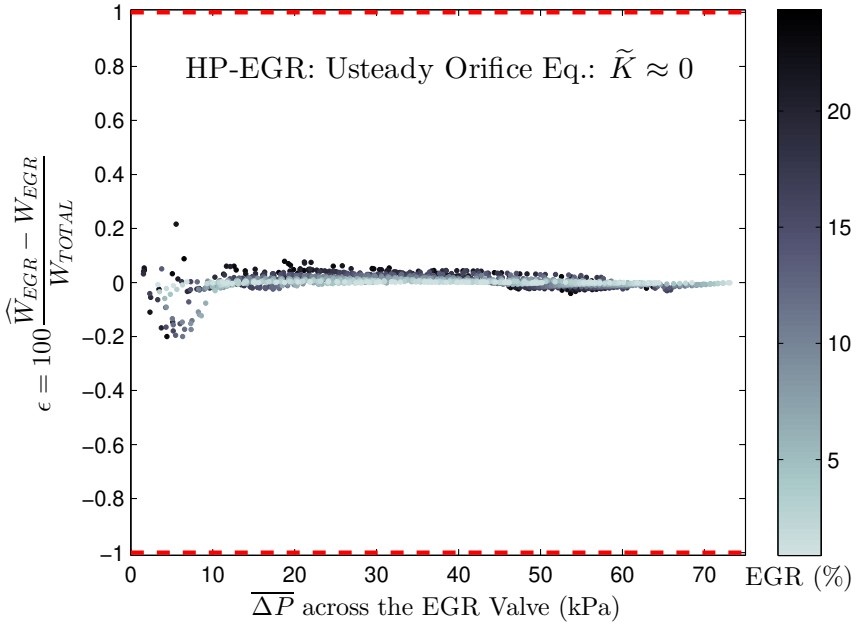

(a) HP-EGR Estimation Error

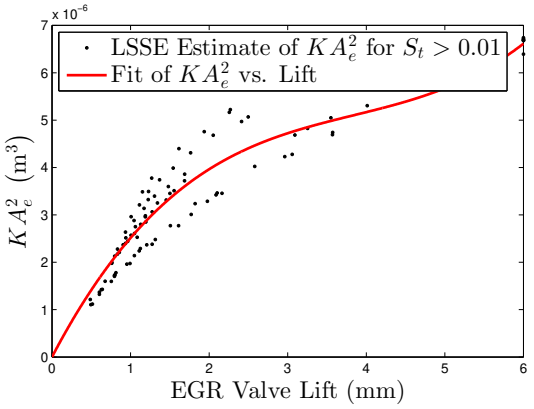

(b) K Fit

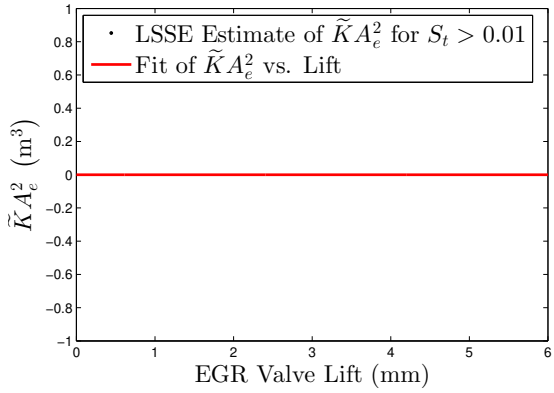

(c) $\widetilde{K}$ Fit

Figure 2.16: HP-EGR estimation error and K and $\widetilde{K}$ fits for the compressible flow unsteady orifice equation with the $\widetilde{K} \approx 0$ assumption. Target EGR estimation error bounds are shown as dashed red lines.

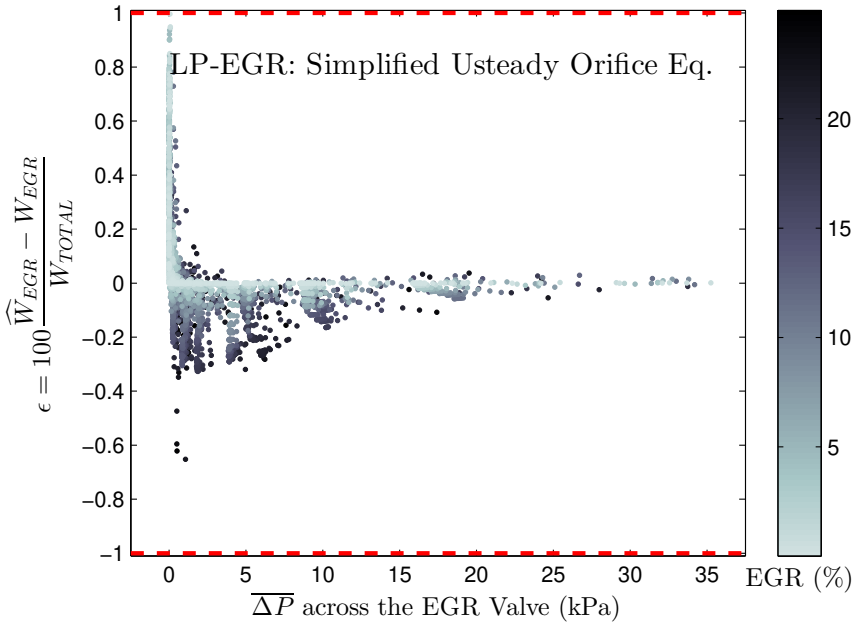

(a) LP-EGR Estimation Error

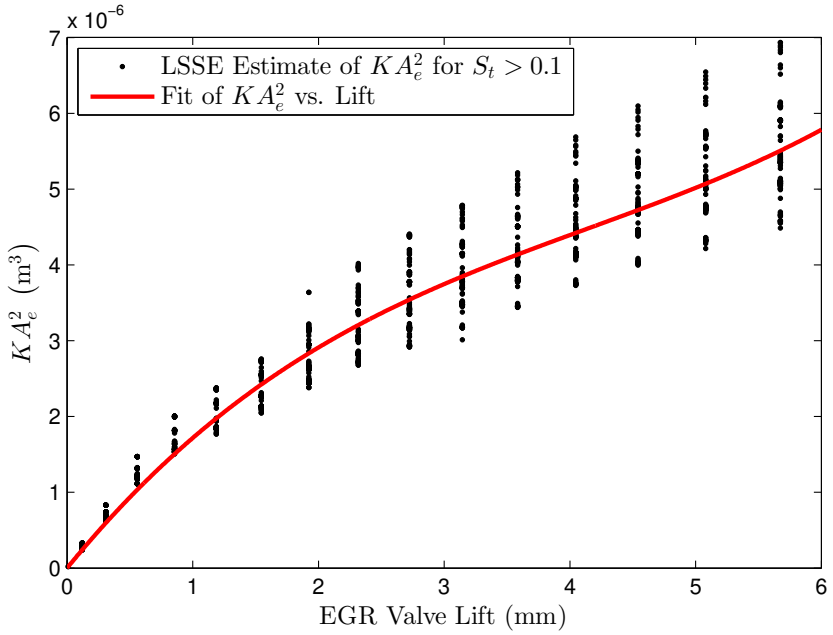

(b) K Fit

Figure 2.17: LP-EGR estimation error and K fit for the simplified compressible flow unsteady orifice equation. Target EGR estimation error bounds are shown as dashed red lines.

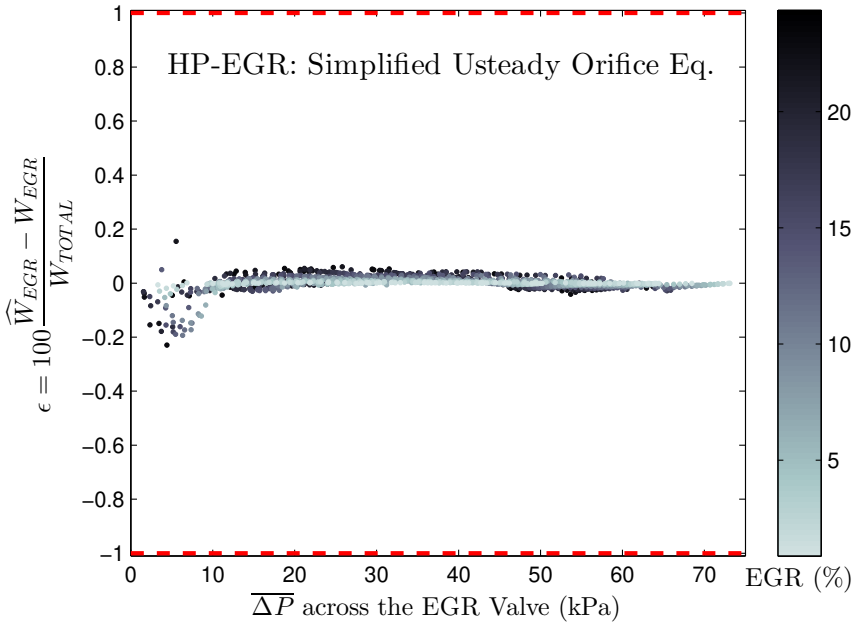

(a) HP-EGR Estimation Error

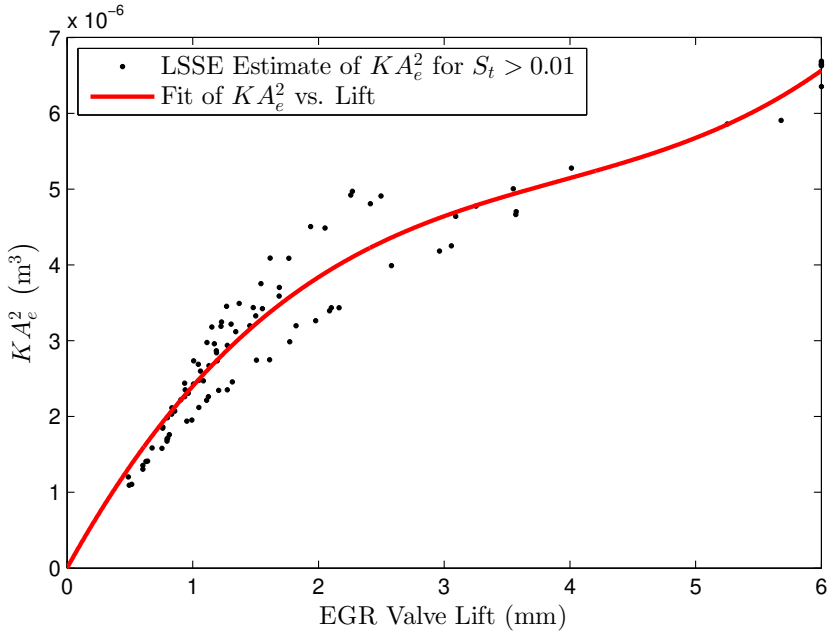

(b) K Fit

Figure 2.18: HP-EGR estimation error and K fit for the simplified compressible flow unsteady orifice equation. Target EGR estimation error bounds are shown as dashed red lines.

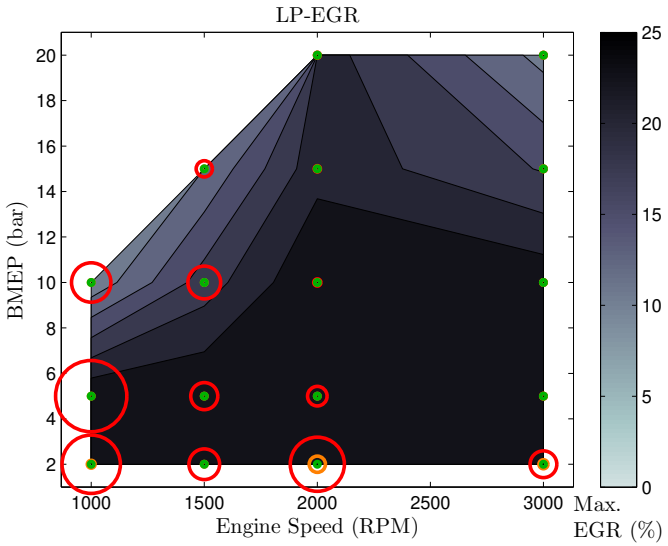

Figure 2.19: Contours of the maximum achievable LP-EGR percentage at simulated engine operating points. The corresponding LP-EGR estimation errors are represented by circles whose radii are proportional to the error using the steady orifice (red, up to 13.2%), quasi-steady (orange, up to 3.0%) and unsteady (green, up to 0.6%) orifice equations.

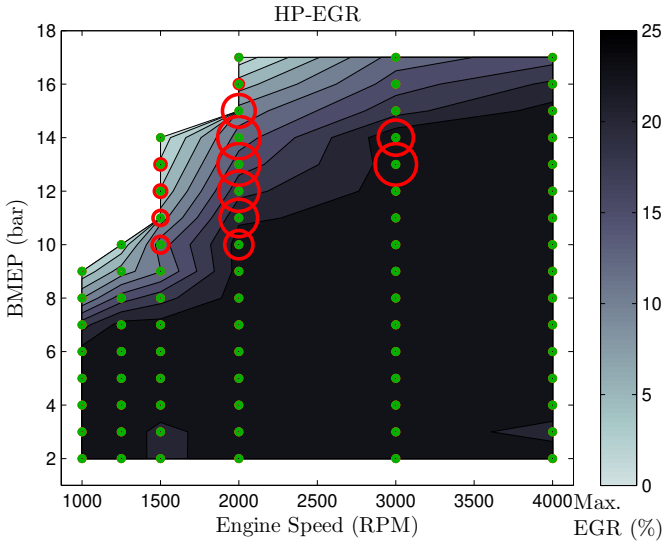

Figure 2.20: Contours of the maximum achievable HP-EGR percentage at simulated engine operating points. The corresponding HP-EGR estimation errors are represented by circles whose radii are proportional to the error using the steady orifice (red, up to 7.8%), quasi-steady (orange, up to 0.6%) and unsteady (green, up to 0.2%) orifice equations.

CHAPTER III

Practical Implementation of EGR Flow Estimation

The analysis in Chapter II shows the need to measure the instantaneous input parameters: pressures and temperature upstream and downstream of the EGR valve or orifice for accurate EGR estimation accuracy. Further accuracy gains are possible by accounting for inertial effects using the unsteady orifice equation. The practical implementation of EGR estimation is discussed in this chapter.

Acquiring all instantaneous input parameters can be expensive. The slow response of typical temperature sensors used for engine applications results in an effectively averaged temperature measurement. Fast-sampling of multiple measurements can be taxing on the engine control unit (ECU) and requires more expensive sensors with faster response. Furthermore, using the unsteady orifice equation involves solving a non-linear dynamic system which can be computationally expensive. It is of interest to avoid the non-linearity error while minimizing the number of fast-sampled measurements and their sampling frequencies, and to account for the inertial effect while reducing the computational cost. To that end, GT-Power simulation data is used to determine the optimal sensor configuration and evaluate less computationally expensive flow formulations. Experimental validation of the simulation results is then provided.

3.1 Pressure Measurement Configuration

Due to the slow response of typical engine temperature sensors, the temperature measurements at the EGR inlet and outlet are considered average values, while the optimal configuration of pressure sensors is investigated in detail. Existing compressor inlet and intake manifold absolute pressure (p) sensors can provide the pressure measurement at the EGR valve outlet (p_o) on a LP and HP-loop respectively. The second pressure measurement can be obtained via an additional absolute p-sensor

at the EGR valve inlet (p_i), or a ΔP sensor across it. The various pressure sensor configurations are summarized in Table (3.1). An over-bar is used to indicate if the pressure measurement is averaged; otherwise it is fast-sampled at every crank angle. The feasibility of using more practical sampling frequencies is investigated in subsequent sections. Table (3.1) also shows the $\overline{\Delta P}$ lower bound required to keep 99.7% (3 σ) of the EGR estimation errors within $\pm 1\%$ using the unsteady orifice equation for both LP and HP cases.

Config. Number	1st Pressure Sensor	2nd Pressure Sensor	LP-EGR $\overline{\Delta P}$ Lower Bound (kPa)	HP-EGR $\overline{\Delta P}$ Lower Bound (kPa)
1	$p_o(t)$	$p_i(t)$	0	< 1.5
2	$\overline{p_o(t)}$	$p_i(t)$	5.7	5.5
3	$p_o(t)$	$\overline{p_i(t)}$	10.1	8.4
4	$\overline{p_o(t)}$	$\overline{p_i(t)}$	10.1	9.2
5	$p_o(t)$	$\Delta P(t)$	0	< 1.5
6	$\overline{p_o(t)}$	$\Delta P(t)$	0	< 1.5
7	$p_o(t)$	$\overline{\Delta P(t)}$	10.1	9.2
8	$\overline{p_o(t)}$	$\overline{\Delta P(t)}$	10.1	9.2

Table 3.1: Pressure sensor configurations considered with the resulting $\overline{\Delta P}$ lower bound required to keep the LP and HP-EGR estimation error within $\pm 1\%$ (obtained using GT-Power simulations).

Figures (3.1) and (3.2) show EGR estimation error corresponding to the pressure sensor configurations 1 through 3 and 5 through 7 from Table (3.1); configurations 4 and 8 are identical to the steady orifice equation with averaged inputs presented in Chapter II Figures (2.4) and (2.5) and are not repeated here. Configurations 1 and 5 use two fast-sampled measurements each: $p_o(t)$ and $p_i(t)$ or $p_o(t)$ and $\Delta P(t)$. Their corresponding EGR estimation error is therefore identical assuming no pressure measurement error as $p_o(t)$ and $p_i(t)$ can be computed from $p_o(t)$ and $\Delta P(t)$. Figures (3.1(a)), (3.1(b)), (3.2(a)) and (3.2(b)) show similar EGR estimation errors for both pressure sensor configurations 1 and 5 compared to the unsteady orifice equation from Chapter II where all inputs including temperature are fast-sampled (Figures (2.6) and (2.7)). The impact of averaged temperature measurements on the non-linearity error is therefore negligible.

Table (3.1) and Figures (3.1) and (3.2) also show that pressure sensor configuration 7

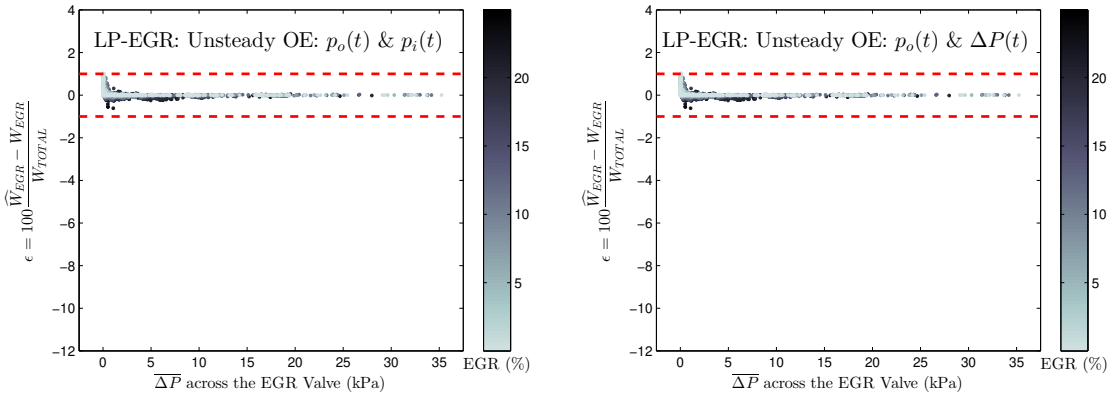

(a) Configuration 1

(b) Configuration 5

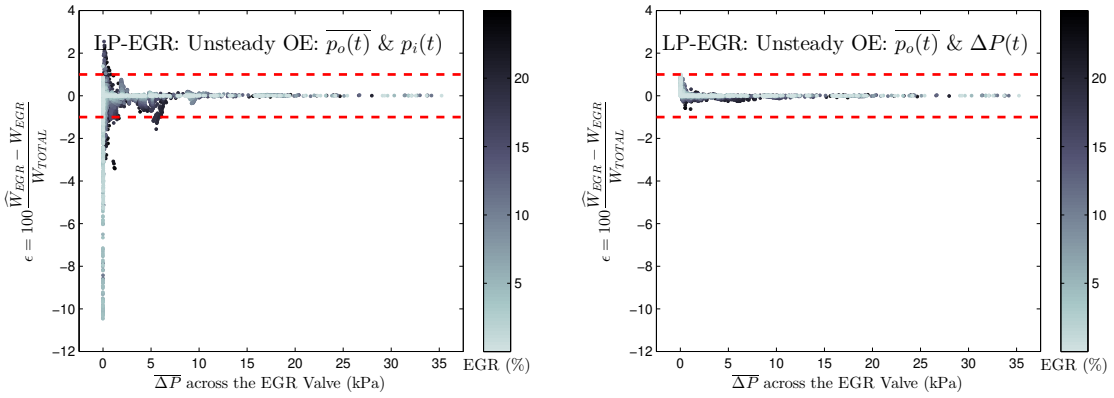

(c) Configuration 2

(d) Configuration 6

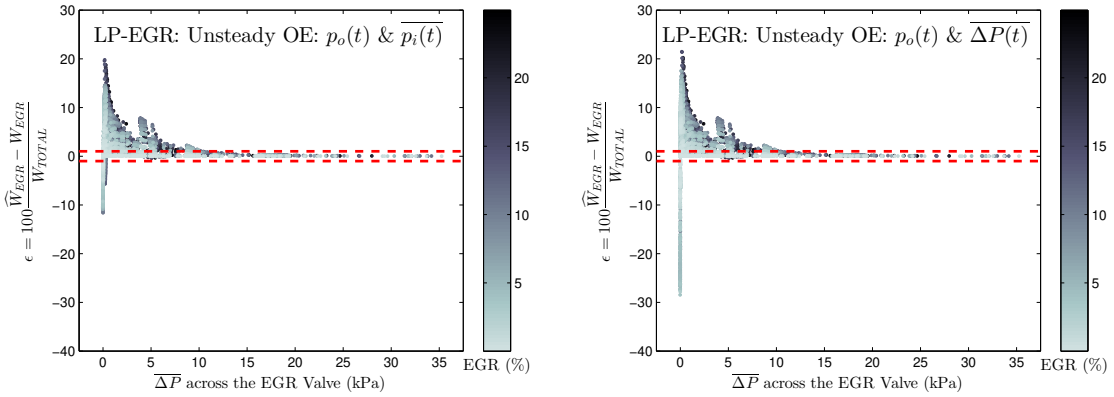

(e) Configuration 3

(f) Configuration 7

Figure 3.1: LP-EGR estimation error for the compressible flow unsteady orifice equation for different pressure sensor configurations. Fast sampling of both two inlet and outlet $p-$sensors is needed. In case a ΔP sensor is used, only fast sampling of the ΔP sensor is required.

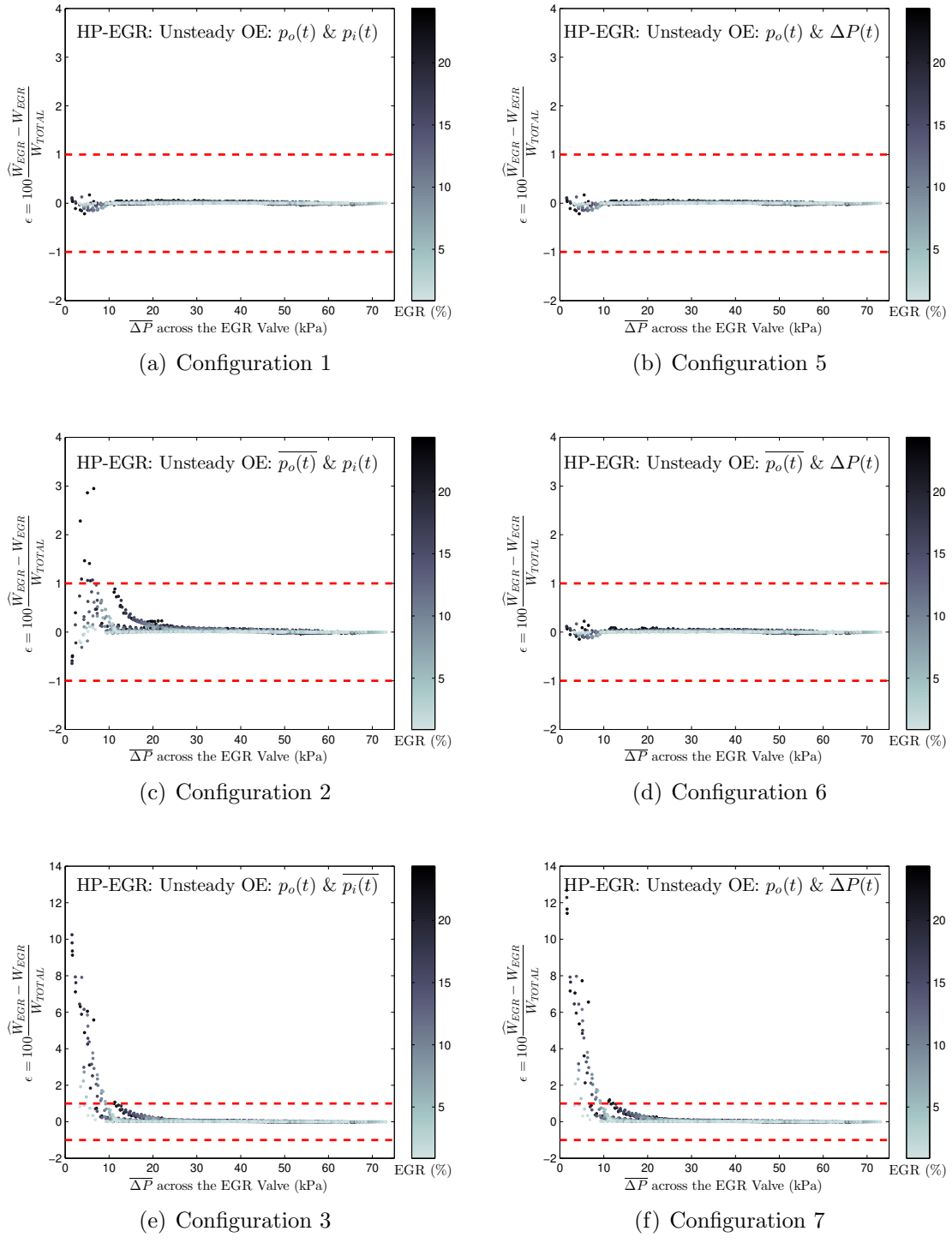

(a) Configuration 1

(b) Configuration 5

(c) Configuration 2

(d) Configuration 6

(e) Configuration 3

(f) Configuration 7

Figure 3.2: HP-EGR estimation error for the compressible flow unsteady orifice equation for different pressure sensor configurations. Fast sampling of both two inlet and outlet $p-$sensors is needed. In case a ΔP sensor is used, only fast sampling of the ΔP sensor is required.

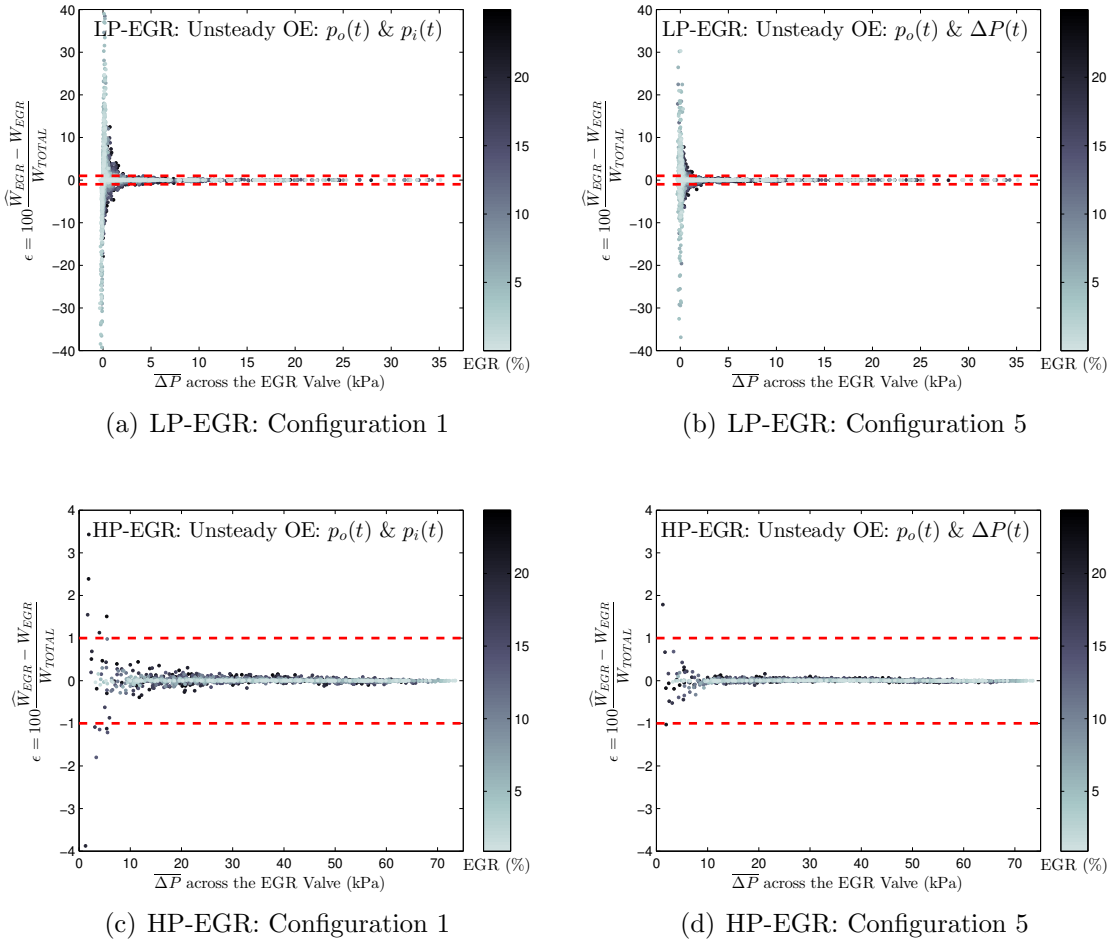

(a) LP-EGR: Configuration 1

(b) LP-EGR: Configuration 5

(c) HP-EGR: Configuration 1

(d) HP-EGR: Configuration 5

Figure 3.3: LP and HP-EGR estimation error for the compressible flow unsteady orifice equation with pressure sensor measurement errors. Pressure measurement errors of ±0.1% FSO are considered.

($\overline{p_o(t)}$ and $\Delta P(t)$) where only the ΔP sensor is fast-sampled yields similar EGR estimation errors compared to configurations 1 ($p_o(t)$ and $p_i(t)$) and 5 ($p_o(t)$ and $\Delta P(t)$) where both pressure sensors are fast-sampled. Fast-sampling of only one measurement is not sufficient if two absolute pressure sensors are used (configurations 2 and 3). This can be expected given that the orifice equation is highly non-linear in ΔP where the slope of the $\widetilde{\Psi}()$ function approaches ∞ as ΔP approaches 0. The requirement of only one fast-sampled measurement favors the use of a ΔP sensor compared to two $p-$sensors.

Figure (3.3) shows the EGR estimation error for pressure sensor configurations 1 ($p_o(t)$ and $p_i(t)$) and 5 ($p_o(t)$ and $\Delta P(t)$) but with added pressure measurement error. A measurement error of ±0.1% of sensor full scale output (FSO) is considered.

Full scale output values of 1 ($\pm$0.5) and 1.5 ($\pm$0.75) bar are used for the ΔP sensor for LP and HP-EGR, and 1.5 and 3 bar are used to the absolute pressure sensors for LP and HP-EGR respectively. Better accuracy is achieved with the use of a ΔP sensor instead of two absolute $p-$sensors. Table (3.2) shows the $\overline{\Delta P}$ lower bound required to keep the EGR estimation error within $\pm$1%. A larger FSO is required for the absolute $p-$sensors resulting in larger measurement errors. The errors can add up leading to even larger error in the computed $\Delta P = p_i - p_o$. The sensitivity of the $\widetilde{\Psi}()$ function to ΔP is higher than that to p_o and p_i, so the lower ΔP error achieved by using a ΔP sensor explains the lower EGR estimation errors. A pressure sensor configuration with a fast-sampled ΔP across the EGR valve, and an averaged absolute pressure outlet measurement (p_o) is the configuration of choice as it results in the highest accuracy with the minimal possible cost.

Config. Number	1st Pressure Sensor	2nd Pressure Sensor	LP-EGR $\overline{\Delta P}$ Lower Bound (kPa)	HP-EGR $\overline{\Delta P}$ Lower Bound (kPa)
1	$p_o(t)$	$p_i(t)$	2.5	4.0
5	$p_o(t)$	$\Delta P(t)$	1.5	< 1.5

Table 3.2: Various pressure sensor configurations with the resulting $\overline{\Delta P}$ lower bound required to keep the LP and HP-EGR estimation error within $\pm$1%. Pressure measurement errors of $\pm$0.1% FSO are considered.

3.2 Approximations of the Unsteady Orifice Equation

The unsteady orifice equation is capable of capturing the inertial effects and improving EGR estimation accuracy. However, it involves solving a non-linear dynamic system and is more computationally expensive than the quasi-steady orifice equation. It is desirable to find simpler formulations capable of approximating the inertial effect for control purposes. In this section, four approximations to the unsteady orifice equation are proposed and evaluated.

3.2.1 Approximation (I): Steady Orifice Equation with Uniform Filtering

The quasi-steady orifice equation (Eq. (2.31)) can be used to approximate the unsteady orifice equation (Eq. (2.35)) by appropriate low-pass filtering of the ΔP signal. The lag in ΔP introduced by the low-pass filter can mimic the flow lag due to inertia and approximates the transient effects. A similar practice can be found in

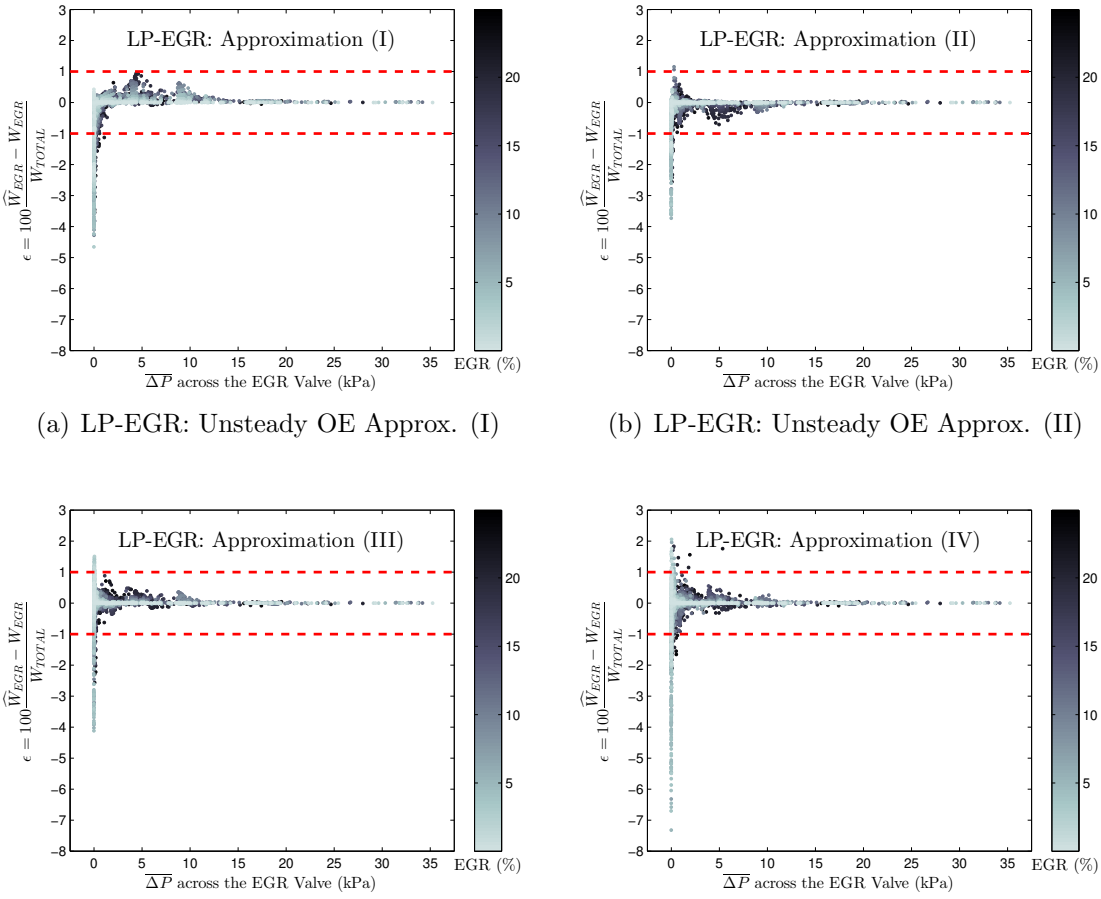

(a) LP-EGR: Unsteady OE Approx. (I)

(b) LP-EGR: Unsteady OE Approx. (II)

(c) LP-EGR: Unsteady OE Approx. (III)

(d) LP-EGR: Unsteady OE Approx. (IV)

Figure 3.4: LP-EGR estimation error for the unsteady orifice equation approximations (I) through (IV). The dashed red lines show the $\pm 1\%$ error bound.

the work of Grietzer [42] on modeling compressor surge where a lag in the pressure ratio was introduced to account for transient effects.

Using a 1^{st} order low-pass filter, the optimal cut-off frequency (f_c) to best approximate the inertial effect is dependent on the operating condition. An f_c of 205 Hz was found to be a good middle-ground solution for the simulated cases as it results in the lowest $\overline{\Delta P}$ lower bound for filter cut-off frequencies swept from 60 Hz to 2.5 kHz. Figures (3.4(a)) and (3.5(a)) show the EGR estimation error (ϵ) for the LP and HP-EGR configurations. A lower bound on $\overline{\Delta P}$ of 0.3 kPa is required to keep ϵ within $\pm 1\%$ for the LP-EGR case; ϵ lies within the $\pm 1\%$ bound for all simulated $\overline{\Delta P}$ for the HP-EGR case (lowest simulated $\overline{\Delta P} \approx 1.5$ kPa).

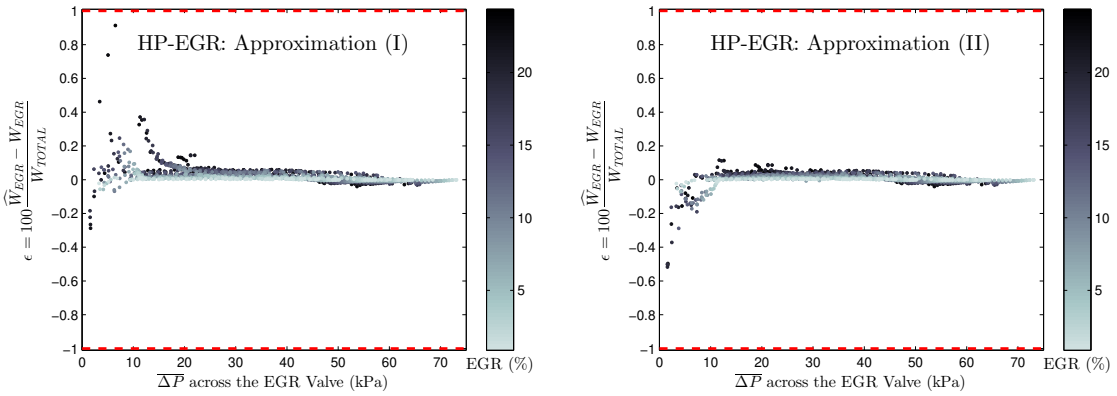

(a) HP-EGR: Unsteady OE Approx. (I)

(b) HP-EGR: Unsteady OE Approx. (II)

(c) HP-EGR: Unsteady OE Approx. (III)

(d) HP-EGR: Unsteady OE Approx. (IV)

Figure 3.5: HP-EGR estimation error for the unsteady orifice equation approximations (I) through (IV). The dashed red lines show the $\pm 1\%$ error bound.

3.2.2 Approximation (II): Steady Orifice Equation with Variable Filtering

To better approximate the inertial effects with a 1st order low pass filter proposed in Approximation (I), a filter with varying cut-off frequency is considered. The relation between the best filter bandwidth (f_c) and the flow variables can be derived analytically. For simplicity, the unsteady incompressible orifice equation is considered (Eq. (2.7)), which when accounting for flow reversals can be expressed as:

$$2A_e^2\rho K\frac{d}{dt}W + W\left|W\right| = 2A_e^2\rho\Delta P \tag{3.1}$$

We seek to approximate the unsteady formulation with the steady orifice equation using a filtered differential pressure signal ΔP_f:

$$W\left|W\right| = 2A_e^2\rho\Delta P_f \tag{3.2}$$

Differentiating Eq. (3.2) with respect to time gives:

$$\frac{d}{dt}W = \frac{1}{2}\sqrt{\frac{2A_e^2\rho}{|\Delta P_f|}}\frac{d}{dt}\Delta P_f \tag{3.3}$$

Substituting Eq. (3.3) into Eq. (3.1) gives a 1st order differential equation in ΔP_f:

$$\frac{K}{2}\sqrt{\frac{2A_e^2\rho}{|\Delta P_f|}}\frac{d}{dt}\Delta P_f + \Delta P_f = \Delta P \tag{3.4}$$

The resulting 1st order dynamic equation in ΔP_f is nonlinear. Nevertheless, it indicates that an approximate linear 1st order filter has a cut-off frequency (f_c) that is proportional to $\sqrt{|\Delta P|}$ and inversely proportional to $KA_e\sqrt{\rho}$. Neglecting the impact of the variation in the density (ρ), a case-varying cut-off frequency:

$$f_c = \frac{C}{KA_e}\sqrt{\overline{|\Delta P|}} \tag{3.5}$$

is used where C is a tunable constant. The value of C was swept from 0.1 to 2; a C value of 0.235 is found to be optimal for the simulated cases, resulting in a lower bound on $\overline{\Delta P}$ of 0.1 kPa required to keep the LP-EGR estimation error ϵ within $\pm 1\%$ (Fig. (3.4(b))). The HP-EGR estimation error lies within the $\pm 1\%$ bound for all simulated $\overline{\Delta P}$ (Fig. (3.4(b))).

3.2.3 Approximation (III): Pseudo-Unsteady Orifice Equation

The unsteady orifice equation (Eq. (2.35)) can be rearranged as:

$$W = \sqrt[\pm]{\widetilde{\Psi}|\widetilde{\Psi}|\left(\Delta P\right) - KC_D^2 A_T^2 \widetilde{\Phi}\left(\Delta P\right)\frac{dW}{dt}} \tag{3.6}$$

where the signed square-root $\sqrt[\pm]{x}$ is defined as $\text{sign}(x)\sqrt{|x|}$. Variables p_o, T_i and T_o are dropped from $\widetilde{\Psi}$ and $\widetilde{\Phi}$ for brevity. Using Approximation (I) to express dW/dt in Eq. (3.6) gives Approximation (III):

$$W \approx \sqrt[\pm]{\widetilde{\Psi}|\widetilde{\Psi}|\left(\Delta P\right) - KC_D^2 A_T^2 \widetilde{\Phi}\left(\Delta P\right)\frac{d\widetilde{\Psi}\left(\Delta P_f\right)}{dt}} \tag{3.7}$$

where ΔP_f is the filtered ΔP using a 1$^{\text{st}}$ order low pass filter with a uniform cut-off frequency f_c. The value of f_c was swept from 20 to 700 Hz to determine an optimal cut-off frequency f_c of 180 Hz, resulting in a LP-EGR $\overline{\Delta P}$ lower bound of 0.1 kPa required for $|\epsilon| < 1\%$ (Fig. (3.4(c))). The HP-EGR estimation error lies within the $\pm 1\%$ bound for all simulated $\overline{\Delta P}$ (Fig. (3.5(c))).

3.2.4 Approximation (IV): Pseudo-Unsteady Orifice Equation with Square Root Approximation

Factoring $\widetilde{\Psi}\left(\Delta P\right)$ out of the square-root in Eq. (3.7) gives:

$$W \approx \widetilde{\Psi}\left(\Delta P\right)\sqrt[\pm]{1 - \frac{KC_D^2 A_T^2 \widetilde{\Phi}\left(\Delta P\right)}{\widetilde{\Psi}|\widetilde{\Psi}|\left(\Delta P\right)}\frac{d\widetilde{\Psi}\left(\Delta P_f\right)}{dt}} \tag{3.8}$$

The transient term is small compared to $\widetilde{\Psi}|\widetilde{\Psi}|\left(\Delta P\right)$ under most circumstances, so we can use the square-root approximation $\sqrt{1+\epsilon} \approx 1 + \epsilon/2$ to generate Approximation (IV):

$$W \approx \widetilde{\Psi}\left(\Delta P\right) - \frac{KC_D^2 A_T^2 \widetilde{\Phi}\left(\Delta P\right)}{2|\widetilde{\Psi}|\left(\Delta P\right)}\frac{d\widetilde{\Psi}\left(\Delta P_f\right)}{dt} \tag{3.9}$$

Similar to Approximation (III), ΔP_f is the filtered ΔP using a 1$^{\text{st}}$ order low pass filter with a uniform cut-off frequency f_c. Sweeping the value f_c from 15 to 550 Hz, an optimal f_c of 70 Hz is found. Fig. (3.4(d)) shows the EGR estimation error ϵ plotted versus $\overline{\Delta P}$. To keep ϵ within $\pm 1\%$, a lower bound of 0.6 kPa on $\overline{\Delta P}$ is required for the LP-EGR system. The HP-EGR estimation error lies within the $\pm 1\%$ bound for all simulated $\overline{\Delta P}$ (Fig. (3.5(d))).

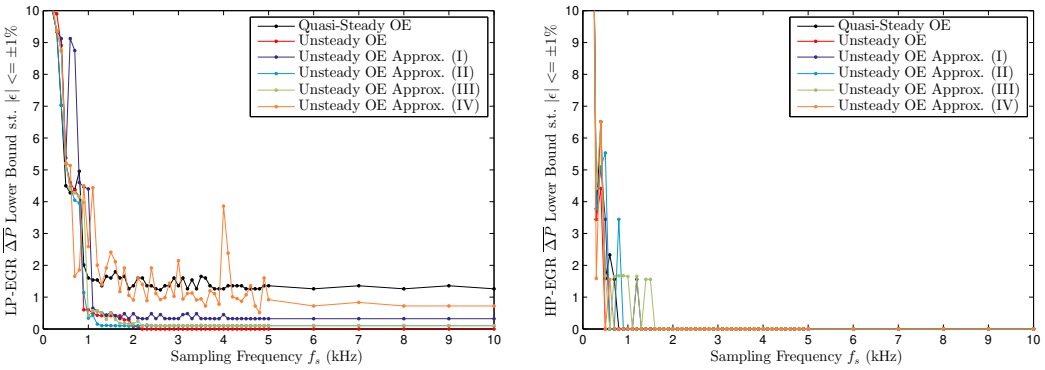

(a) LP-EGR: $\overline{\Delta P}$ vs f_s

(b) HP-EGR: $\overline{\Delta P}$ vs f_s

Figure 3.6: $\overline{\Delta P}$ lower bound required to keep the EGR estimation error within $\pm 1\%$ as a function of ΔP sampling frequency obtained using different orifice equation (OE) flow formulations.

3.3 Sampling Frequency Requirement

The previous simulation results used ΔP sampled at every CA to represent instantaneous ΔP signals; however, this corresponds to sampling frequencies between 6 and 24 kHz for the engine speeds considered (1000 to 4000 RPM). This may be too demanding for current ECU's, or expensive enough to prohibit implementation. Therefore, it is desirable to find the minimum sampling frequency f_s capable of achieving the benefit observed with CA-resolved ΔP. To this end, the instantaneous ΔP signal from GT-Power was down-sampled using different sampling frequencies ranging from 0.1 to 10 kHz. Fig. (3.6) shows the $\overline{\Delta P}$ lower bound plotted versus the sampling frequency f_s for both LP and HP-EGR systems. Most of the benefit is achieved with an f_s of around 1 kHz, while an f_s of 2 kHz is required to achieve the full benefit of the unsteady orifice equation for the LP-EGR case. Table (3.3) summarizes the frequency required to get the full benefit for each flow formulation. Finally, it should be noted here that the discretization time used to numerically solve the unsteady orifice was the same as the sampling interval. This is done with the use of an implicit formulation of the ordinary differential equation (ODE); the use of an explicit formulation requires finer discretization times. Using the same discretization time as the sampling interval results in a sampling frequency requirement of 9 kHz for the explicit formulation of the unsteady orifice equation to be stable.

Formulation	LP-EGR Sampling Freq. Requirement (kHz)	HP-EGR Sampling Freq. Requirement (kHz)
Steady Orifice Eq.	≥ 1.0	≥ 0.8
Unsteady Orifice Eq.	≥ 2.0	≥ 0.5
Unsteady Approx. (I)	≥ 1.1	≥ 1.3
Unsteady Approx. (II)	≥ 1.2	≥ 0.9
Unsteady Approx. (III)	≥ 1.0	≥ 1.6
Unsteady Approx. (IV)	≥ 5.0	≥ 0.7

Table 3.3: LP and HP-EGR sampling frequency requirement.

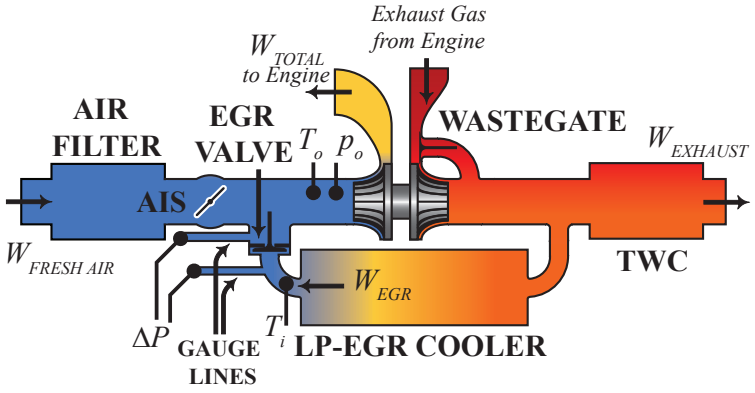

Figure 3.7: LP-EGR configuration showing the flow rates and sensor measurements of interest.

3.4 Experimental Validation

The performance of the EGR estimation methods based on the simulation results discussed previously is validated with several experimental studies. The valve effective area is also fit.

3.4.1 LP-EGR Experimental Setup

The experimental setup used to validate the LP-EGR GT-Power simulations incorporated a Ford 1.6L EcoBoost engine modified by adding a LP-EGR system. The LP-EGR loop includes an EGR cooler, a poppet EGR valve and an AIS throttle. This is consistent with the configuration used in the GT-Power model. A ± 2.5 psi ($\approx \pm 17$ kPa) Kistler piezoresistive ΔP sensor with a bandwidth of 2 kHz was mounted across the LP-EGR valve and sampled at 10 kHz. Sampling at a sufficiently

high frequency like 10 kHz allows us to investigate the impact of various sampling frequencies (< 10 kHz) on the EGR estimation error by down-sampling the ΔP signal in post-processing. Similarly, the high sensor bandwidth allows us to study the impact of various filter bandwidths (< 2 kHz) on the EGR estimation by applying the filtering in post-processing. The ΔP gauge-lines were kept below 12 cm to minimize gauge-line distortions of the ΔP signal [51]. The EGR loop instrumentation also included thermocouples installed on both sides of the valve, and an absolute pressure sensor installed at the compressor inlet downstream of the AIS throttle (Fig. (3.7)). The thermocouples and the absolute pressure sensor were sampled at only 10 Hz. These ΔP, pressure and temperature measurements were used in the different formulations presented in this work to estimate the EGR flow rate $\widehat{W}_{EGR}$.

An AVL emissions bench was used to measure the CO_2 concentrations pre-throttle and in the exhaust manifold so that the molar EGR fraction can be computed using:

$$[\text{EGR}] = \frac{[\text{CO}_{2,i}] - [\text{CO}_{2,a}]}{[\text{CO}_{2,e}] - [\text{CO}_{2,a}]} \tag{3.10}$$

where $[\text{CO}_{2,i}]$, $[\text{CO}_{2,e}]$ and $[\text{CO}_{2,a}]$ are the intake (measured pre-throttle), exhaust and ambient CO_2 molar or volume (wet) concentrations respectively. Using the bench fuel flow measurement, the ECU equivalence ratio (λ) measurement (from the universal exhaust-gas oxygen (UEGO) sensor), and the fuel's stoichiometric air-to-fuel ratio (obtained from testing the fuel), the engine air mass flow rate can be computed. Converting the EGR molar fraction from Eq. (3.10) into EGR mass fraction, and using the calculated engine air mass flow rate, the EGR mass flow rate W_{EGR} was computed. The EGR estimation error ϵ can be then obtained using Eq. (2.5).

Data was collected for 4 different EGR valve positions: 10, 30, 50 and 70% open. The engine was operated at engine speeds between 1000 and 3000 RPM, and engine loads between 2 and 15 bar BMEP with each of the 4 EGR valve positions. At each valve lift, engine speed and load combination, the AIS throttle opening was swept starting from wide open, and gradually closed until one of these conditions was met:

1. EGR percentage exceeds 20%.
2. Coefficient of variation (COV) of the indicated mean effective pressure (IMEP) exceeds 10%.
3. The pressure downstream the AIS throttle drops below -8 kPa (gauge).

The 3$^{\text{rd}}$ condition was required to avoid excessive oil leakage. The setup was equipped with a back pressure valve that was set at the position that generates a back pressure

representative of that of the exhaust path on a vehicle (with the catalyst and muffler). Finally, an additional data point with the engine turned off and the EGR valve open was collected to correct for the ΔP sensor offset error. Under this condition, the actual ΔP is zero, and the average measured value can be subtracted from the remaining ΔP signals to compensate for the measurement bias.

3.4.2 HP-EGR Experimental Setup

A similar experimental setup was used to validate the HP-EGR GT-Power simulations where a HP-EGR loop was added to the Ford 1.6L EcoBoost engine. The HP-EGR loop includes an EGR cooler and a poppet EGR valve. The EGR valve is identical to the one used on the LP-EGR loop. Instead of a ΔP sensor, two surface mounted Kistler piezoresistive absolute $p-$sensors were installed across the HP-EGR valve and sampled at every 0.1 crank angle. The same emissions bench was used to measure the CO_2 concentrations, but in this case, emissions samples were taken from the intake (instead of pre-throttle) and exhaust manifolds.

Data was collected for the same 4 different EGR valve positions: 10, 30, 50 and 70% open. The engine was operated at engine speeds between 1000 and 3000 RPM, and engine loads between 6 and 15 bar BMEP with each of the 4 EGR valve positions. An operating point was skipped if the EGR valve opening results in excessive EGR percentage or high COV, or if the load could not be achieved.

3.4.3 EGR Valve Effective Area Fit

Comprehensive manufacturer EGR flow data was not available nor was a steady flow bench available to calibrate the effective area of the EGR valve for different lifts and different ΔP's (both positive and negative). Therefore, the valve effective area $A_e = C_D A_T$ needs to be fitted from the engine pulsating flow data. It is convenient to define Ψ^* as the steady-orifice mass flow per unit area function:

$$\Psi^*\left(\Delta P, p_o, T_i, T_o\right) = \frac{\widetilde{\Psi}(p_i, p_o, T_i, T_o)}{A_e\left(\Delta P\right)} \tag{3.11}$$

where $\widetilde{\Psi}$ is defined in Eq. (2.31). The area term A_e is a function of the valve lift, but dependency of lift is not explicitly shown here as the proposed fit is applied to each subset of the collected data with a uniform EGR valve opening. The steady

compressible flow orifice equation can be written as:

$$W(t) = A_e\left(\Delta P(t)\right)\Psi^*\left(\Delta P(t)\right) \tag{3.12}$$

where the p_o, T_i and T_o terms are dropped for brevity. The limited steady flow data available for the EGR valve at pressure differentials of 2 and 5 kPa (Fig. (2.1)) show the dependency of A_e on ΔP, but are not sufficient to determine the shape and value of A_e over the (instantaneous) pressure differentials observed in the experiment. To allow the optimization to determine the shape of A_e versus ΔP, a 1-D look-up table is used. The effective area at each ΔP is interpolated from an area vector $\mathbf{a} = [a_n]_1^N$ tuned for a pre-chosen differential pressure vector $\boldsymbol{\delta}\mathbf{p} = [\delta p_n]_1^N$. The EGR valve effective A_e can now be expressed as:

$$A_e\left(\Delta P\right) = \left(\frac{\delta p_{n+1} - \Delta P}{\delta p_{n+1} - \delta p_n}\right) a_n + \left(\frac{\Delta P - \delta p_n}{\delta p_{n+1} - \delta p_n}\right) a_{n+1} \tag{3.13}$$

for $\delta p_n < \Delta P < \delta p_{n+1}$. Defining the function:

$$\mathcal{U}_n\left(\Delta P\right) = \begin{cases} 1 & \text{if } \delta p_n < \Delta P < \delta p_{n+1} \\ 0 & \text{Otherwise} \end{cases}, \tag{3.14}$$

the steady compressible flow orifice equation can be written as:

$$W(t) = \sum_{n=1}^{N-1} \mathcal{U}_n\left(\Delta P(t)\right) A_e\left(\Delta P(t)\right)\Psi^*\left(\Delta P(t)\right) \tag{3.15}$$

Defining the functions:

$$\begin{aligned} \psi_{0,n} &= \mathcal{U}_n\left(\Delta P(t)\right)\Psi^*\left(\Delta P(t)\right) \\ \psi_{1,n} &= \mathcal{U}_n\left(\Delta P(t)\right)\Delta P(t)\Psi^*\left(\Delta P(t)\right) \end{aligned}, \tag{3.16}$$

Eq. (3.15) can be expressed as:

$$\begin{aligned} W(t) = &\sum_{n=1}^{N-1} \mathcal{U}_n\left(\Delta P\right)\left(\frac{\delta p_{n+1} - \Delta P}{\delta p_{n+1} - \delta p_n}\right) a_n \Psi^*\left(\Delta P\right) \\ &+ \sum_{n=1}^{N-1} \mathcal{U}_n\left(\Delta P\right)\left(\frac{\Delta P - \delta p_n}{\delta p_{n+1} - \delta p_n}\right) a_{n+1}\Psi^*\left(\Delta P\right) \end{aligned}. \tag{3.17}$$

Eq. (3.17) can be rearranged into:

$$\begin{aligned} W(t) = & \left(\frac{\delta p_2 \psi_{0,1} - \psi_{1,1}}{\delta p_2 - \delta p_1} \right) a_1 \\ & + \sum_{n=2}^{N-1} \left(\frac{\delta p_{n+1} \psi_{0,n} - \psi_{1,n}}{\delta p_{n+1} - \delta p_n} + \frac{\delta p_{n-1} \psi_{0,n-1} - \psi_{1,n-1}}{\delta p_{n-1} - \delta p_n} \right) a_n \\ & + \left(\frac{\delta p_{N-1} \psi_{0,N-1} - \psi_{1,N-1}}{\delta p_{N-1} - \delta p_N} \right) a_N \end{aligned} \tag{3.18}$$

The terms $\psi_{0,n}$ and $\psi_{1,n}$ are a function of time, and their instantaneous values can be obtained experimentally using a fast sampled ΔP sensor. However, the EGR percentage and flow rate are computed based on the emission bench measurement of the intake and exhaust CO_2 concentrations, so $W(t)$ is unknown; only $\overline{W(t)}$ can be obtained given the experimental setup. Eq. (3.18) expresses $W(t)$ as a linear function of a_n's. Taking the time average of the right and left hand sides of Eq. (3.18), the measured average flow rate $\overline{W(t)}$ can be written as linear function in a_n where the coefficients are functions of the instantaneous $\Delta P(t)$:

$$\overline{W(t)} = \sum_{n=1}^{N} \overline{h_n(t)} a_n \tag{3.19}$$

where $h_n(t)$ denotes the coefficients of a_n in Eq. (3.18) for $n = 1, 2...N$, and therefore, the optimal a_n's that minimize the sum of square errors can be linearly regressed or obtained using a quadratic program.

Having M measurements of $\overline{W(t)}$ and $\Delta P(t)$ all performed at the same EGR valve lift, the coefficients $\mathbf{a} = [a_n]_1^N$ can be linearly regressed through Eq. (3.19) given that M is sufficiently larger than N. Unfortunately, the linear regression results in unphysical negative least sum of square error (LSSE) estimates of a_n's corresponding to near-zero δp's. The flow reversal lags behind the ΔP reversal, so there exist instants of time where the instantaneous flow $W(t)$ has the opposite sign of the instantaneous $\Delta P(t)$. Computing the effective area at these instants using a quasi-steady orifice equation results in an unphysical $A_e < 0$. Although the linear optimization does not have access to the instantaneous flow $W(t)$, it could be inferring negative a_n's at near-zero δp's to compensate for the inability of the quasi-steady orifice equation to capture inertial lag.

Equation (3.19) is linear in a_n, so the LSSE estimation can be easily formulated into a quadratic program. Upper and lower bounds on $\mathbf{a} = [a_n]_1^N$ are imposed to

avoid unrealistic estimates: $0 < a_n < 2\pi D_v L_v$ for $n = 1, 2...N$ where D_v and L_v are the diameter and lift (at the valve's curtain area) respectively. Linear inequality constraints are also imposed to ensure that consecutive a_n's do not vary unreasonably: $|a_{n+1} - a_n| < f a_n$ where δp_{n+1} and δp_n have the same sign and f is chosen to be 0.05. The relative change of a_n at the point where δp changes sign is not restricted (as long as a_n's fall within the upper and lower bounds) to allow a discontinuity in the effective area between forward and reverse flows.

The described quadratic program can be used to fit the effective area A_e using both fast sampled or averaged ΔP signals. Averaging the experimentally obtained ΔP signal to fit A_e we obtain the LP-EGR estimation error ϵ shown in Fig. (3.8(a)). A $\overline{\Delta P}$ lower bound as high as 12.7 kPa is required to keep ϵ within $\pm 1\%$. Fig. (3.8(b)) shows the resulting EGR estimation error ϵ if instead the ΔP signal sampled at 10 kHz is used. The LP-EGR $\overline{\Delta P}$ lower bound required to keep ϵ within $\pm 1\%$ is significantly reduced to 1.9 kPa.

A similar quadratic program can be used to fit the effective area using the unsteady orifice equation approximations (I) and (II) if the ΔP signals in these cases are filtered before being substituted in the function $\Psi^*(\Delta P)$. In the case of approximation (I), the cut-off frequency f_c for the 1$^{\text{st}}$ filter was varied from 50 Hz to 2 kHz, and for each f_c value, the ΔP signal was filtered and the quadratic program was solved. A filter bandwidth f_c greater than 875 Hz is found to result in the smallest LP-EGR $\overline{\Delta P}$ lower bound of 1.9 kPa (Fig. (3.8(c))). This $\overline{\Delta P}$ lower bound is the same one obtained using the quasi-steady orifice equation (with no filtering). Unlike the simulation results, no reduction in the $\overline{\Delta P}$ lower bound is observed when uniform ΔP filtering is applied to the experimental data.

For the unsteady orifice equation approximation (II), a variable filter bandwidth f_c is used. The variable bandwidth used for the simulation data has the form described in Eq. (3.5) where it is a function of K, A_e and $\sqrt{\overline{\Delta P}}$. Expressing f_c this way is convenient since both K and A_e are known in the simulation data. However, this is not the case for the experiment. Therefore C/KA_e is replaced by a lift-dependent coefficient $\widetilde{C}(L)/L$:

$$f_c = \frac{\widetilde{C}(L)}{L}\sqrt{\overline{|\Delta P|}} \tag{3.20}$$

The value of $\widetilde{C}(L)$ was varied from 50 to 400 (with ΔP in kPa and L in mm); an optimal $\widetilde{C}(L)$ of 300 reduces the LP-EGR $\overline{\Delta P}$ bound to 1.1 kPa (Fig. (3.8(d))) compared to 1.9 kPa using the quasi-steady orifice equation.

The same quadratic program can be also used to fit the effective area (A_e) for

the unsteady orifice equation approximation (III) with the introduction of a small modification. This can be derived from Eq. (3.8): an equivalent form to Eq. (3.7). Here it is convenient to rewrite Eq. (3.8) using the function $\Psi^*(\Delta P)$ instead of $\widetilde{\Psi}(\Delta P)$:

$$W \approx A_e(\Delta P)\Psi^*(\Delta P) \times \sqrt[\pm]{1 - \frac{KC_D^2 A_T^2 \widetilde{\Phi}(\Delta P)}{A_e^2(\Delta P)\Psi^*|\Psi^*|(\Delta P)} \frac{d}{dt}\left(A_e(\Delta P_f)\right)\Psi^*(\Delta P_f)} \tag{3.21}$$

Further approximating the $A_e(\Delta P)$ and $A_e(\Delta P_f)$ terms inside the signed square root by A_T where $A_T = \pi DL$:

$$W \approx A_e(\Delta P)\Psi^*(\Delta P) \times \sqrt[\pm]{1 - \frac{KC_D^2 A_T^2 \widetilde{\Phi}(\Delta P)}{A_T \Psi^*|\Psi^*|(\Delta P)} \frac{d}{dt}\Psi^*(\Delta P_f)} \tag{3.22}$$

The same quadratic program can be used to fit A_e for the unsteady orifice equation approximation (III) by replacing the function $\Psi^*(\Delta P)$ by the product of $\Psi^*(\Delta P)$ and the signed square root term in Eq. (3.22). A grid of $0 < KC_D^2 A_T^2 < 4.2 \times 10^{-}5$ and 100 Hz $< f_c <$ 300 Hz was used where the quadratic program was solved for each $KC_D^2 A_T^2$ and f_c combination. Assuming the use of uniform filtering, the optimal $KC_D^2 A_T^2$ was determined for each valve lift L and filter bandwidth f_c, and then an optimal f_c value (210 Hz) that minimizes the $\overline{\Delta P}$ lower bound for all 4 lifts was chosen. The optimal $KC_D^2 A_T^2$ values for 10, 30, 50 and 70% open EGR valve are 0, 5.6×10^{-6}, 6.3×10^{-6} and 6.3×10^{-6} (kg.s^{-1}) respectively; the optimal filter bandwidth is 210 Hz. The resulting $\overline{\Delta P}$ lower bound (Fig. (3.8(e))) required to keep the LP-EGR estimation error within $\pm1\%$ is 1.1 kPa (same as the unsteady orifice equation approximation (II)).

The same quadratic program used to fit A_e for the quasi-steady orifice equation can once again be extended to fit A_e for the unsteady orifice equation approximation (IV). It is convenient to write Eq. (3.9) as:

$$W \approx A_e(\Delta P)\Psi^*(\Delta P) - \frac{KC_D^2 A_T^2 \widetilde{\Phi}(\Delta P)}{2A_e(\Delta P)|\Psi^*|(\Delta P)} \frac{d}{dt} A_e(\Delta P)\Psi^*(\Delta P_f) \tag{3.23}$$

Formulation	LP-EGR $\overline{\Delta P}$ Lower Bound (kPa)	HP-EGR $\overline{\Delta P}$ Lower Bound (kPa)
Steady OE	12.7	27.9
Quasi-Steady OE	1.9	2.9
Unsteady Approx. (I)	1.9	2.9
Unsteady Approx. (II)	1.1	2.9
Unsteady Approx. (III)	1.1	2.9
Unsteady Approx. (IV)	1.3	2.9

Table 3.4: $\overline{\Delta P}$ lower bound for $|\epsilon| < 1\%$ using experimental data.

Further assuming $dA_e(\Delta P)/dt \approx 0$ gives:

$$W \approx A_e(\Delta P)\Psi^*(\Delta P) - \frac{KC_D^2 A_T^2 \widetilde{\Phi}(\Delta P)}{2|\Psi^*|(\Delta P)} \frac{d}{dt}\Psi^*(\Delta P_f) \tag{3.24}$$

The 1st term on the left hand side of Eq. (3.24) is identical to that in the quadratic program formulated to fit A_e for the quasi-steady orifice equation (and therefore is linear in a_n). The additional second term is specific to approximation (IV) but is linear in $KC_D^2 A_T^2$, and therefore, the formulated quadratic program can be used to solve for $KC_D^2 A_T^2$. The filter bandwidth f_c was varied from 25 to 400 Hz, and the extended quadratic program was solved for each f_c. An optimal f_c value of 245 Hz results in a $\overline{\Delta P}$ lower bound of 1.3 kPa (Fig. (3.8(f))) for the LP-EGR system.

Figure (3.9) shows the EGR estimation error using experimental data for the HP-EGR case. The $\overline{\Delta P}$ lower bound is significantly reduced with the use of a fast-sampled inlet and outlet pressures (p_i and p_o) compared to averaged p_i and p_o. However, unlike the LP-EGR case, no further reduction in $\overline{\Delta P}$ is observed with approximations (I) through (IV)[1]. This may be due the larger measurement error with the use of two absolute pressure sensors instead of a ΔP sensor. The computed ΔP signal ($p_i - p_o$) from the HP-EGR data shows ± 0.86 kPa noise, 4.8 times larger than the noise observed on the ΔP signal (± 0.18 kPa) from the LP-EGR data. Another possible factor is related to the accuracy of the reference EGR percentage computed based on the emissions bench measurement. In the HP-EGR setup, the intake is sampled for emissions at a short distance from the EGR introduction into the intake manifold. The CO_2 concentration in the emissions samples can be different from the average CO_2 concentration in the intake due to insufficient mixing. This

[1]The filtering is performed on the computed ΔP from the inlet and outlet absolute pressure sensors.

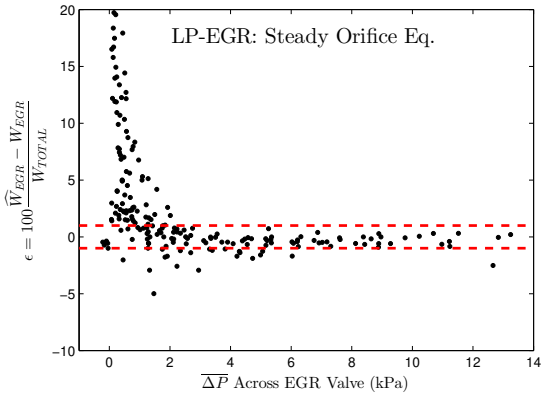

(a) LP-EGR: Steady OE

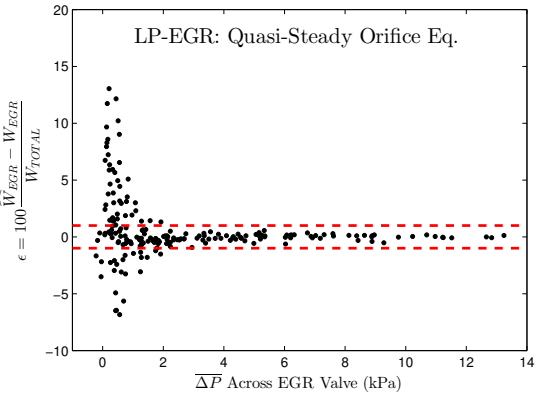

(b) LP-EGR: Quasi-Steady OE with ΔP sampled at 10 kHz

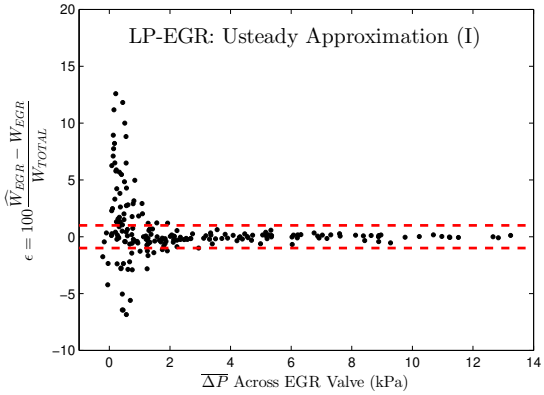

(c) LP-EGR: Unsteady OE Approx. (I) with ΔP sampled at 10 kHz

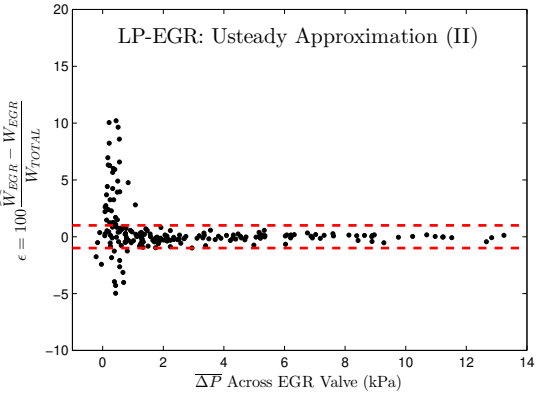

(d) LP-EGR: Unsteady OE Approx. (II) with ΔP sampled at 10 kHz

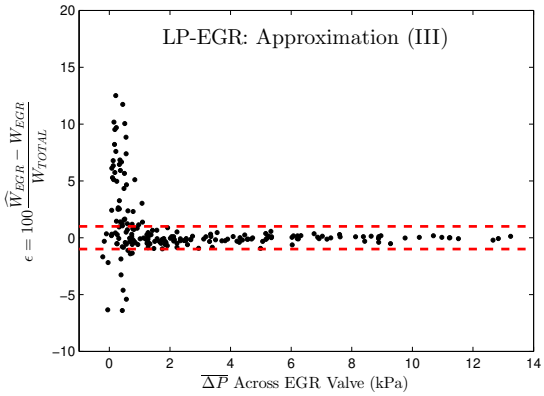

(e) LP-EGR: Unsteady OE Approx. (III) with ΔP sampled at 10 kHz

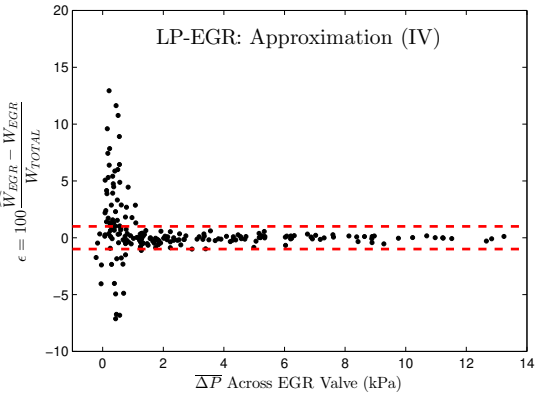

(f) LP-EGR: Unsteady OE Approx. (IV) with ΔP sampled at 10 kHz

Figure 3.8: LP-EGR estimation error for different formulations using experimental data. The $\overline{\Delta P}$ lower bound can be reduced 12.7 to 1.9 kPa with quasi-steady formulation; further reduction to 1.1-1.3 kPa is possible with unsteady approximations (II), (III) and (IV).

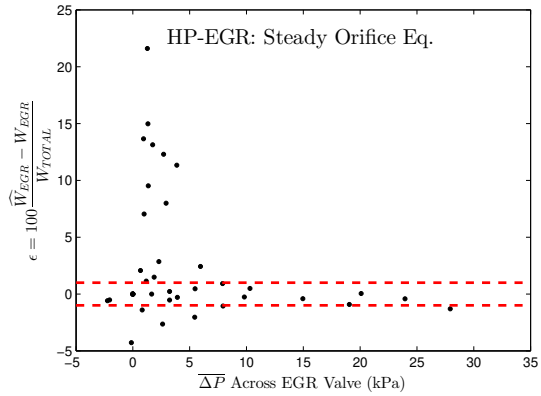

(a) HP-EGR: Steady OE

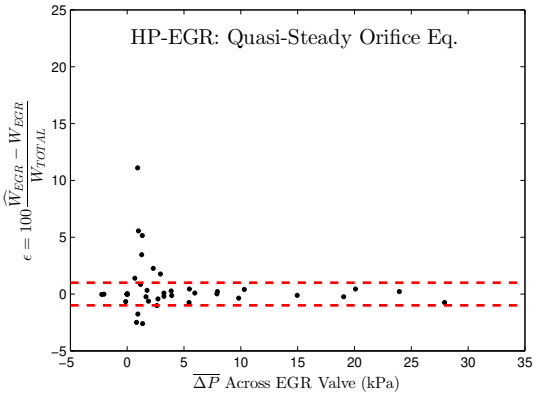

(b) HP-EGR: Quasi-Steady OE

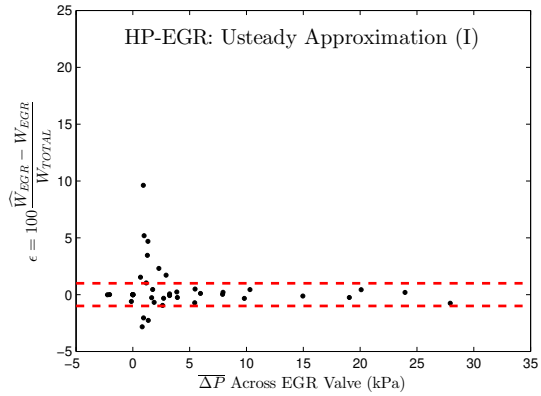

(c) HP-EGR: Unsteady OE Approx. (I)

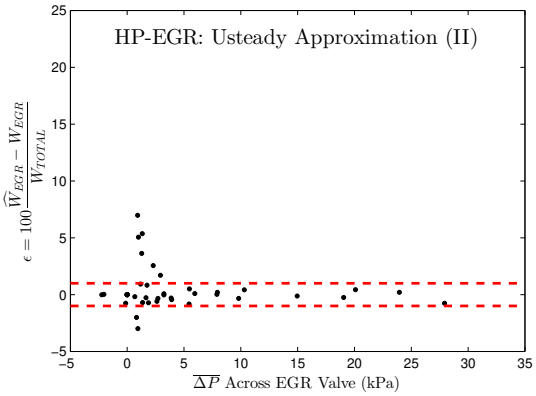

(d) HP-EGR: Unsteady OE Approx. (II)

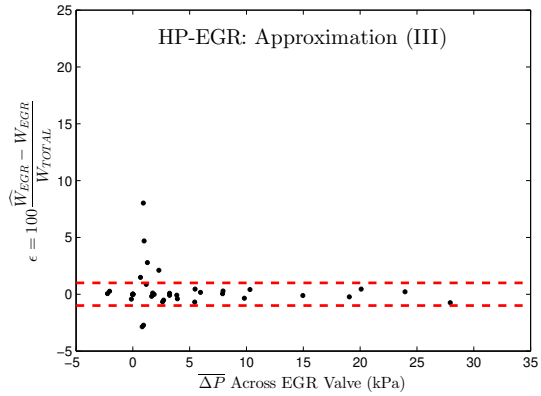

(e) HP-EGR: Unsteady OE Approx. (III)

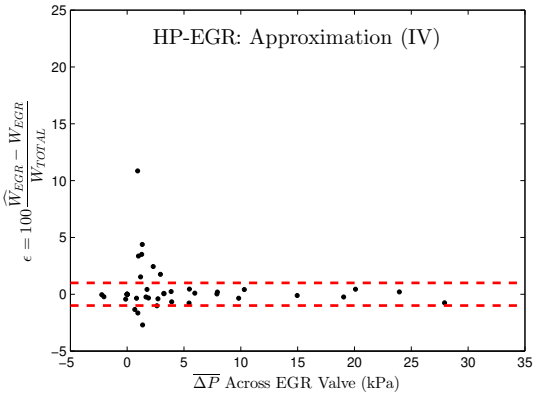

(f) HP-EGR: Unsteady OE Approx. (IV)

Figure 3.9: HP-EGR estimation error for different formulations using experimental data. The $\overline{\Delta P}$ lower bound can be reduced 27.9 to 2.9 kPa with quas-steady formulation; no further reduction is possible with the unsteady approximations.

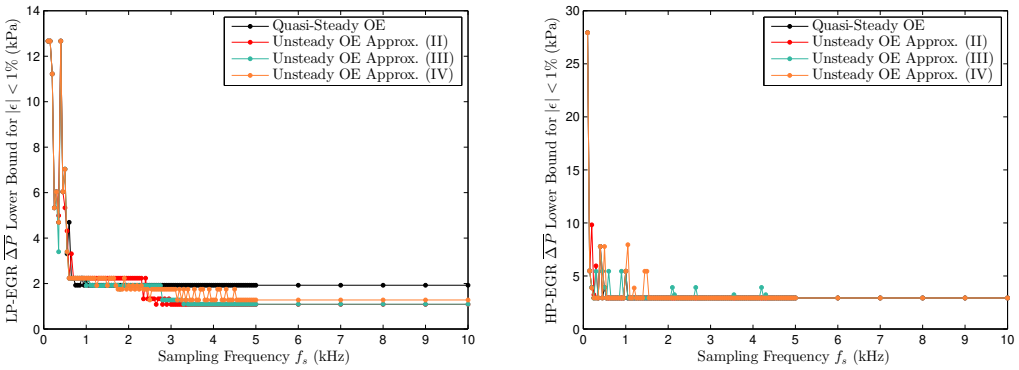

(a) LP-EGR: $\overline{\Delta P}$ vs f_s (b) HP-EGR: $\overline{\Delta P}$ vs f_s

Figure 3.10: $\overline{\Delta P}$ lower bound required to keep the EGR estimation error within $\pm 1\%$ as a function of ΔP sampling frequency from experimental data obtained using different orifice equation (OE) flow formulations.

problem is not encountered on a LP-EGR system as a result of the inherently longer paths between the EGR introduction into the intake system and the intake manifold. Table (3.4) summarizes $\overline{\Delta P}$ lower bound required to keep the EGR estimation error within $\pm 1\%$ for both LP and HP-EGR systems. While approximations (II) through (IV) can reduce the LP $\overline{\Delta P}$ lower bound compared to the quasi-steady formulation, none of the approximations was able to reduce the HP $\overline{\Delta P}$ lower bound.

Finally, the pressure sensor signals from the LP and HP-EGR data are down-sampled using sampling frequencies (f_s) ranging from 100 Hz to 10 kHz to determine the minimum sampling frequency requirement. Figure (3.10) shows the $\overline{\Delta P}$ lower bound plotted versus f_s for various flow formulations. The impact of sampling frequency on approximation (I) was not investigated as it does not provide any improvement over the quasi-steady orifice equation. For the LP-EGR case, a sampling frequency of 1.05 kHz was found sufficient with the quasi-steady orifice equation. A higher sampling frequency of 2.45 kHz was required to achieve most of the benefit of the unsteady orifice equation approximation (II); a sampling frequency of 3 kHz was required to achieve the full benefit. For the HP-EGR case, sampling frequencies of 0.55 and 1.05 kHz were found sufficient with the quasi-steady orifice equation and the unsteady orifice equation approximation (II). Table (3.5) summarizes the sampling frequency f_s requirement to achieve the full benefit for each flow formulation.

Formulation	LP-EGR Sampling Freq. Requirement (kHz)	HP-EGR Sampling Freq. Requirement (kHz)
Steady Orifice Eq.	≥ 1.05	≥ 0.55
Unsteady Approx. (II)	≥ 3.00	≥ 1.05
Unsteady Approx. (III)	≥ 3.30	≥ 4.35
Unsteady Approx. (IV)	≥ 4.60	≥ 1.55

Table 3.5: LP and HP-EGR sampling frequency requirement from experimental data.

3.5 Summary and Conclusions

This chapter addressed the practical aspects of implementing the lessons learned in Chapter II on an EGR system. First the optimal sensor configuration was determined using GT-Power simulations. The individual contributions of the pressure and temperature signals to the EGR estimation non-linearity error were evaluated. While averaging the EGR valve inlet and outlet temperatures has a negligible effect, either two fast-sampled valve inlet and outlet pressure sensors or a single fast-sampled ΔP sensor were required to avoid the non-linearity. Modeled measurement errors also showed that the use of a ΔP sensor results in lower EGR estimation errors. Both the need for fewer fast-sampled measurements and lower impact of measurement errors favor a ΔP sensor (along with an averaged outlet pressure sensor) over two absolute pressure sensors.

Approximations of the unsteady orifice equation using filtered ΔP signals and the quasi-steady formulations were proposed and evaluated using both simulation and experimental data. These approximations avoid the need to solve a non-linear 1^{st} order system to estimate the EGR flow. Uniform and variable bandwidth low-pass filters were considered. The variable filter was shown analytically to be dependent on the EGR valve area and ΔP. While the second approximation with variable filtering successfully reduced the $\overline{\Delta P}$ lower bound required to keep the LP-EGR estimation error within the target $\pm 1\%$ from 1.9 (no filtering) to 1.1 kPa, no improvement was observed for the HP-EGR case. This can be due to the larger errors in the computed ΔP due to the use of two absolute pressure sensors.

Finally, the sampling frequency requirement wa determined for the LP and HP-EGR systems by down-sampling the measured pressures at different rates in post-processing. A minimum sampling frequency of ≈ 1 kHz was required to avoid the non-linearity error reducing the LP and HP $\overline{\Delta P}$ lower bound from 12.7 and 27.9 kPa to 1.9 and 2.9 kPa respectively. A higher sampling rate of ≈ 3 kHz was required to

achieve the full benefit of the unsteady orifice approximation with variable filtering and reduce the LP $\overline{\Delta P}$ lower bound from 1.9 to 1.1 kPa.

The experiments and simulations presented in this chapter include the major error sources present: non-linearity, inertial and measurements errors. However, pressure gauge-lines were kept as short as possible to avoid distortions of the measured pressure signal, and the EGR valves used are new which eliminates effective area errors due to the accumulation of carbon deposits. Gauge-line and effective area errors are the subject of the following two chapters.

CHAPTER IV

Impact of and Correction for Gauge-Lines Distortions

Pressure sensing lead lines, or gauge-lines, are part of ΔP measurement systems. These gauge-lines are necessary to protect the ΔP sensor from excessive temperatures, or due to space constraints and packaging restrictions. Unfortunately, acoustic resonance is excited within the lines under pulsating conditions. The characteristics of the excitation depends on the pulsation frequency and line lengths. This can either amplify or attenuate the pulsations. The pressure differential at the ΔP sensor is therefore distorted and different from the actual pressure differential at the valve taps, which can in some cases lead to significant EGR mass flow rate calculation errors, also known as gauge-line errors [28].

In this chapter, the impact of gauge-lines on the EGR estimation error is quantified using 1-D simulations. Methods to correct for the gauge-line distortion are proposed and evaluated under ideal and more realistic noisy measurement conditions.

4.1 Pressure Gauge-Line Model

The effects of the ΔP sensor gauge-line lengths on EGR estimation error were quantified for LP-EGR configuration. A separate GT-Power model was used where the gauge-lines are modeled as straight round tubes with lengths varying from $L = 10$ to 30 cm. The pressure amplification and attenuation in the gauge-lines were simulated in isolation from the engine fast running 1-D model. The small discretization lengths used for gauge-line tubes require a small simulation time step that makes the combined engine and gauge-lines system simulations computationally expensive. The EGR valve inlet pressures and temperatures at the gauge line tap were obtained from the LP-EGR engine simulations and imposed as time-varying

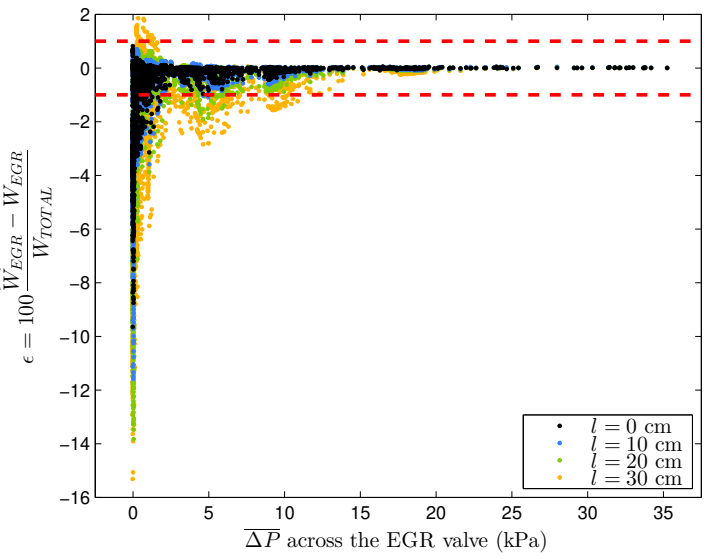

Figure 4.1: LP-EGR estimation error using the quasi-steady compressible orifice equation for different gauge-line lengths.

boundary conditions at one end of the tube at the EGR valve inlet. A similar step was performed for the open end of the tube at the EGR valve outlet using the valve outlet pressures and temperatures. The other end of both tubes was treated as closed to model the gauge-line termination at the ΔP sensor ports. Grid sensitivity analysis on the gauge-lines 1-D model was performed to ensure that the pressures at the both sensor ports were insensitive to spacial discretization. Starting with a discretization length of 25 mm, several iterations were performed where the discretization length of the round tubes was halved following each iteration until the estimated pressure traces converge. The estimates of the pressure traces at the end caps (sensor ports) were considered to converge when the root-mean-square (RMS) of the difference between the traces from consecutive iterations is less than 0.05 kPa. A final discretization length of ≈3 mm is used to ensure grid independence.

The simulated pressure traces at the sensor ports for gauge-line lengths of 10, 20 and 30 cm were then used in the quasi-steady orifice equation (Eq. 2.31), and the LP-EGR estimation errors ϵ were computed and compared to the error obtained for the baseline case with no gauge-lines ($L = 0$ cm). Figure (4.1) shows this error versus $\overline{\Delta P}$ for different gauge-line lengths. The lower bound of 1.4 kPa on $\overline{\Delta P}$, required to keep ϵ within $\pm 1\%$ when ΔP is read directly at the tap ($L = 0$ cm) slightly increases to 1.7 kPa when 10 cm gauge-lines are introduced at the EGR valve inlet and outlet ($L = 10$ cm). The EGR estimation accuracy deteriorates however as longer gauge-line

are used ($L = 20, 30$ cm). Higher $\overline{\Delta P}$ lower bounds of 5.9 and 10.9 kPa are required to maintain the same EGR estimation accuracy when 20 and 30 cm (respectively) gauge-lines are used.

4.2 Correcting for Gauge-Line Errors

A lumped parameter model was developed by Nagao and Ikegami [43] in order to model the amplification and attenuation of the pressure signal through the gauge-lines. The model relates the pressure at the sensor port (p_s) to the pressure at the gauge-line tap (p_t) through the 2$^{\text{nd}}$ order non-linear differential equation:

$$\alpha \frac{d^2 p_s}{dt^2} + \beta \frac{dp_s}{dt} \left| \frac{dp_s}{dt} \right| + p_s = p_t \tag{4.1}$$

where α is a function of geometry and speed of sound, and β is a function of geometry, speed of sound, friction and the average pressure at the tap. The non-linear term in Eq. 4.1, $dp_s/dt\,|dp_s/dt|$ is representative of non-linear friction losses [43]. Botros et. al investigated the accuracy of this model (Eq. 4.1), and reported that it can be applied to moderate gauge-line lengths ($\lesssim 1.3$ m) with its accuracy slightly decreasing with increased pulsation frequency and amplitude [52].

With the lumped parameter model (Eq. 4.1) correctly tuned, and the pressure measurement p_s, the actual pressure signal at the tap p_t can be estimated. But in the case of a ΔP measurement, only the measurement of the difference of the inlet and outlet pressure signals at the sensor ports is available; thus, Eq. 4.1 does not apply. The pressure pulsations downstream of the EGR valve (pre-compressor) are small compared to those upstream of it (post-turbine), so the pressure pulsations downstream of the EGR valve can be neglected. It follows that $dp_s/dt \simeq 0$ and $d^2p_s/dt^2 \simeq 0$ at the downstream side. Hence we can write $p_{s,d} \simeq p_{t,d}$ where $p_{s,d}$ and $p_{t,d}$ are the respective pressures at the sensor and the tap downstream the EGR valve. Expressing Eq. 4.1 for the pressures at the sensor and the tap upstream of the EGR valve, $p_{s,u}$ and $p_{t,u}$, and subtracting $p_{s,d}$ and $p_{t,d}$ from the left hand and right hand sides respectively, gives:

$$\alpha \frac{d^2 \Delta p_s}{dt^2} + \beta \frac{d\Delta p_s}{dt} \left| \frac{d\Delta p_s}{dt} \right| + \Delta p_s = \Delta p_t \tag{4.2}$$

where $\Delta p_s = p_{s,u} - p_{s,d}$ and $\Delta p_t = p_{t,u} - p_{t,d}$. For each of the simulated cases in the 1-D model, the least sum of square error (LSSE) estimates of α and β are determined

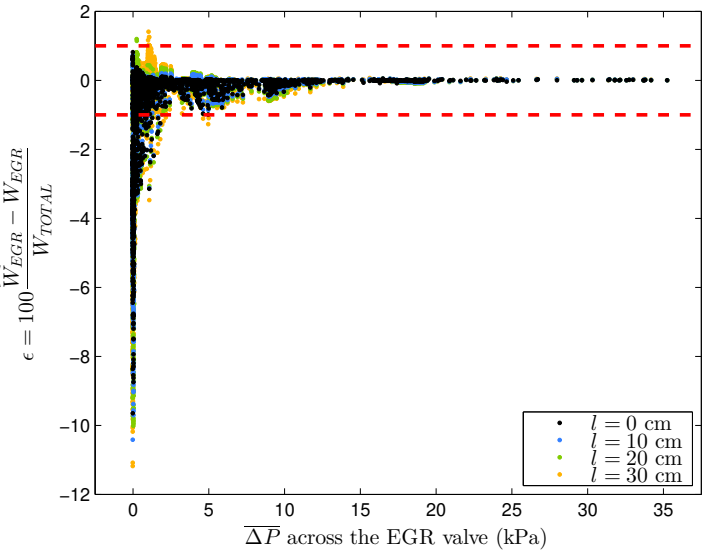

Figure 4.2: LP-EGR estimation error using the quasi-steady compressible orifice equation with compensation for the gauge-line effects using Eq. 4.2.

where the error is defined as the difference between the right and left hand sides of Eq. 4.2. The values of α and β for a given gauge-line length L, are then set to the average of their corresponding LSSE estimates obtained from all operating conditions with the same gauge-line length, and Eq. 4.2 is used to estimate the actual ΔP at the taps from the distorted ΔP signal seen at the sensor ports. The corrected ΔP signals are then used in the steady orifice equation (Eq. 2.31), and the corresponding error in the estimated EGR percentage ϵ is shown in Fig. 4.2. The EGR estimation accuracy is improved; the lower bound on $\overline{\Delta P}$ required to keep ϵ within $\pm 1\%$ is reduced to 1.4, 1.4 and 1.9 kPa for the cases with 10, 20 and 30 cm gauge-lines respectively. The $\overline{\Delta P}$ lower bound remains at 1.4 kPa for 0 cm gauge-line case.

Alternatively, the distortions of the pressure signal due to gauge-line lengths could have been corrected without the need to assume negligible pressure pulsations downstream of the EGR valve if instead a linearized version of Eq. 4.1 was used. Assuming a lumped parameter model based on a linearized friction model gives:

$$\alpha \frac{d^2 p_s}{dt^2} + \widetilde{\beta} \frac{dp_s}{dt} + p_s = p_t. \tag{4.3}$$

Further assuming the same gauge-line lengths upstream and downstream of the valve, and neglecting the difference in the upstream and downstream acoustic velocity resulting from the temperature difference across the valve, it follows that the upstream

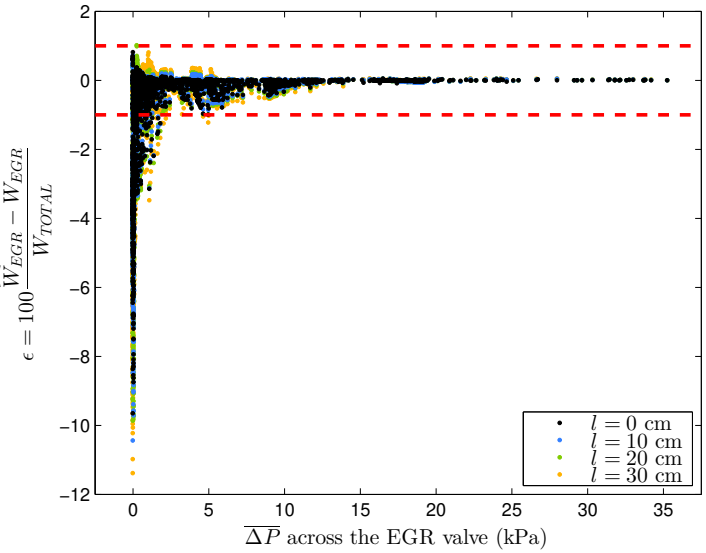

Figure 4.3: LP-EGR estimation error using the quasi-steady compressible orifice equation with compensation for the gauge-line effects using Eq. 4.4.

and downstream α and $\widetilde{\beta}$ are equal, and therefore:

$$\alpha\frac{d^2\Delta p_s}{dt^2} + \widetilde{\beta}\frac{d\Delta p_s}{dt} + \Delta p_s = \Delta p_t. \tag{4.4}$$

Using Eq. 4.4 to correct for the gauge-line effects results in a reduction similar to that of Eq. 4.2 in the lower bound in $\overline{\Delta P}$ required to keep ϵ within $\pm 1\%$ as shown in Fig. 4.3. Table (4.1) summarizes $\overline{\Delta P}$ lower for different gauge-line lengths and compensation methods. Equation 4.4 is used for the remaining analysis in this chapter.

Gauge-Line Length (cm)	$\overline{\Delta P}$ Lower Bound (kPa)		
	No Correction	Corr. using Eq. 4.2	Corr. using Eq. 4.4
0	1.4	1.4	1.4
10	1.7	1.4	1.4
20	5.9	1.4	1.4
30	10.9	2.2	2.2

Table 4.1: $\overline{\Delta P}$ lower bound for different gauge-line lengths and compensation methods.

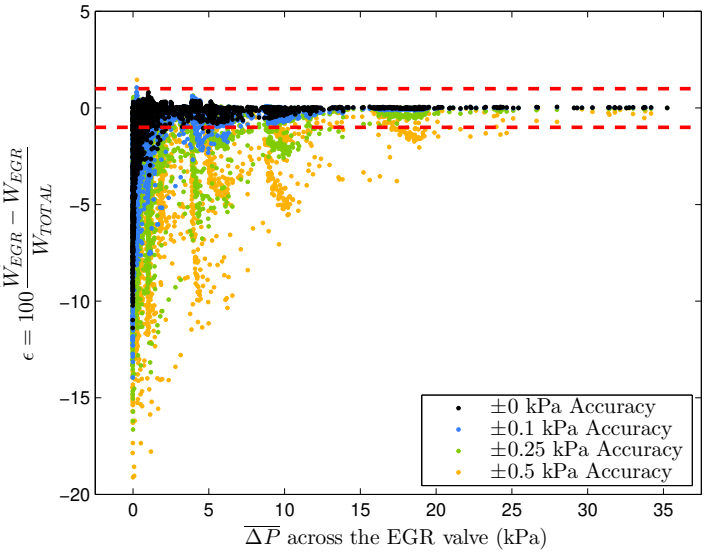

Figure 4.4: LP-EGR estimation error using the quasi-steady compressible orifice equation for 30 cm gauge-lines and different ΔP measurement accuracies. Gauge-line distortions in the noisy ΔP signal are corrected for using the model in Eq. 4.4.

4.3 Measurement Noise Effects on EGR Estimation Errors

Although the correction methods for gauge-line length effects proposed in the previous section produce satisfactory results, they both involve the differentiation of the measured ΔP signal. This can be problematic in the presence of high-frequency noise components that are amplified when differentiated. Therefore, in this section, the ΔP sensor measurement noise error is modeled as white noise superimposed onto the sensor ΔP signals. This allows investigating the feasibility of correcting for gauge-line effects under realistic scenarios with measurement noise during the process of estimating EGR mass flow.

Figure 4.4 depicts the error in the estimated EGR percentage ϵ versus $\overline{\Delta P}$ using the quasi-steady compressible orifice equation fed with corrected and noisy ΔP signals with 30 cm gauge-line lengths. As expected, the EGR estimation accuracy is significantly deteriorated. Even a small ΔP measurement error of ± 0.1 kPa[1] requires the lower bound on $\overline{\Delta P}$ to be increased from 2.2 to 6.2 kPa to keep ϵ within $\pm 1\%$. Larger measurement errors of ± 0.25 and ± 0.5 kPa result in further $\overline{\Delta P}$ increases to 13.8 and 24.7 kPa respectively.

[1]The ± 0.1 kPa corresponds to 95% confidence interval; the measurement error is randomly sampled from $\mathcal{N}\left(0, \sigma^2\right)$ where $\sigma = 0.1/2$.

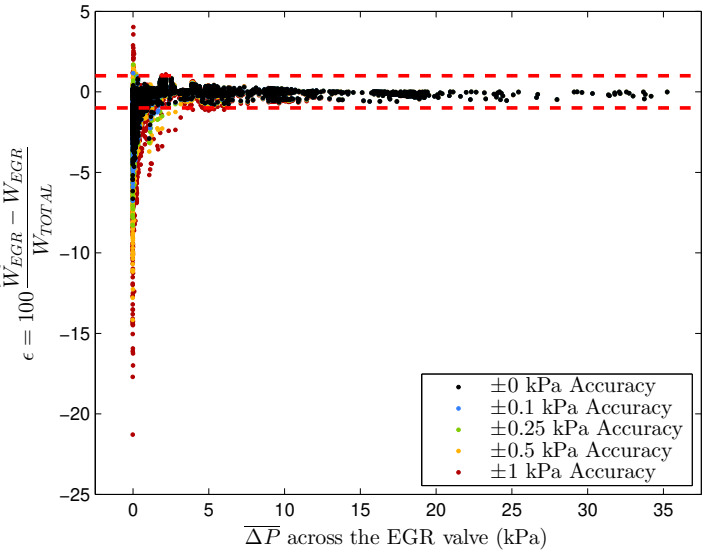

Figure 4.5: LP-EGR estimation error using the quasi-steady compressible orifice equation for 30 cm gauge-lines and different ΔP measurement accuracies. The ΔP signal is low-pass filtered (cut-off frequency $f_C = 205$ Hz), then gauge-line effects are corrected for using the model in Eq. 4.4.

Since the high frequency components of the measurement error are significantly amplified after differentiating the ΔP signal, low-pass filtering of the noisy ΔP signal was considered before using the proposed correction method for the gauge-line effects. Specifically, a 1st order low pass filter with a cut-off frequency f_c of 205 Hz was used. This particular frequency was chosen based on the results from Chapter III where this f_c mimics the EGR flow lag due to inertial effects. Figure 4.5 shows the corresponding error in estimated LP-EGR percentage ϵ versus $\overline{\Delta P}$. The lower bound on $\overline{\Delta P}$ required to keep ϵ within $\pm 1\%$ is reduced from 6.2, 13.8 and 24.72 kPa without filtering to 1.2, 1.4 and 1.7 kPa with filtering for measurement errors of ± 0.1, ± 0.25 and ± 0.5

ΔP Sensor Accuracy (kPa)	$\overline{\Delta P}$ Lower Bound (kPa)	
	Correction without Filtering	Correction with Filtering
0	2.2	0.9
± 0.1	6.2	1.2
± 0.25	13.8	1.4
± 0.5	24.7	1.7
± 1.0	–	2.3

Table 4.2: $\overline{\Delta P}$ lower for 30 cm gauge-line length with modeled ΔP measurement noise.

respectively. The lower bound required for a measurement error of ±1 kPa is 5.3 kPa (with filtering). Table (4.2) summarizes $\overline{\Delta P}$ lower for 30 cm gauge-line length with modeled ΔP measurement noise.

4.4 Summary and Conclusions

This chapter studied the impact of pressure gauge-lines on the EGR estimation error using GT-Power simulations. A method to correct for the gauge-line distortions based on a 2^{nd} order lumped parameter was proposed and evaluated. Gauge-lines longer than $\approx$ 10 cm were found to considerably increase the LP-EGR estimation error; 30 cm gauge-lines increased the $\overline{\Delta P}$ lower bound required to keep the LP-EGR estimation error within ±1% from 1.4 to 10.9 kPa using the quasi-steady orifice equation. The proposed correction method can reduce the $\overline{\Delta P}$ lower bound back to 1.4 kPa in the presence of ±0.25 kPa measurement noise. With higher noise magnitudes of ±0.5 and ±1 kPa, the $\overline{\Delta P}$ lower bound can be only reduced to 1.7 and 2.3 kPa respectively.

CHAPTER V

Impact of and Correction for Valve Area Errors

In the previous chapters, various error sources contributing to the EGR estimation error were investigated: non-linearity errors, inertial errors, measurement errors, and gauge-line distortion errors. All these errors had the largest impact at low ΔP, effectively requiring a lower bound on $\overline{\Delta P}$ to keep the EGR estimation error (ϵ) within the target $\pm 1\%$. Effective area errors affect the EGR estimation accuracy differently.

In the case of ΔP measurement across the EGR valve, such errors can result from measurement errors in the valve lift sensor, or from actual changes in the area due to carbon deposits. The resulting errors in the ECU's estimate of the effective area are more problematic at low valve lift operation. For example, an area offset error of 0.02 mm at full valve lift of 6 mm accounts for a small relative error of 0.33%. The same area offset corresponds to 4% relative error at 0.5 mm valve lift leading to 4% relative error in EGR flow, and therefore, an EGR estimation error of 1% at 25% EGR. Since for the same target EGR flow, a smaller valve opening is needed at larger ΔP's, valve area errors - unlike the errors discussed in the previous chapters - can be especially detrimental to the EGR estimation accuracy at the large ΔP's.

In this chapter, the impact of effective area errors are quantified using 1-D engine simulations. The use of a lower bound on valve lift to avoid problematic low lift operations is evaluated. Finally, a novel method for online calibration of the HP-EGR valve area using preexisting engine sensors is proposed.

5.1 Impact of Effective Area Errors

Over the life of a valve, carbon deposits gradually accumulate changing the valve area over time. While some valve actuation algorithms attempt to remove the carbon deposits by slamming the valve shut to crush any deposits, this method can only

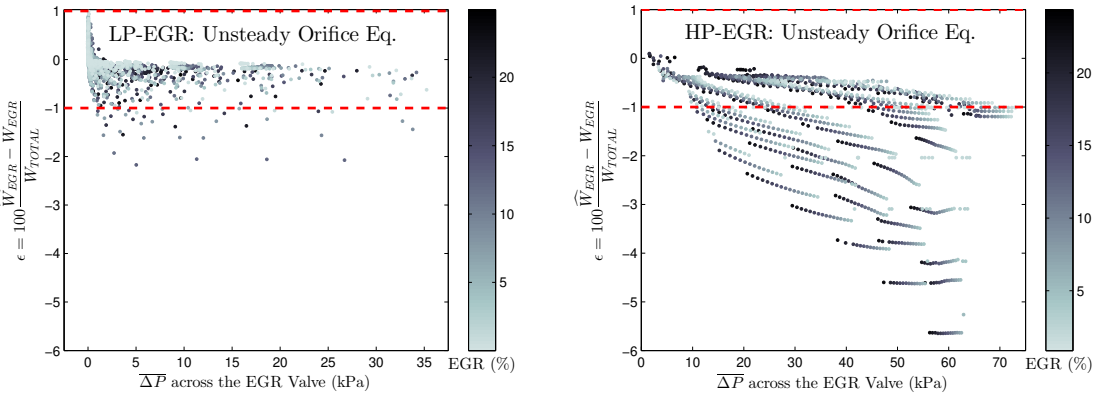

(a) LP-EGR: Unsteady Orifice Eq.

(b) HP-EGR: Unsteady Orifice Eq.

Figure 5.1: EGR estimation error for the compressible flow unsteady orifice equation with 0.02 mm valve lift offset error.

remove the deposits on the valve seat. The change in the effective area is not fully eliminated. To model the impact of carbon deposits, an area offset error was used to approximate their effect on the EGR valve effective area (A_e). The valve lift value used to compute A_e in the unsteady orifice equation (Eq. (2.35)) was varied by 0.02 mm from the lift value used in the LP and HP-EGR GT-Power simulations.

Figure (5.1) shows the EGR estimation error using the unsteady orifice equation with 0.02 mm offset error in valve lift. Even a small offset error of 0.02 mm can cause EGR estimation errors that exceed the target $\pm 1\%$. As expected, the deterioration of the EGR estimation accuracy is more severe at the larger $\overline{\Delta P}$ due to the low-lift valve operation.

5.2 Valve Lift Lower Bound

Given that area offset errors are mostly problematic at the low valve lifts, the feasibility of imposing a lower bound on EGR valve lift was investigated. To analytically derive an equation for the lift lower bound, the actual flow is approximated using the steady incompressible orifice equation:

$$W_{EGR} = A_e \sqrt{2\rho\Delta P} \tag{5.1}$$

while the estimated flow where the only error source present is an area offset error is written as:

$$\widehat{W}_{EGR} = \widehat{A_e}\sqrt{2\rho\Delta P} = (A_e + A_{e,\text{OFFSET}})\sqrt{2\rho\Delta P} \tag{5.2}$$

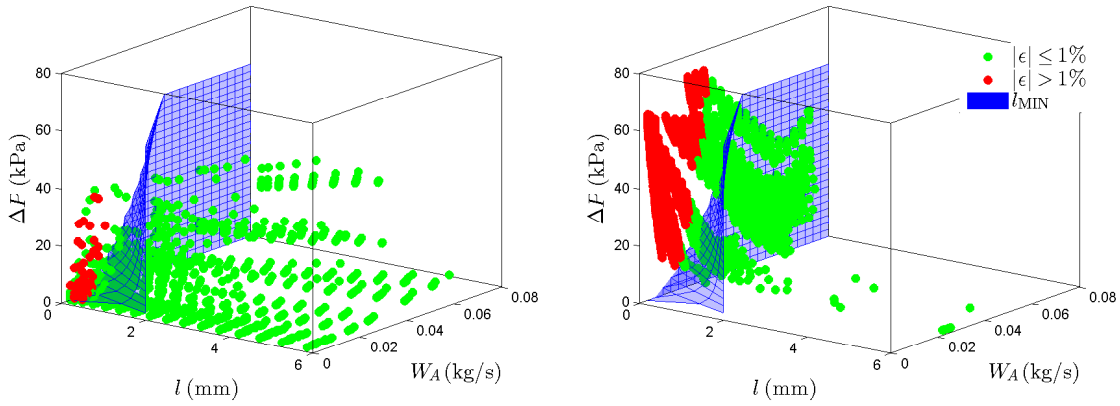

(a) LP-EGR: Unsteady Orifice Eq. (b) HP-EGR: Unsteady Orifice Eq.

Figure 5.2: Lower Bound on EGR valve lift for EGR estimation error within ±1% with a 0.02 mm lift offset error. Green and red circles correspond to the simulated points with an EGR estimation error less than and greater that 1% respectively.

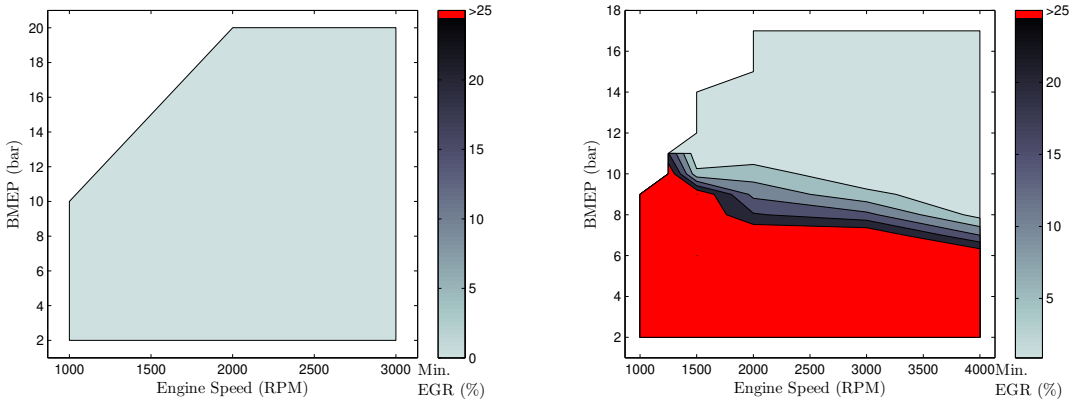

(a) LP-EGR: Unsteady Orifice Eq. (b) HP-EGR: Unsteady Orifice Eq.

Figure 5.3: Minimum permissible EGR percentage for the imposed lower bound on EGR valve lift corresponding to a 0.02 mm lift offset error. HP-EGR is not possible at low and mid loads.

The EGR estimation error (ϵ) can now be written as:

$$\epsilon = 100\frac{\widehat{W}_{EGR} - W_{EGR}}{W_{TOTAL}} = 100\frac{\widehat{W}_{EGR} - W_{EGR}}{W_{EGR} + W_A} = 100\frac{A_{e,\text{OFFSET}}\sqrt{2\rho\Delta P}}{A_e\sqrt{2\rho\Delta P} + W_A} \tag{5.3}$$

where W_A is the engine air flow. Approximating the effective area using $A_e \approx \pi Dl$, where D and l are the EGR valve diameter and lift respectively, gives:

$$\epsilon = 100\frac{\pi D l_{\text{OFFSET}}\sqrt{2\rho\Delta P}}{\pi Dl\sqrt{2\rho\Delta P} + W_A} \tag{5.4}$$

Solving for the valve lift l under the constraint $\epsilon \geq 1$ gives:

$$l \geq l_{\text{MIN}} = 100 l_{\text{OFFSET}} - \frac{W_A}{\pi D\sqrt{2\rho\Delta P}} \tag{5.5}$$

The derived lift lower bound is an increasing function in the lift offset error (l_{OFFSET}). A larger lift offset error requires valve operation at larger lifts such that the offset error is *relatively* small. The lift lower bound is also an increasing function in $\sqrt{\Delta P}/W_A$. This term is approximately proportional to the EGR fraction. At larger EGR fractions, the same relative error in the EGR flow results in larger EGR estimation error.

Figure (5.2) shows the lower bound on EGR valve lift from Eq. (5.5) required to keep the EGR estimation within $\pm 1\%$ for both LP and HP-EGR systems. Simulated points with an EGR estimation error less than and greater that 1% are shown as solid green and red circles respectively. The derived lower bound on valve lift is somewhat conservative, but is successful to avoid the point where a lift offset error of 0.02 mm leads to EGR estimation errors greater than 1%. However, imposing a minimum valve lift while flowing EGR implies a minimum EGR percentage below which the engine cannot operate. If this minimum EGR percentage is higher than the engine tolerance for EGR, then EGR cannot be used at the given operating condition. Figure (5.3) shows the contours of the minimum permissible EGR percentage for the imposed lower bound on EGR valve lift corresponding to a 0.02 mm lift offset error. The lift lower bound is barely restrictive for the LP-EGR case. However, the minimum permissible HP-EGR percentage exceeds 25% at the low to mid engine loads, and as result, no EGR can be flowed. The lower $\overline{\Delta P}$'s observed on the LP-EGR system force the LP-EGR valve operation at higher valve lifts. As a result, lift offset errors are not as detrimental as the HP-EGR case. The use of a smaller HP-EGR valve diameter can be considered to reduce the impact of lift offset errors.

5.3 EGR Valve Area Online Calibration

Since imposing a lower bound on the HP-EGR valve lift even for small lift offset errors of 0.02 mm prevents HP-EGR operation at low to mid-engine loads, a better solution is required. An online adaption of the EGR valve area can be performed if an independent (feedback) EGR measurement is available. This can be obtained from an intake air oxygen (IAO2) sensor. Unfortunately, adding an IAO2 sensor imposes additional costs, and the IAO2 EGR estimate can be subject to errors due to insufficient mixing and fuel present in the intake manifold. A better solution would be to have an online area calibration method based on preexisting engine sensors.

A HP-EGR valve connects the exhaust and intake manifolds, so pressure coupling between the two manifolds is a function of the actual valve area. The use of an existing intake manifold pressure sensor to calibrate the HP-EGR valve area can be possible if a transfer function relating intake pressure to the valve area can be established and the sensitivity of the intake pressure to the valve area is sufficiently large.

Steady-state intake manifold pressure is achieved when input flows into the intake manifold from the throttle body (W_θ) and HP-EGR valve (W_{VLV}) balance out with the output flows into the engine cylinders (W_{ICE}):

$$W_\theta + W_{VLV} = W_{ICE} \tag{5.6}$$

The throttle flow can be modeled using the steady orifice equation:

$$W_\theta = A_\theta \Psi^*(p_{PT}, p_{INT}) \tag{5.7}$$

where A_θ is the throttle area, p_{PT} is the pre-throttle pressure and p_{INT} is the intake manifold pressure. Similarly, the HP-EGR valve flow can be written as:

$$W_{VLV} = A_e \Psi^*(p_{EXH}, p_{INT}) \tag{5.8}$$

where A_e is the EGR valve effective area and p_{EXH} is the exhaust manifold pressure (neglecting the pressure drop in the HP-EGR cooler). The engine flow at a given engine speed (N) can be approximated by a linear function in intake pressure:

$$W_{ICE} \approx \alpha_0(N) + \alpha_1(N) p_{INT} \tag{5.9}$$

Substituting Eq. (5.7), (5.8) and (5.9) into Eq. (5.6) gives:

$$A_\theta \Psi^*(p_{PT}, p_{INT}) + A_e \Psi^*(p_{EXH}, p_{INT}) = \alpha_0(N) + \alpha_1(N) p_{INT} \tag{5.10}$$

Equation (5.10) shows that the maximum sensitivity of the intake pressure p_{INT} to the changes in the HP-EGR valve area (A_e) occurs when the $\Psi^*(p_{EXH}, p_{INT})$ is the largest. This is obtained at sufficiently small intake manifold pressures such that the flow through the HP-EGR valve is choked: $p_{INT}/p_{EXH} \leq P_{r,CR}$ ($P_{r,CR}$ is the critical pressure ratio). At choked conditions, the HP-EGR valve flow is maximized for a given valve area (A_e) and upstream pressure (p_{EXH}) which maximizes the sensitivity of p_{INT} to A_e. However, maximizing the HP-EGR flow can be undesirable to avoid combustion instabilities from excessive EGR flow. Fortunately, this can be avoided if this online calibration procedure is performed under deceleration fuel shut-off (DFSO) conditions. In this case, the HP-EGR valve flow is just another source of air flow into the intake manifold. Under DFSO conditions, the pre-throttle and exhaust manifold pressures are roughly atmospheric ($p_{PT} = p_{EXH} = p_0$) which gives:

$$(A_\theta + A_e)\, \Psi^*(p_0, p_{INT}) = \alpha_0(N) + \alpha_1(N) p_{INT} \tag{5.11}$$

Under choked conditions, the term $\Psi^*(p_0, p_{INT})$ is not a function of p_{INT} resulting in a linear relation between p_{INT} and A_e:

$$(A_\theta + A_e)\, \Psi^*(p_0, p_0 P_{r,CR}) = \alpha_0(N) + \alpha_1(N) p_{INT} \tag{5.12}$$

While Eq. (5.10) and (5.12) show an encouraging relation between the intake manifold pressure (p_{INT}) and the HP-EGR valve effective area (A_e), the sensitivity of p_{INT} to changes in A_e has to be quantified.

5.3.1 GT-Power Simulations

The same GT-Power engine model with HP-EGR described in Section 2.1.2 was used evaluate the proposed EGR valve area online calibration method. Injected fuel mass flow rate was set to zero, and the intake throttle angle was fixed at the value resulting in a 0.3 bar intake pressure (choked condition) at 2000 RPM with the HP-EGR valve fully closed. Engine speeds of 1000 through 2000 RPM (at increments of 250 RPM) were considered. At each engine speed, the HP-EGR valve lift was swept from fully closed to fully open. At each valve lift, the model was run until steady-state conditions were met. Figure (5.4) shows the simulated transfer functions relating the

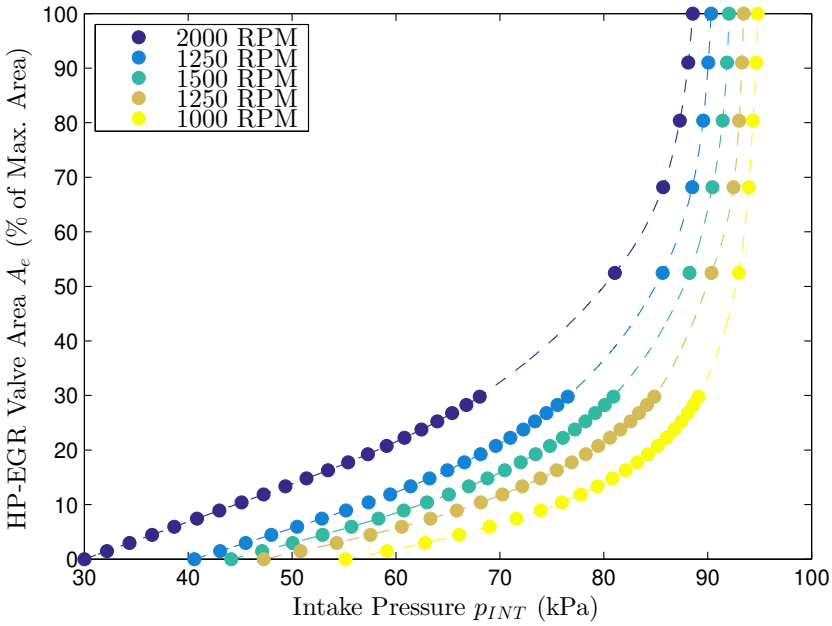

Figure 5.4: Simulated transfer functions for HP-EGR valve area calibration at different engine speeds.

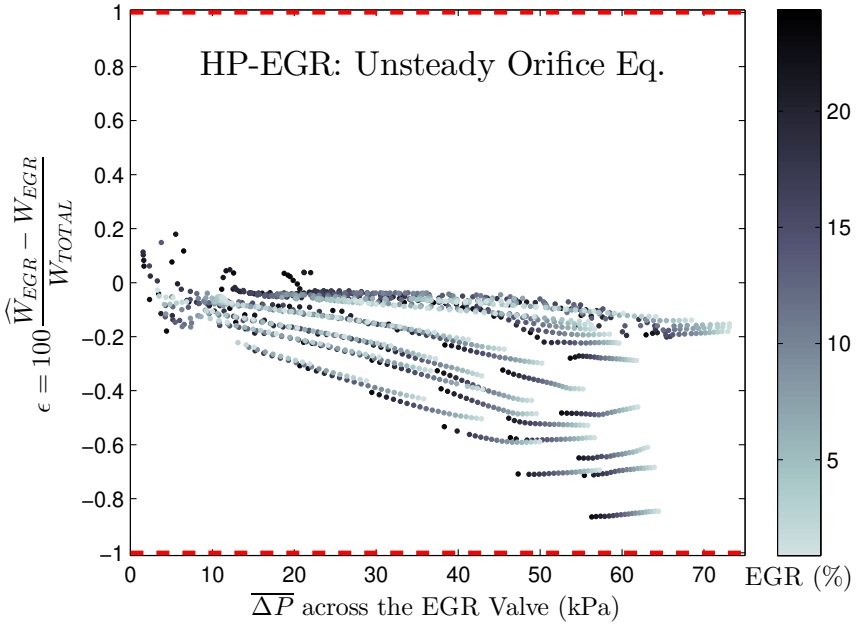

Figure 5.5: HP-EGR estimation error for the compressible flow unsteady orifice equation with 0.003 mm valve lift offset error.

steady-state intake pressure (p_{INT}) to the valve effective area (A_e). A sensitivity of 0.71% of max A_e (≈ 0.043 mm lift) per 1 kPa of p_{INT} is observed in the linear region at 2000 RPM; a better sensitivity of 0.45% of max A_e (≈ 0.027 mm lift) per 1 kPa of p_{INT} is obtained at 1000 RPM. The sensitivity changes with engine speed due to the change in engine flow rate with RPM at the same intake manifold pressure. With an intake pressure sensor capable of measuring changes as small as ± 0.1 kPa, valve lift offsets as small of 0.003 mm can be detected and corrected for. Figure (5.5) shows the HP-EGR estimation error with a reduced valve lift offset error of 0.003 mm using the unsteady orifice equation; the error is within the $\pm 1\%$ bound for all the simulated $\overline{\Delta P}$.

The transfer functions shown in Fig. (5.4) are obtained when the engine reaches steady-state; however, during a DFSO event, the vehicle is decelerating and therefore the engine speed is dropping. Assuming no gear shift is preformed and the vehicle is in a high gear, the decrease in engine speed can be assumed to be small but non-zero. Another set of GT-Power simulations were performed to investigate the impact of different engine speed deceleration rates on the 1000 RPM transfer function obtained if p_{INT} is measured when the engine speed reaches 1000 RPM. Figure (5.6) shows the 1000 RPM transfer functions corresponding to engine speed decelerations of -25 to -100 RPM/s. At the same effective area (A_e), a variation of $\approx 1.5\%$ in p_{INT} between the fastest and slowest speed transients can be observed in the linear region. This translates into a variation in effective area of $\approx 0.4\%$ of max A_e at the same measured p_{INT}, and therefore, can result in a significant relative A_e error at the low valve openings.

Fortunately, the variation of the measured p_{INT} with the rate of engine speed deceleration ($\dot{N} = dN/dt$) is linear at the low valve openings. This can be shown mathematically by first considering a linearized model of the intake manifold filling dynamics where $\Psi^*(p_0, p_{INT}) \approx \beta_0 + \beta_1 p_{INT}$ and $W_{ICE} \approx \alpha_{00} + \alpha_{10} p_{INT} + \alpha_{01} N$:

$$\left[\left(A_\theta + A_e\right)\beta_1 - \alpha_{10}\right] p_{INT} + \left(A_\theta + A_e\right)\beta_0 - \alpha_{00} - \alpha_{01} N = \frac{V_{INT}}{R T_{INT}} \dot{p}_{INT} \tag{5.13}$$

where V_{INT} is the volume of the intake manifold, T_{INT} is intake manifold temperature and R is the air gas constant. The steady-state intake pressure $p_{INT,\mathrm{SS}}$ can be expressed as:

$$p_{INT,\mathrm{SS}} = \frac{-\left(A_\theta + A_e\right)\beta_0 + \alpha_{00} + \alpha_{01} N}{\left(A_\theta + A_e\right)\beta_1 - \alpha_{10}} \tag{5.14}$$

For a ramp in engine speed N at constant rate: $N(t) = N_0 + \dot{N}t$, the steady-state

intake pressure obtained at each instant if the current engine speed $N(t)$ was held constant can be written as:

$$p_{INT,\mathrm{SS}} = \frac{-\left(A_\theta + A_e\right)\beta_0 + \alpha_{00} + \alpha_{01}\left(N_0 + \dot{N}t\right)}{\left(A_\theta + A_e\right)\beta_1 - \alpha_{10}} = \gamma_0 + \gamma_1 \dot{N} t \tag{5.15}$$

Now, Eq. (5.13) can be re-written as:

$$\tau \dot{p}_{INT}(t) + p_{INT}(t) = p_{INT,\mathrm{SS}}(t) = \gamma_0 + \gamma_1 \dot{N} t \tag{5.16}$$

where:

$$\tau = \frac{V_{INT}}{RT_{INT}\left[\left(A_\theta + A_e\right)\beta_1 - \alpha_{10}\right]} \tag{5.17}$$

Equation (5.16) describes a linear 1$^{\mathrm{st}}$ order system with a ramp input. The steady-state response $p^*_{INT}(t)$ is therefore ramp similar to the input but shifted in time by τ:

$$p^*_{INT}(t) = \gamma_0 + \gamma_1 \dot{N}(t - \tau) \tag{5.18}$$

Substituting Eq. (5.15) in Eq. (5.18) gives:

$$p^*_{INT}(t) = p_{INT,\mathrm{SS}}(t) - \dot{N}\tau \tag{5.19}$$

Equation (5.19) shows that for a given speed deceleration rate $\dot{N}$, the measured steady-state intake pressure ($p^*_{INT}(t)$) deviates from the steady-state intake pressure obtained if the current speed was held fixed ($p_{INT,\mathrm{SS}}(t)$) by an amount proportional to the speed deceleration rate ($\dot{N}$). Figure (5.7) shows this behavior for A_e of 1.5%. A linear fit of p_{INT} versus dN/dt results in an R–square above 0.9997 in the linear region.

5.3.2 Experimental Validation

The same experimental setup described in Section 3.4.2 was used to obtain the transfer functions for HP-EGR valve area online calibration at 1000 through 2000 RPM. With fueling turned off, the throttle angle was fixed at the value resulting in $\approx$ 0.3 bar intake manifold pressure at 2000 RPM with the HP-EGR valve fully closed. At each engine speed and starting with a fully closed HP-EGR valve, the EGR valve opening was incremented with 10 second waiting times between each increment to guarantee that the steady-state intake pressure was reached. Figure (5.8) shows the transfer functions relating the steady-state intake pressure (p_{INT}) to the valve

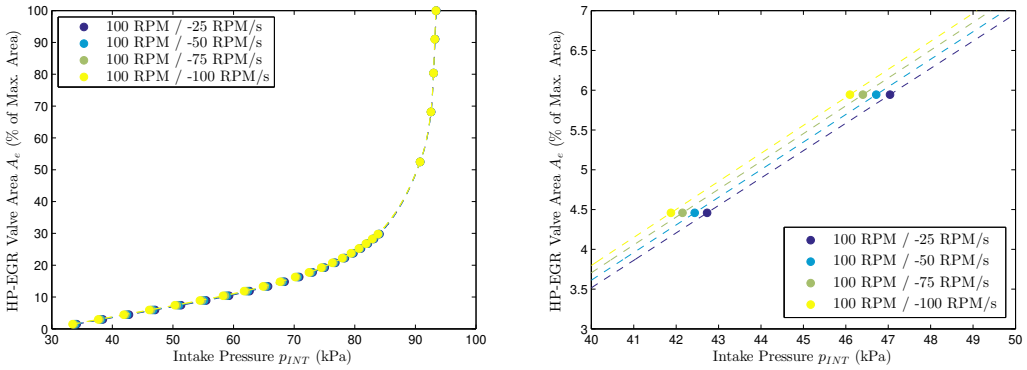

(a) Simulated Transfer Functions

(b) Zoomed-in Transfer Functions

Figure 5.6: Simulated transfer functions for HP-EGR valve area calibration at different engine speeds during an engine speed deceleration.

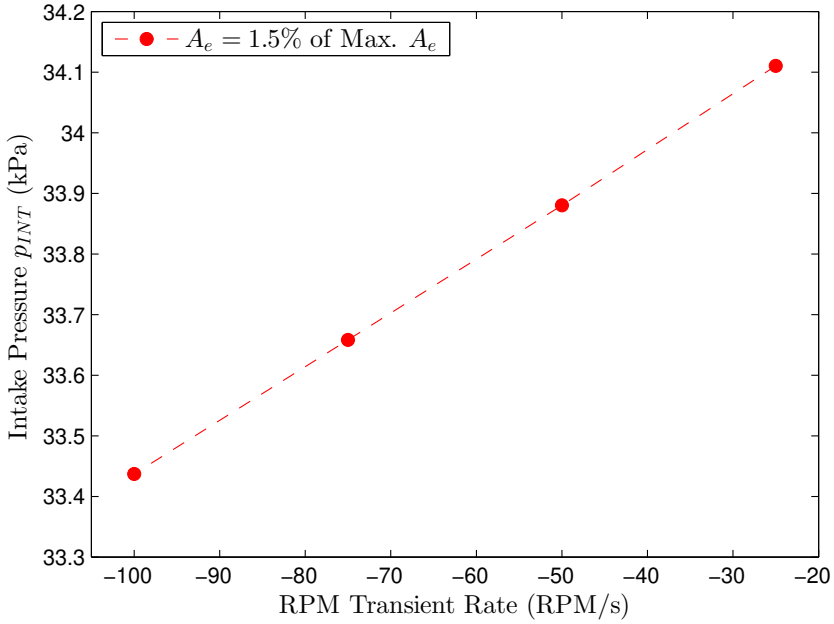

Figure 5.7: Intake Manifold Pressure at $A_e = 1.5\%$ during an engine speed deceleration.

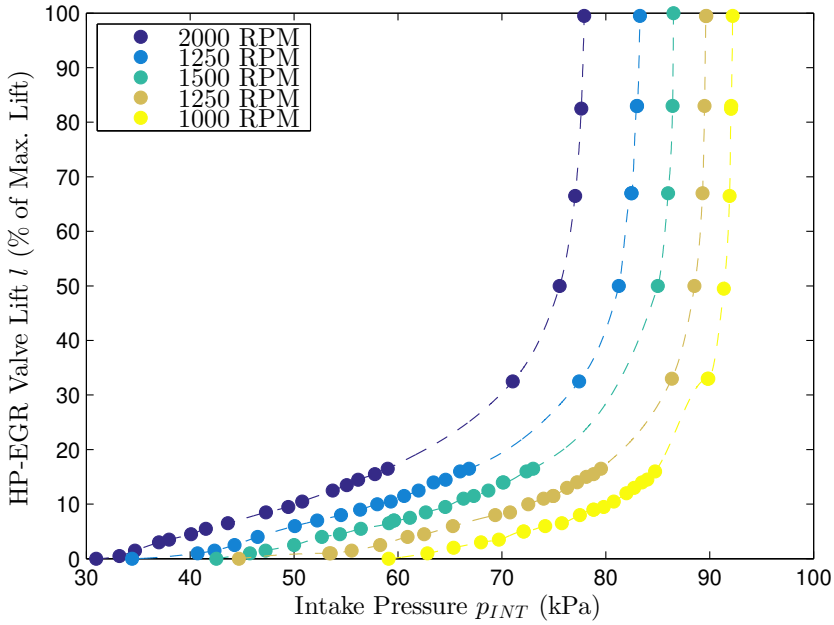

Figure 5.8: Experimental transfer functions for HP-EGR valve area calibration at different engine speeds.

opening. A similar trend to the simulation results was obtained. A sensitivity of 0.034 mm lift ($\approx 0.56\%$ of max A_e) per 1 kPa of p_{INT} is observed in the linear region at 2000 RPM; a better sensitivity of 0.022 mm lift ($\approx 0.36\%$ of max A_e) per 1 kPa of p_{INT} is achieved at 1000 RPM.

5.4 Application of the Online Calibration

The process of generating the transfer functions (Fig. (5.8)) relating the valve effective area (A_e) to the intake manifold pressure (p_{INT}) should be preformed offline using a new HP-EGR valve during the engine calibration process. As the EGR valve ages, the valve effective area can be re-calibrated online during DFSO events. A typical 3 to 5 second DFSO event should be enough for the intake manifold pressure to reach its steady-state value. With the throttle angle fixed at the reference throttle angle used to generate the transfer functions, and commanded valve lift l_c, the steady-state intake manifold pressure (p_{INT}) measured. Using the offline generated transfer functions, the actual effective area corresponding to the measured p_{INT} is computed and then assigned to the commanded valve lift (l_c). The process can then be repeated at other commanded valve lifts during following DFSO events.

5.5 Summary and Conclusions

Small offset errors in the EGR valve effective area resulting from carbon deposits can result in unacceptable EGR estimation errors in the low valve lift – high $\overline{\Delta P}$ region. Restricting the EGR valve operation using a minimum permissible valve opening results in a minimum EGR percentage at the low to mid-loads that exceeds the engine's stability limit, therefore, preventing EGR operations for the HP-EGR case. To address this problem, an online calibration method for the HP-EGR valve area was proposed and evaluated. The proposed online calibration method uses the preexisting intake pressure sensor during deceleration fuel shut-off events and shows promising capability to correct for the effective area errors.

CHAPTER VI

Electric Turbo-Generation

While the previous four chapters are dedicated to addressing the problem of EGR estimation, the second part of this work on waste heat recovery (WHR) is covered in this chapter. An analytical study using the ideal Otto cycle is conducted to assess the main tradeoff between the recovered energy and increased pumping losses due to a WHR expander. More realistic 1-D engine simulations are performed that capture the effects of engine speed, combustion phasing and engine heat transfer. Two boosting methods are considered as shown in Fig. (6.1). A model of a roots-type electric turbo-generator (eTG) is used as the WHR expander. Both low pressure (LP) and high pressure (HP) eTG on a conventional turbocharged (TC) engine are compared to the eTG benefit under a different boosting system. Eaton's electrically assisted variable speed (EAVS) supercharger (Fig. 6.2) is a power split supercharger (PSS) considered in this work as an alternative to the TC. The EAVS supercharger system includes a roots type supercharger, a planetary geartrain, and an electric motor (Fig. (6.1(c))). The planetary geartrain allows the supercharger to spin at a variable speed ratio to the crankshaft by varying the electric motor speed. When no boost is required, the EAVS supercharger (SC) can be declutched from the crankshaft and braked to avoid unnecessary friction losses. Other capabilities of the EAVS supercharger are detailed elsewhere [53]. The eTG benefits are evaluated and quantified over the engine map under both boosting systems using the percent change in system brake efficiency metric. Then a simplified steady-state visitation point based method [54] is used to estimate the reduction in fuel consumption (FC) possible with the eTG for the Ford Escape and Fusion over the EPA city (FTP), highway (HWY) and US06 drive cycles. All recovered energy is assumed to be reused during the cycle at a representative engine efficiency of 30% with 10% losses in the electrical path. The analysis shows that the EAVS SC-eTG is overall the better boosting and turbogeneration system as the EAVS SC-eTG setup (boost-by-wire) achieved the highest FC reductions.

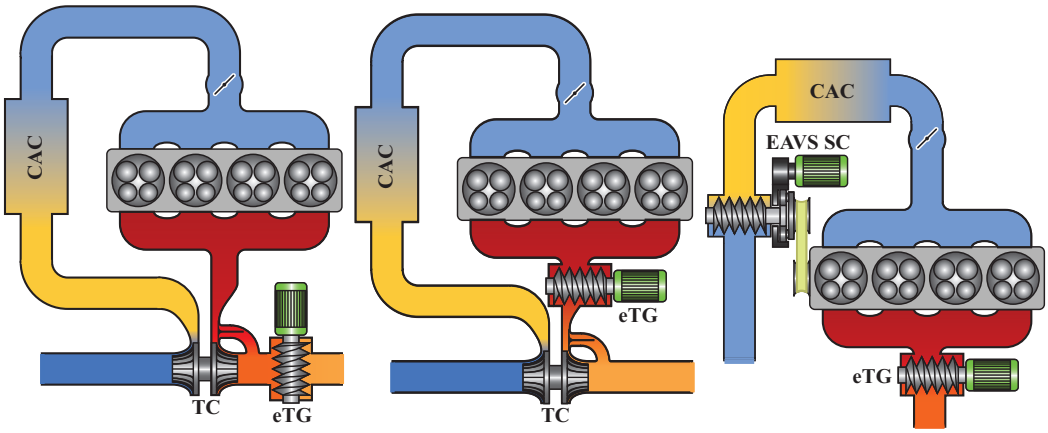

(a) TC-LP eTG (b) TC-HP eTG (c) EAVS SC-eTG

Figure 6.1: Turbocharged engine with LP-eTG (6.1(a)), turbocharged engine with HP-eTG (6.1(b)) and hybrid-supercharged engine with eTG (boost-by-wire) (6.1(c)).

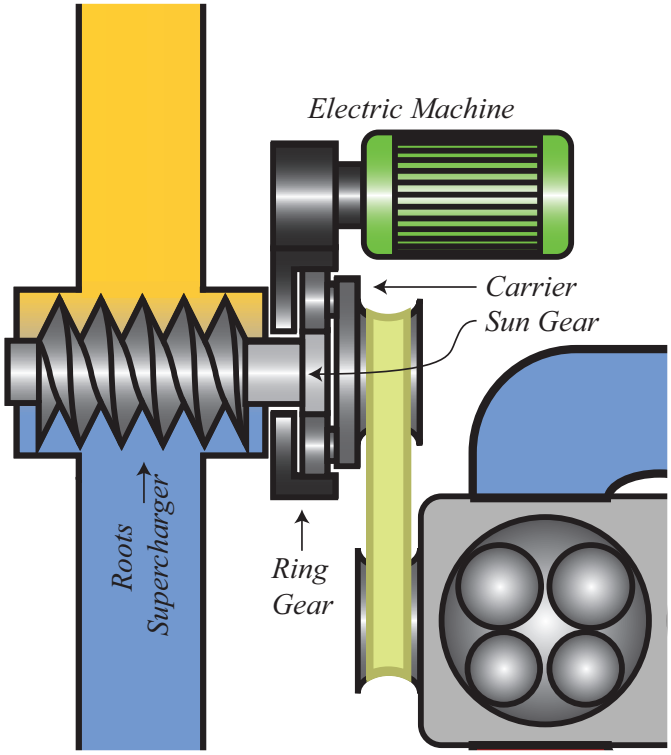

Figure 6.2: Eaton's electrically assisted variable speed (EAVS) supercharger showing the roots-type supercharger attached to planetary geartrain sun gear, the electric machine driving the ring gear, and the carrier coupled to the engine crank through a pulley system.

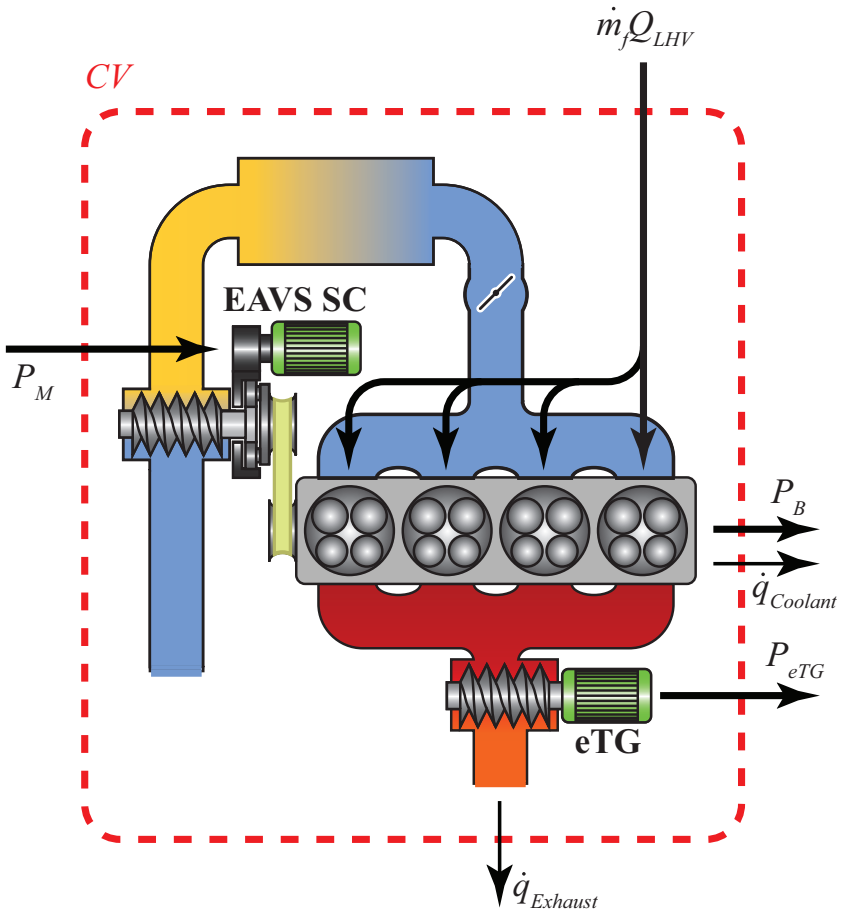

Figure 6.3: Control volume for the hybrid-supercharged engine with eTG showing power flows. $\dot{m}_f Q_{LHV}$ denotes the input power flow from fuel, P_B is the engine brake power, P_{eTG} is the eTG power, P_M is the EAVS supercharger motor power, $\dot{q}_{Coolant}$ is the coolant rejected heat, and $\dot{q}_{Exhaust}$ is the exhaust rejected heat.

6.1 eTG Performance Evaluation

Various engine losses accompany the addition of an expander in the engine exhaust. The flow restriction increases exhaust back pressure and results in higher pumping losses. To maintain engine brake load, the engine must operate at higher gross indicated power to compensate for the additional losses. The fraction of trapped in-cylinder residuals also increases due to the increased back pressure. The resulting shifts in engine gross indicated load and trapped residuals affect the combustion and heat transfer processes. All these factors need to be included to evaluate the potential benefits of the eTG recovered power.

To that end, a control volume (CV) around the engine is considered. Input

power from fuel ($\dot{m}_f Q_{LHV}$) and the EAVS supercharger motor (P_M), and output power from the crank and eTG (P_B and P_{eTG}) as well as heat flows ($\dot{q}_{Coolant}$ and $\dot{q}_{Exhaust}$) from the system are included. Figure 6.3 shows this CV for the hybrid-supercharged configuration, while the same flows, except for P_M, are also present in both turbocharged cases (not shown). A percent change in system brake efficiency metric ($\Delta\eta_{b,SYS}$) is defined for evaluating the eTG performance where the system brake efficiency with the eTG ($\eta_{b,SYS}$) is:

$$\eta_{b,SYS} = \frac{P_B - P_M + P_{eTG}}{\dot{m}_f Q_{LHV}} \tag{6.1}$$

The expression of the baseline engine brake efficiency ($\eta_{b,0}$) is similar to $\eta_{b,SYS}$ with $P_{eTG} = 0$ as the device is not present. The EAVS supercharger motor power P_M is also zero for the turbocharged cases.

6.2 Ideal Engine Cycle Analysis

As a first step to understand the potential of an eTG, an ideal engine cycle analysis is developed to provide valuable insight into the main eTG tradeoff under simplified conditions: recovered power versus additional pumping losses. The ideal Otto-cycle with isentropic compression, constant volume heat addition, isentropic expansion, isentropic blow-down, and ideal intake and exhaust displacements is considered for a naturally-aspirated engine. The trapped in-cylinder mass is determined using the ideal gas law assuming the intake valve closes at intake bottom dead center (BDC) with in-cylinder pressure equal to the intake pressure (p_i). The magnitude of constant volume heat addition is calculated from the fuel energy of a stoichiometric fuel mass assuming gasoline fuel with lower heating value (Q_{LHV}) of 43.4 MJ.kg^{-1}.

The system brake efficiency defined in Eq. (6.1) can be expressed as:

$$\begin{aligned} \eta_{b,SYS} &= \eta_{IG} \frac{P_{b,SYS}}{P_{b,SYS} + P_F + P_{P,0} + \Delta P_P + P_M - P_{eTG}} \\ &= \eta_{IG} \frac{P_{b,SYS}}{P_{b,SYS} + P_F + P_{P,0} - NRP} \end{aligned} \tag{6.2}$$

where $P_{b,SYS} = P_B - P_M + P_{eTG}$ is the system brake power, P_F is the frictional power, $P_{P,0}$ is the baseline pumping power, ΔP_P is the increase in pumping power due to the eTG (detailed derivation is presented elsewhere [55]). Using the described Otto-cycle, the engine gross indicated efficiency η_{IG} does not vary with increasing back pressure

and P_M is zero. The variation of P_F with load is neglected, and $P_{P,0}$ is constant by definition. As a result, the only engine loss resulting from the addition of the eTG is the increased pumping loss. In this situation, we can use the net recovered power (NRP) metric, defined as $P_{eTG} - \Delta P_P$ (when $P_M = 0$), to capture the variable terms. The detailed derivation of the NRP expression is presented elsewhere [55]; the key equations along with the analysis results are shown below.

The flow restriction due to the addition of the eTG increases the exhaust manifold pressure by some Δp_e. Therefore, an increase of Δp_i in the intake manifold pressure is required to maintain the airflow and the load. The sensitivity of the change in pumping power (ΔP_P) to Δp_i is equal but opposite to that of Δp_e:

$$\Delta P_P = \frac{V_D N}{2} \left(\Delta p_e - \Delta p_i \right) \tag{6.3}$$

where V_D and N denote displaced volume and engine speed. However, the change in intake manifold pressure also contributes to the engine load by affecting the trapped charge mass, and therefore fueling. As a result, the overall load sensitivity to Δp_i is larger than that to Δp_e. Therefore, the Δp_i required to maintain load is smaller than Δp_e, leading to increased pumping losses. The Δp_e also contributes to the engine load by reducing the volumetric efficiency due to the increase in trapped residuals, but this contribution is small compared to that of Δp_i to the trapped charge mass.

The relation between ΔP_P and Δp_e while engine load is maintained can be expressed as:

$$\Delta P_P = \frac{V_D N}{2} \Delta p_e \left(1 - C_{\Delta i, \Delta e} \right) \tag{6.4}$$

where

$$C_{\Delta i, \Delta e} = \frac{\Delta p_i}{\Delta p_e} = \frac{1}{\eta_{IG} \dfrac{Q_{LHV}}{f' + 1} \dfrac{1}{R T_1} + 1} \tag{6.5}$$

η_{IG} is the indicated gross efficiency, f' is the charge-to-fuel ratio, Q_{LHV} is the fuel lower heating value, R is the charge's gas constant, and T_1 is the charge temperature at intake bottom dead center (BDC).

The increase in pumping losses ΔP_P is a linear function in Δp_e and is independent of load. However, the expander power:

$$P_{eTG} = \eta_s \dot{m} c_p \overline{T}_e \left(1 - \left(\frac{p_e + \Delta p_e}{p_e} \right)^{\frac{1-\gamma}{\gamma}} \right) \tag{6.6}$$

is a strong function of engine load due to its dependence on engine mass flow rate $\dot{m}$ and exhaust temperature $\overline{T}_e$, which both increase with increasing load. Therefore, there may exist a minimum engine load below which the expander power is not large enough to offset the increase in pumping power. The ideal Otto-cycle is used to determine the unknown parameters η_{IG} and $\overline{T}_e$ in Equations (6.4) and (6.6) so the potential benefits of an eTG can be evaluated for different engine loads.

The net recovered power can then be computed as the difference between the eTG power and the increase in pumping power:

$$\begin{aligned} NRP &= P_{eTG} - \Delta P_P \\ &= \eta_s \dot{m} c_p \overline{T}_e \left(1 - \left(\frac{p_e + \Delta p_e}{p_e}\right)^{\frac{1-\gamma}{\gamma}}\right) - \Delta P_P \end{aligned} \tag{6.7}$$

The expander NRP can be normalized to calculate the net recovered mean effective pressure (MEP), shown on Fig. (6.4) for various loads with an isentropic expander ($\eta_s = 1$). The thick dashed lines indicate that the isentropic blow-down assumption does not hold for the corresponding Δp_e, while the fine dashed lines indicate that $p_i > 1$ bar is required to maintain load (i.e. the naturally aspirated assumption does not hold). The intake pressure p_i is determined from the brake mean effective pressure (BMEP) as:

$$p_i = (p_e + \text{BMEP} + \text{FMEP}) C_{\Delta i, \Delta e} \tag{6.8}$$

where the friction mean effective pressure (FMEP) is assumed constant at 0.5 bar.

Figure (6.4) shows that for a perfect isentropic expander, a positive net recovered power can be obtained for all loads. However, this is not the case for an expander with a more feasible 60% isentropic efficiency as shown in Fig. (6.5). There exists a minimum load of around 4 bar BMEP below which a positive net recovered power cannot be achieved. Below this load, the expander power is not large enough to offset the increase in pumping losses. At higher loads increasing Δp_e does not necessarily result in a larger net recovered MEP. This is due to the steeper slope of ΔP_P versus Δp_e compared to the asymptotic direction of P_{eTG} for the given isentropic efficiency η_s. As a result, the maximum net recovered power exists at an intermediate Δp_e value, beyond which larger Δp_e results in diminishing returns. Finally, at the higher loads (such as 11 bar BMEP) the maximum net recovered power is restricted by the inability to maintain the desired load for higher Δp_e values. Higher back pressures require an intake pressure above atmospheric for the modeled naturally-aspirated engine.

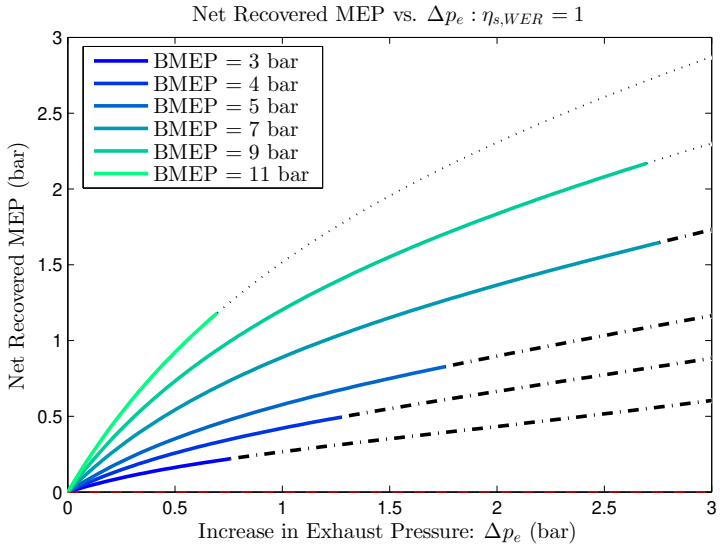

Figure 6.4: Net recovered MEP versus Δp_e across the expander for various engine loads using an isentropic expander ($\eta_s = 1$). Dotted lines indicate that the desired BMEP cannot be achieved for the given increase in exhaust back pressure for a naturally-aspirated (NA) engine. Dashed-dotted lines indicate that exhaust manifold pressure exceeds the in-cylinder pressure just before blow-down, and therefore, the isentropic blow-down assumption doesn't hold.

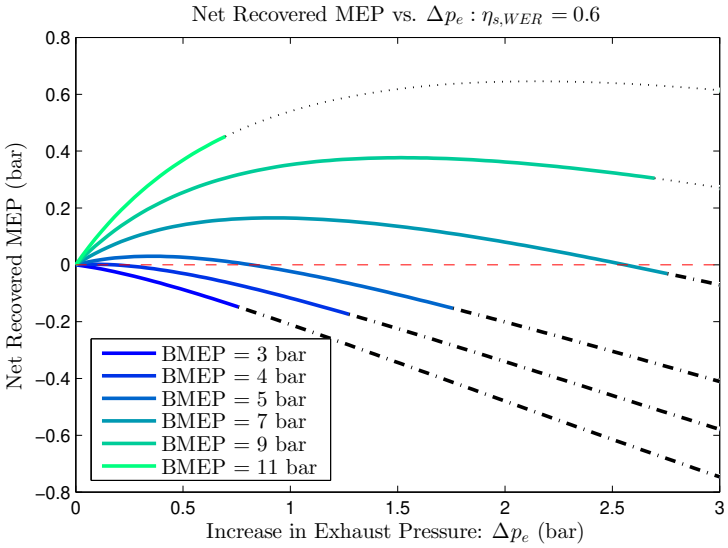

Figure 6.5: Net recovered MEP versus Δp_e across the expander for various engine loads using an expander with $\eta_s = 0.6$. Dotted lines indicate that the desired BMEP cannot be achieved for an NA engine. Dashed-dotted lines indicate that the isentropic blow-down assumption doesn't hold.

6.3 GT-Power Analysis

While the ideal engine cycle analysis presented in the previous section gives valuable insights into the main trade-offs present, more detailed simulations are required to capture engine speed, combustion phasing, heat transfer and variable valve timing effects that the ideal engine cycle analysis cannot reproduce. The GT-Power engine model of the Ford 1.6 L EcoBoost engine developed for the HP-EGR simulations (described in Chapter II subsection 2.1.2) was modified and used to estimate the possible waste heat recovery with an expander in the exhaust. Three configurations were considered: a turbocharged engine with LP-eTG, a turbocharged engine a HP-eTG, and a hyrbrid-supercharged engine with the eTG (Fig (6.1)).

For all configurations, engine simulations with no EGR were performed over a grid of engine speeds (1000 to 3500 RPM) and intake pressures (0.3 to 2.0 bar absolute) to cover the bulk of the operating conditions visited during a drive cycle. At each speed and load, the expander speed was swept to find the optimal system brake efficiency. Intake variable cam timing (VCT) and exhaust VCT were determined based on 2-D maps indexed by engine speed and intake manifold pressure derived from the stock ECU strategy. Boost pressure was determined in a similar fashion to intake and exhaust VCT for both turbocharged engines. However, no boost reserve is required for the EAVS supercharged engine due its faster transient response [56], and a wide open throttle was imposed when the EAVS supercharger operates in boosting mode. When no boost is required, the EAVS supercharger was declutched from the crankshaft and braked. The EAVS SC model was provided by Eaton. The knock-limited maximum brake torque (MBT) spark timing was determined for each case by adjusting spark timing subject to an EGR sensitive knock constraint (same as used for the HP-EGR simulations). The expander isentropic efficiency was set to a constant 60%, an efficiency typical of positive displacement expanders.

Figure (6.6) shows the variation of different TC-engine parameters at 2000 RPM and 12 bar BMEP with LP-eTG speed. In this case, the turbo could not provide sufficient boost to meet the desired load for eTG speeds lower than 14,000 RPM, due to high back pressure. At speeds higher than 18,000 RPM, the eTG acts as compressor instead of an expander resulting in a pressure upstream of the eTG that is lower than the pressure downstream of it[1]. These two factors limit the range of feasible eTG speeds. Consistent with the findings of the previous section, the increase in exhaust

[1]The pressure downstream of the eTG is roughly atmospheric at low exhaust flow rates. This can result in pressures lower than atmospheric upstream of the eTG when it operates as a compressor.

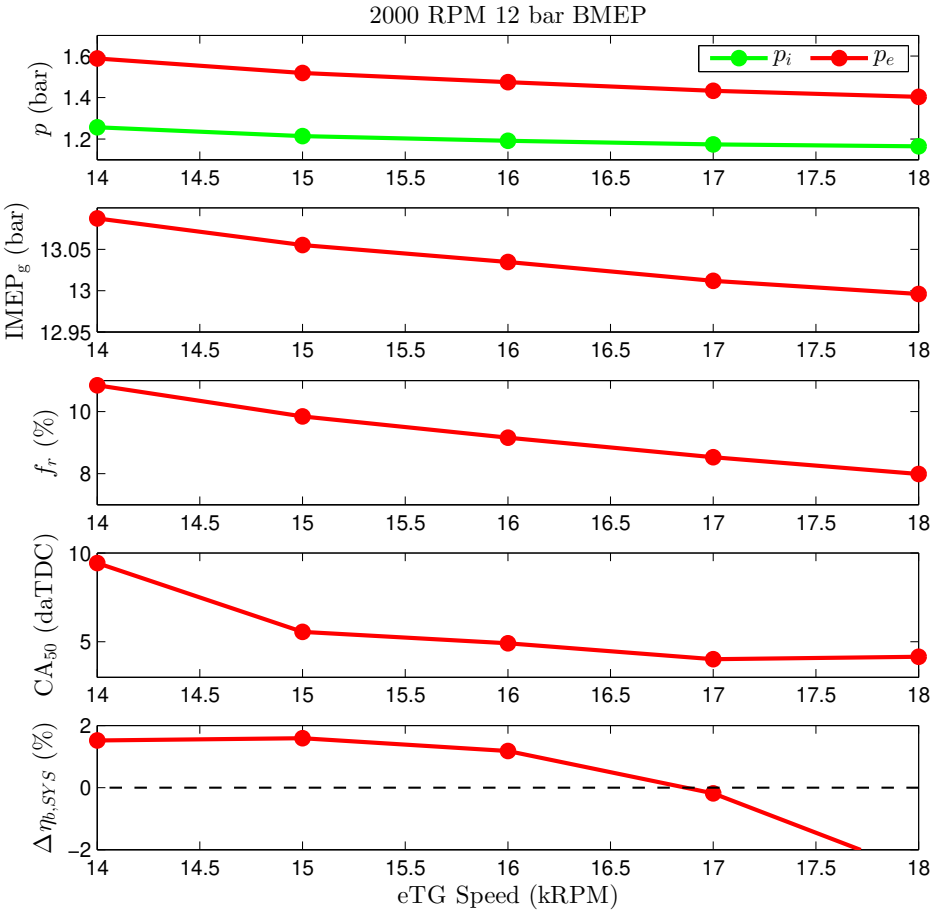

Figure 6.6: Engine parameters as a function of eTG speed. From top to bottom: intake (p_i) and exhaust (p_e) pressures, gross indicated mean effective pressure (IMEP$_g$), percentage of trapped residuals (f_r), crank angle at 50% burned charge (CA$_{50}$), and percent change in brake system efficiency ($\Delta\eta_{b,SYS}$).

back pressure with decreasing eTG speed is accompanied with a smaller increase in intake pressure resulting in an overall increase in pumping losses. The increased pumping losses require the engine to operate at higher gross indicated power to maintain the same brake load (Fig. (6.6)). This shift in the gross indicated load makes the engine more prone to knock at the mid to high-loads and results in less optimal combustion phasing. The increased back pressure also traps more internal residuals (Fig. (6.6)). Although cooled exhaust gas recirculation (EGR) helps mitigate knock, the increased charge temperature due to increased internal EGR further increase the knocking tendency requiring even more spark retard [18]. Figure (6.6) shows the effect of increased knocking tendency on CA_{50}. This increased knock tendency with higher back pressures due to increased trapped residual fraction was also reported by Dijkstra *et al.* [17]. As a result, the NRP simplification used in the ideal cycle analysis is insufficient to capture the engine behavior and we must use the percent change in the system brake efficiency metric, $\Delta\eta_{b,SYS} = 100(\eta_{b,SYS} - \eta_{b,0})/\eta_{b,0}$, instead. Figure (6.6, *Bottom*) shows $\Delta\eta_{b,SYS}$ as a function of the eTG speed. In this case the optimal eTG speed resulting in the highest $\Delta\eta_{b,SYS}$ is 15,000 RPM. Increasing back pressure by lowering the expander speed beyond 15,000 RPM results in diminishing returns: $\Delta\eta_{b,SYS}$ drops from 1.59% at 15,000 RPM to 1.52% at 14,000 RPM.

Case	System	Baseline
A	Turbocharged engine with LP-eTG	Turbocharged engine
B	Turbocharged engine with HP-eTG	Turbocharged engine
C	Supercharged engine with eTG	Supercharged engine
D	Supercharged engine with eTG	Turbocharged engine

Table 6.1: System-baseline combinations under considerations.

To isolate the potential benefits of the eTG, the percent change in system brake efficiency ($\Delta\eta_{b,SYS}$) of the turbocharged engine with LP-eTG or HP-eTG is computed relative to the baseline turbocharged engine. Similarly, the baseline used for evaluating $\Delta\eta_{b,SYS}$ for the supercharged engine with eTG is the unmodified supercharged engine. A fourth case is also considered where $\Delta\eta_{b,SYS}$ is computed for the supercharged engine with eTG relative to the baseline turbocharged engine in order to evaluate the overall improvement of replacing the TC with the EAVS supercharger (SC) along with the addition of the eTG. Those 4 cases are summarized in Table (6.1). The optimal eTG speed for all engine speeds and loads is determined for all 4 cases, with the resulting optimal $\Delta\eta_{b,SYS}$ shown in Fig. 6.7. The increase in percent trapped residuals relative to the baseline case (without eTG) obtained at the

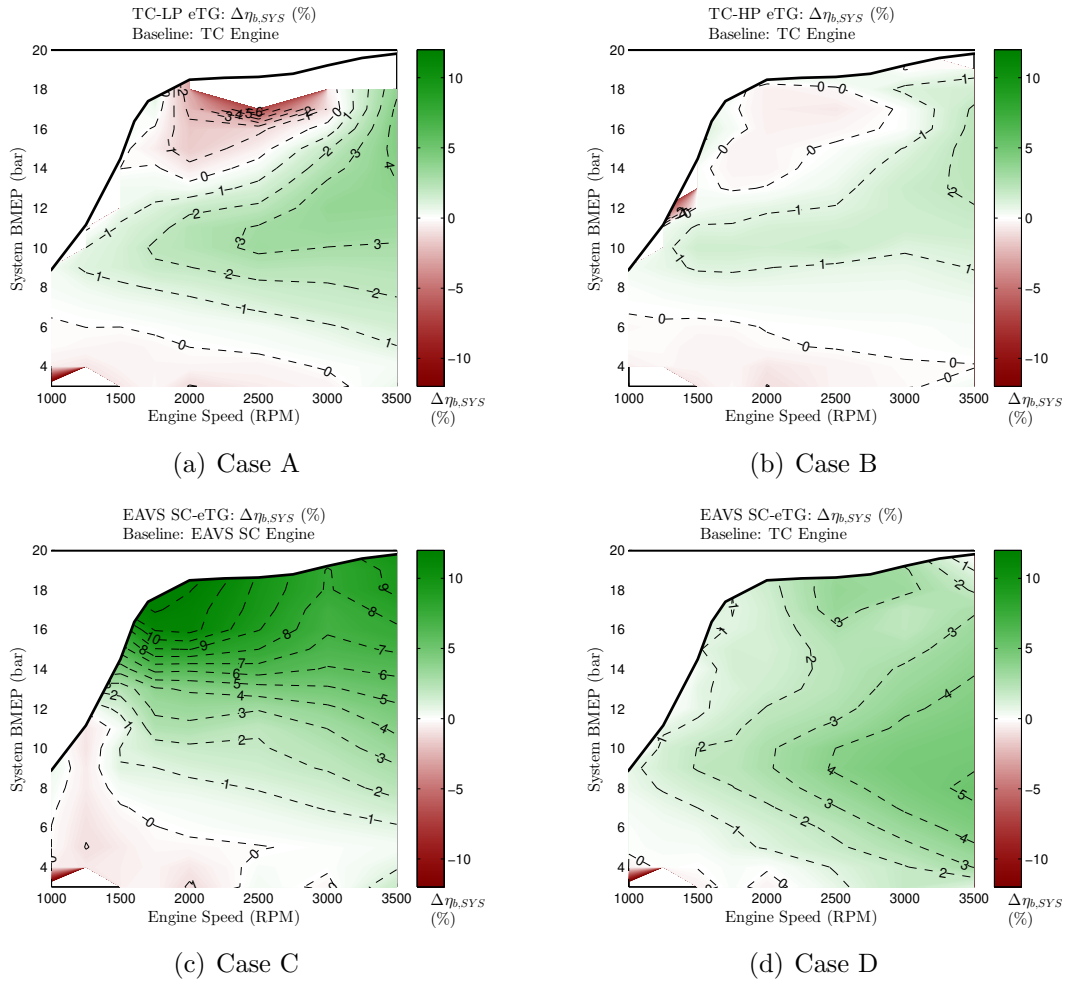

(a) Case A

(b) Case B

(c) Case C

(d) Case D

Figure 6.7: Percentage change in system brake efficiency ($\delta\eta_{b,SYS}$). The solid black line shows the wide open throttle (WOT) BMEP of the baseline engine versus engine speed.

optimal eTG speed is shown in Figure (6.8) for the Case A. The maximum increase in internal residuals occurs at mid-load which is expected from the ideal cycle results depicted in Fig. 6.5 where the optimal increase in back pressure Δp_e is the highest at the mid-loads.

Consistent with the previous section, there exists a lower bound on load below which the eTG has a negative impact. However, this lower bound decreases with increasing engine speed (Fig. (6.7)). The higher exhaust temperature present at higher engine speeds results in higher expander power (Eq. (6.6)) for the same extra pumping (and other engine losses). Accounting for these additional engine losses beyond just increased pumping shows an additional region in the speed-load space, high loads and low speeds, where using the eTG is detrimental for the turbocharged

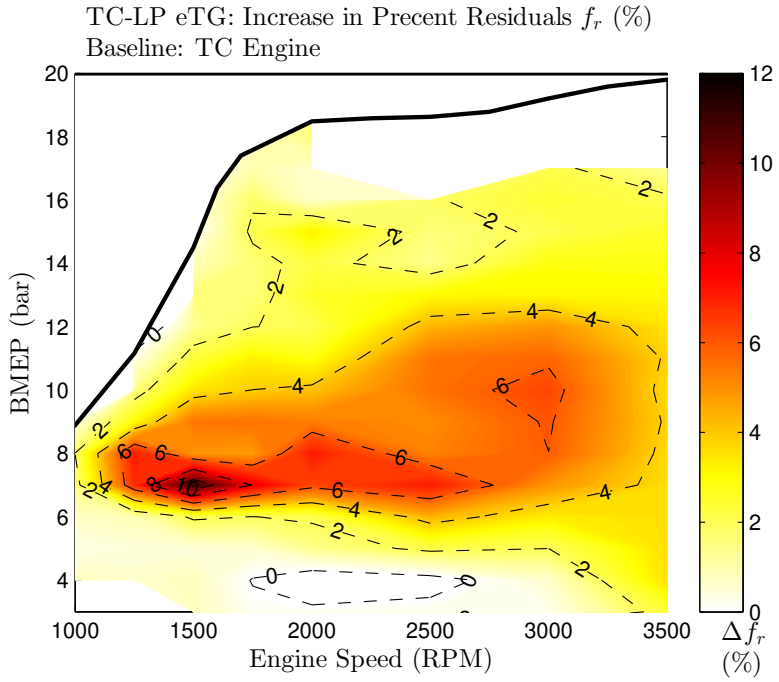

Figure 6.8: Increase in trapped internal residuals: the TC engine with a LP-eTG relative to the baseline TC engine (Case A) obtained at maximum $\Delta\eta_{b,SYS}$.

engines (Cases A and B). As a result, the engine operating points that can benefit from the eTG are restricted to the mid-loads (Fig. (6.7(a)) and (6.7(b))). The simulations show that the LP-eTG provides higher $\Delta\eta_{b,SYS}$ than the HP-eTG over most of the simulated region of engine speeds and loads. This is attributed to additional TC turbine wastegating in the HP-eTG case.

Since the TC engine with LP-eTG achieves higher $\Delta\eta_{b,SYS}$ than the HP-eTG, the rest of the chapter will compare and discuss the TC-LP eTG and the EAVS SC-eTG cases. Adding the LP-eTG to a turbocharged engine (Fig. (6.7(a))) shows improvements in $\eta_{b,SYS}$ up to 4% at the mid-loads. Fig. 6.9(a) shows the additional retard in CA_{50} at the optimum $\Delta\eta_{b,SYS}$ relative to the baseline turbocharged engine. Up to 10^o additional retard in combustion phasing can be observed at the high loads. The cyan and blue lines correspond to the boundary where spark timing is retarded away from MBT to mitigate knock for the baseline and engine with LP-eTG respectively. The simulations show a significant increase in the region where spark retard is required.

Figure (6.7(c)) shows the improvement in $\eta_{b,SYS}$ with the addition of the eTG to the supercharged baseline engine. Similar to the turbocharged case, the eTG power

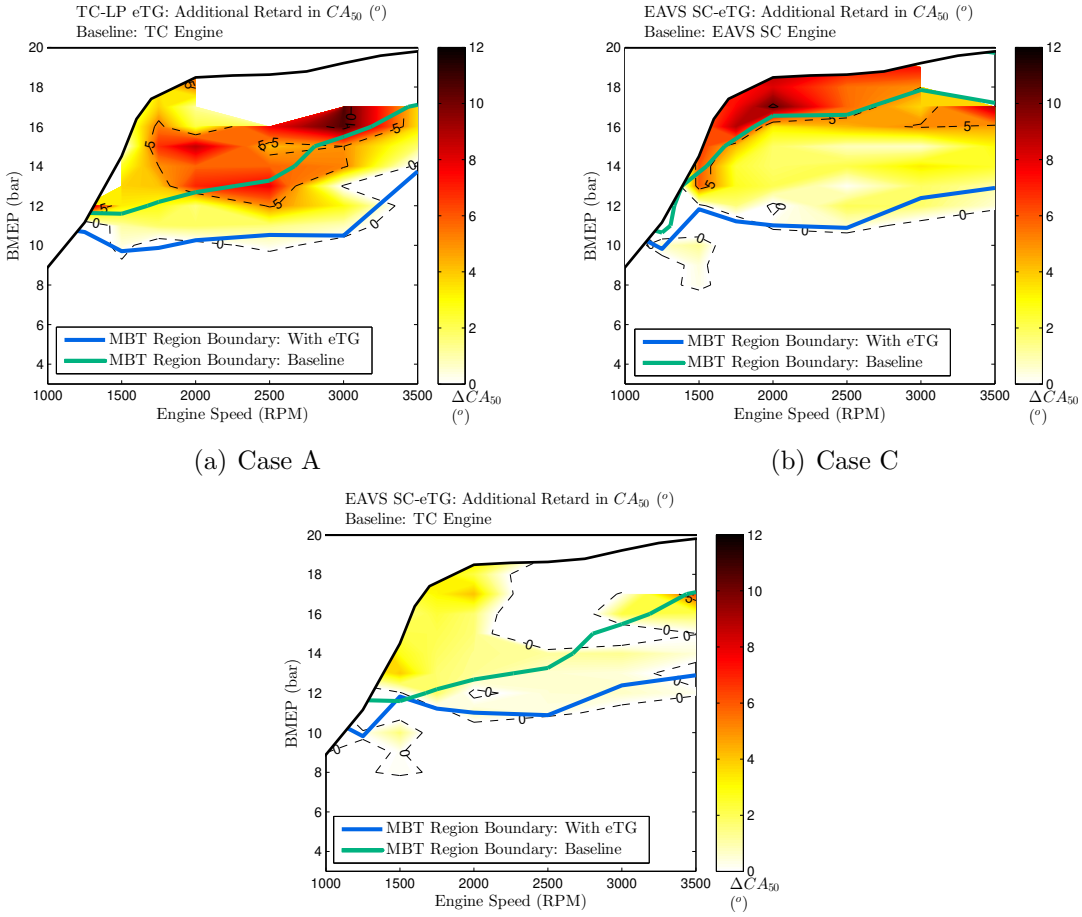

(a) Case A

(b) Case C

(c) Case D

Figure 6.9: Retard in CA_{50} at maximum $\Delta\eta_{b,SYS}$. The cyan and blue lines correspond to the boundary of knock-limited MBT spark timing for the baseline and engine with LP-eTG respectively.

at the low load is insufficient to offset the increase in pumping losses. However, an opposite trend is observed at the higher loads. The eTG improves $\eta_{b,SYS}$ by up to 12%. Figure (6.9(b)) shows additional retard in CA_{50} up to 10^o at the high loads similar to the turbocharged case. However, this deterioration of combustion phasing occurs at much higher eTG recovered power. This behavior is due to the higher temperature T_i at the eTG inlet for Case C (due to the absence of the TC turbine) which requires, for the same eTG power as Case A, a smaller increase in back pressure, and therefore, less pumping losses and lower trapped residuals.

Figure (6.7(d)) shows the overall improvement in system brake efficiency when the TC is replaced with the EAVS SC along with the addition of the eTG. A low load region still exists where the eTG is detrimental. However, this region is smaller compared to Case A (Fig. (6.7(a))) that was the same turbocharged baseline. This improvement is the result of lower engine back pressures from removing the TC and the boost reserve requirement. Case D shows larger $\eta_{b,SYS}$ improvements over most of the simulated region compared to Case A. At high loads, the eTG and EAVS SC improves $\eta_{b,SYS}$ by up to 4%. This improvement is considerably smaller than that of Case C (Fig. (6.7(c))) because of the EAVS SC detrimental parasitic losses in the boosted region relative to the TC engine.

Finally, it should be mentioned that the eTG performance with the presence of LP-EGR is worth investigating. At a given brake load, the EGR increases engine mass flow which contribute to a larger eTG power. However, the reduced exhaust temperature has the opposite effect. A previous study indicates that relative decrease in temperature is smaller than corresponding relative increase in mass flow [57]. This can potentially lead to larger eTG improvements and requires further study.

6.4 Drive Cycle Fuel Consumption Improvements

With optimal eTG operating points determined based on the optimal $\Delta\eta_{b,SYS}$ from the previous section, the reduction in fuel consumption (FC) can be estimated for a given vehicle and drive cycle. A steady-state method that employs 13 carefully chosen visitation points, along with a representative time spent at each point, was used to estimate the fuel consumed by the 2015 Ford Escape and 2012 Ford Fusion over the EPA city (FTP), highway (HWY) and US06 drive cycles. This visitation point based approach is detailed by Middleton [54].

The fuel mass consumed for the eTG and baseline configurations (m_f and $m_{f,0}$ respectively) over a drive cycle is estimated by summing the product of fuel flow

rate ($\dot{m}_i$ and $\dot{m}_{i,0}$) consumed at each visitation point i and time (t_i) spent in the region surrounding that visitation point. The mass flow rate $\dot{m}_i$ is set to the fuel flow of the baseline case, $\dot{m}_{i,0}$, if at visitation point i, the change in system brake efficiency is negative. This is consistent with bypassing the eTG when its use would be detrimental.

The expander (gross) recovered energy can be computed in the same fashion:

$$RE = \eta_E \sum_i P_{eTG,i} t_i \tag{6.9}$$

where η_E is the efficiency of the electrical path, and $P_{eTG,i}$ is set to zero if the percent change in system brake efficiency at visitation point i is negative. A detailed strategy for utilizing the eTG power has not yet been developed and is the subject of future work. However, a preliminary estimate of the benefit of the eTG can still be obtained by assuming that all the recovered energy RE can be reused during the cycle at some representative engine efficiency η_{ICE}. The equivalent fuel energy (EFE) replaced by RE can be computed using:

$$EFE = \frac{RE}{\eta_{ICE}} \tag{6.10}$$

While the mass of fuel replaced by using the eTG RE is:

$$m_{f,eTG} = \sum_i \frac{\eta_E P_{eTG,i}}{\eta_{ICE} Q_{LVH}} t_i \tag{6.11}$$

The effective overall increase in fuel consumption $\Delta m_{f,EFF} = m_f - m_{f,0} - m_{f,eTG}$ can then be estimated as:

$$\Delta m_{f,EFF} = \sum_i \left[\dot{m}_i - \dot{m}_{i,0} - \frac{\eta_E P_{eTG,i}}{\eta_{ICE} Q_{LVH}} \right] t_i \tag{6.12}$$

Assuming a 90% efficiency for the electric path (η_E), and 30% representative engine efficiency (η_{ICE}), the percent reduction in FC for Cases A, C and D is shown in Table 6.2. The Escape shows larger FC improvements with the eTG than the Fusion, and both vehicles show larger improvements on the US06 compared to the city (FTP) and highway cycles. In general, engine loads where the eTG is more effective are more frequently visited with heavier vehicles and more aggressive cycles. Comparing Cases A and C, the supercharged engine benefits more from the addition of the eTG than the turbocharged engine over the city and US06 cycles, while the trend is reversed for the highway cycle. Comparing Cases A and D, the overall FC improvement achieved

by replacing the TC with the EAVS SC plus eTG system is larger than that obtained with only adding the eTG for both vehicles and over all 3 drive cycles.

Table 6.2: Fuel consumption improvements with the 60% efficient eTG expander for the Escape and Fusion over the FTP, highway and US06 drive cycles computed for Cases A, C and D.

Vehicle	Drive Cycle	Reduction in FC (%) Case A	Case C	Case D
Escape	FTP	0.8	0.9	1.4
	HWY	2.0	1.3	2.4
	US06	3.9	4.6	4.6
Fusion	FTP	0.7	0.8	1.3
	HWY	1.6	1.0	1.9
	US06	3.6	4.2	4.3

Table 6.3: Case D fuel consumption improvements for the Escape and Fusion over the FTP, highway and US06 drive cycles estimated for various eTG expander efficiencies.

Vehicle	Drive Cycle	Reduction in FC (%) $\eta_s = 60\%$	$\eta_s = 70\%$	$\eta_s = 80\%$
Escape	FTP	1.4	1.9	2.7
	HWY	2.4	3.5	4.7
	US06	4.6	5.9	7.8
Fusion	FTP	1.3	1.8	2.5
	HWY	1.9	2.8	4.0
	US06	4.3	5.5	7.3

While current roots-type expanders can achieve a peak efficiency of 65%, centrifugal turbine efficiences can exceed 70%. To highlight the potential of a best case scenario as well as to quantify the sensitivity of the results to device efficiency, the percent reduction in FC achieved by replacing the TC with the EAVS SC plus eTG by was performed with different isentropic efficiencies of the WHR expander (Table 6.3). The FC improvements are non-linear and very sensitive to the expander isentropic efficiency. Increasing the expander efficiency from 60% to 80% (33% relative increase) results in almost doubling the reduction in FC over the city (FTP) and highway (HWY) cycles, and a 70% additional FC reduction over the US06.

Finally, it should be noted that the current steady state drive cycle FC estimates do not account for transient effects. Nazari *et al.* [58] simulated tip-ins on an engine

with an eTG and showed that the transient response of the eTG has a significant impact on the FC during the transients. The dynamic response of the SC also affects the cycle FC [56] which would impact Case D improvement. Therefore, full drive cycle simulations, capable of capturing potential losses through non-equilibrium operation (constantly accelerating and decelerating to adjust to the optimal eTG speed), are required to validate the presented steady-state FC estimates. The full drive cycle simulations are also important to evaluate battery size requirements and potential benefits from offloading electric auxiliary loads using the eTG electrical energy.

6.5 Experimental Validation

Experimental validation of the GT-Power simulations was performed with a turbocharged engine in the LP-eTG configuration at engine speeds of 2000 to 3000 RPM and loads of 10 to 14 bar BMEP. These conditions were selected from the simulation results indicating relative net increases of brake system efficiency between 2 and 3%. At each point, the expander speed, and therefore the pressure ratio across it, were varied. Recovered power up to 2.2 kW was observed. Positive net changes in brake system efficiency were achieved at only one engine operating point (2500 RPM, 12.5 bar BMEP) with a maximum improvement below 0.4%. The eTG was detrimental for the remaining cases. The computed eTG efficiencies from experimental data are unexpectedly low with $\approx 20\%$ efficiency at the best case. The excessive cooling of the prototype roots expander could be the main cause explaining the low observed efficiencies.

6.6 Summary and Conclusions

This chapter evaluated waste heat recovery using electric turbo-generation (eTG) on boosted SI engines. Ideal engine cycle analysis was performed to establish a simple and insightful relationship between the net recovered power and load. The increase in pumping losses due to the eTG was shown to be load-independent. The eTG power on the other hand scaled proportionally with engine mass flow rate and exhaust temperature, and therefore, increased with load. As a result, there exists a minimum load below which the eTG power is insufficient to offset the increase in pumping losses. It is also shown that increasing the pressure ratio across the eTG does not necessarily lead to increased net recovered power. Beyond some optimal pressure ratio, the increase in eTG power becomes smaller than the increase in pumping,

resulting in diminishing returns.

GT-Power engine simulations confirmed the negative impact of the eTG at low loads for turbocharged and hybrid-supercharged engines. The shift in engine operation into more knock prone regions made the low pressure (LP) and high pressure (HP) eTG detrimental at the high loads on the turbocharged engines. The regions where the eTG can improve the overall system efficiency was therefore limited to the mid-loads with the LP-eTG providing greater improvements. However, the eTG improved the brake system efficiency at both the mid and high loads for the hybrid-supercharged case. Despite the negative impact of the eTG on combustion phasing, the eTG recovered power at the high loads exceeded the additional engine losses including pumping and sub-optimal combustion phasing.

A steady-state drive cycle estimation of FC improvements with the eTG expander on both the turbocharged and supercharged engines showed that heavier vehicles benefit more from the eTG addition than lighter ones. The Ford Escape benefited more from the addition of the eTG than the Fusion on the city, highway and US06 drive cycles regardless of the boosting method used. Both supercharged vehicles benefited more from the addition of the eTG than their turbocharged counterparts over the city (FTP) and US06 cycles. The opposite was observed on the highway cycle. Also, both vehicles benefited more on the US06 (up to 4.6%) than the less aggressive city and highway cycles (up to 0.9% and 2.0% respectively).

The overall benefit from replacing the turbocharger with a power split supercharger (PSS) was evaluated as well. The PSS with eTG was the better boosting-WHR combination providing higher brake system efficiency over most of the engine map, and larger drive cycle FC improvement than the turbocharger-eTG configuration. Replacing the turbocharger with a PSS along with the addition of the eTG reduced FC by up to 1.4%, 2.4% and 4.6% over the city, highway and US06 drive cycles. Improving the eTG efficiency from 60% to 80% roughly doubled the FC reductions for the FTP and highway cycles to 2.7% and 4.7%.

Experimental validation of the simulation results were performed. Due to the unexpectedly low expander efficiencies ($< 20\%$) observed for provided prototype, the eTG was detrimental for most of the tested points. The largest improvement in system brake efficiency was only 0.4%.

CHAPTER VII

Conclusions and Future Work

7.1 EGR Estimation

The first part of this work addresses the EGR estimation problem. Cooled external EGR on production spark ignition (SI) engines has only achieved limited market penetration despite its well established efficiency benefits. While the accurate knowledge of EGR content in the intake manifold is crucial for emissions control, combustion stability and knock mitigation, EGR estimation is challenging especially at low differential pressures (ΔP) due to the pulsating nature of the flow. While some EGR systems are capable of increasing the ΔP across the EGR valve or orifice, this can limit the overall EGR benefit. It is therefore desirable to improve EGR estimation accuracy at the low differential pressures.

The biggest contributor to the EGR estimation error is the non-linearity error. The orifice equation is highly non-linear especially at the low ΔP. Conventional averaged and/or slow-sampled pressure measurements result in a large flow error. GT-Power simulations of a low pressure (LP) and a high pressure (HP) EGR systems added to the Ford 1.6 L EcoBoost engine show EGR estimation errors up to $\approx 30\%$ and $\approx 12\%$ respectively. To keep the EGR estimation error within a target $\pm 1\%$, the average differential pressure across the EGR valve ($\overline{\Delta P}$) should be kept above 10.1 and 9.2 kPa for the LP and HP-EGR systems respectively. The target error bound of $\pm 1\%$ is mainly dictated by accuracy requirement on air-charge estimation for emissions control.

To avoid the non-linearity error, fast-sampling of measured signals is required. The analysis in this work shows that fast-sampling of the ΔP signal is sufficient to eliminate the non-linearity error. Averaging of remaining signals: EGR valve inlet and outlet temperatures, and outlet pressures has negligible impact on the EGR estimation accuracy. However, if two inlet and outlet pressure sensors are used

instead, then both sensors need to be fast-sampled. A ΔP sampling frequency of at least 1 kHz is required. Simulation results show reductions in $\overline{\Delta P}$ lower bound required for LP and HP-EGR estimation errors within $\pm 1\%$ to 1.4 and < 1.5 kPa respectively. Experimental studies performed show a similar trend. With a sampling frequency of at least 1 kHz, the LP and HP $\overline{\Delta P}$ lower bound can be reduced from 12.7 and 27.9 to 1.9 and 2.9 kPa respectively.

To further reduce the $\overline{\Delta P}$ lower bound, the flow formulation needs to account for the inertial effects. To that end, an unsteady compressible flow orifice equation was derived. Various assumptions to simplify the unsteady orifice equation were evaluated using the GT-Power simulation data. The derived unsteady flow formulation achieves an EGR estimation error withing $\pm 1\%$ for all the simulated $\overline{\Delta P}$ for both EGR systems.

The unsteady orifice equation involves solving a first order non-linear dynamic system, so approximating the unsteady formulation with a quasi-steady orifice equation and low pass filtered ΔP is considered. The lag of a first order low-pass filter with a variable bandwidth is shown to approximate the inertial lag. The variable bandwidth is shown to be dependent on valve area and ΔP. Experimental data shows that the $\overline{\Delta P}$ lower bound for the LP-EGR case can be reduced from 1.9 to 1.1 kPa. No improvement is observed for the HP-EGR case. This can be due to the larger measurement errors as a result of the using inlet and outlet pressure sensors instead of a ΔP sensor.

Another possible source of error that can affect the EGR estimation is the gauge-line distortion of the pressure signal. Various pressure frequency component can be amplified or attenuated based on the gauge-line lengths and the pulsation frequency. The impact of gauge-line errors was evaluated using GT-Power simulations for the LP-EGR case. Gauge-line lengths under 10 cm have insignificant effect on the EGR estimation accuracy; however, 30 cm gauge-lines increase the $\overline{\Delta P}$ lower bound required to keep the LP-EGR estimation error within $\pm 1\%$ from 1.4 to 10.9 kPa. A method based on a 2^{nd} order lumped parameter to correct for the gauge-line distortions was proposed and evaluated. The proposed correction method can reduce the $\overline{\Delta P}$ lower bound back to 1.4 kPa in the presence of ± 0.25 kPa measurement noise. With higher noise of ± 0.5 and ± 1 kPa, the $\overline{\Delta P}$ lower bound can be only reduced to 1.7 and 2.3 kPa respectively.

Finally, changes over time in the valve area due to the accumulation of carbon deposits can be detrimental to the EGR estimation accuracy. These changes can be modeled as area offset errors. Unlike all the previously discussed errors, area offset

errors are especially detrimental at the higher ΔP's as EGR valve is forced into low lift operation. At such low lifts, a thin layer of deposits can cause a large relative change in the area. Simulation studies on the HP-EGR system show that a small area offset error of 0.02 mm result in EGR estimation error greater than $\pm 1\%$ at $\overline{\Delta P}$'s higher than ≈ 10 kPa.

Imposing a lower bound on lift to avoid low lift operation causing unacceptable EGR estimation errors for a 0.02 mm area offset prevents EGR operation at low to mid-loads for the HP-EGR system. An online calibration method for the HP-EGR valve area was developed and assessed. The proposed method uses the preexisting intake manifold pressure sensor. Transfer functions relating the intake manifold pressure to the actual HP-EGR valve area for some given throttle position are first generated. Intake pressure measurements taken during deceleration fuel shut-off events can be then used to recalibrate the HP-EGR valve area online.

7.1.1 Future Work

While the LP-EGR and HP-EGR case studies in this work considered a pressure measurement across the EGR valve, the analysis of non-linearity errors, inertial errors, measurement errors and gauge-line distortions is also applicable to the more conventional case with a ΔP across an EGR orifice. Sizing of EGR orifices involves a trade-off between having a sufficiently small orifice area that results in $\overline{\Delta P}$ above the lower bound required for accurate EGR estimation at low EGR flows, and sufficiently large orifice area that does not restrict EGR flow at higher engine speeds and loads. Future studies can apply the outcomes of this work to reduce the minimum $\overline{\Delta P}$ requirement for an orifice which allows for more optimal orifice sizing.

Using a pressure measurement across the EGR valve instead of an orifice eliminates the orifice sizing trade-off. However, the regions with high $\overline{\Delta P}$ restrict the valve operation to small opening areas where the sensitivity of the EGR estimation error to area offset errors is significantly increased. On a LP-EGR system, such high $\overline{\Delta P}$ can be avoided by keeping the air intake system (AIS) throttle near wide-open given the estimation algorithm enables accurate estimation at the low ΔP. However, throttled SI engine operation imposes high $\overline{\Delta P}$ across the EGR valve in a HP-EGR system. As a result, the high $\overline{\Delta P}$ cannot be avoided unless advanced engine technologies like variable valve lift (VVL) are used. An online calibration algorithm for the HP-EGR valve area is crucial.

The proposed online calibration method in this work requires no additional engine sensors. The analysis performed shows potential for implementation. More validation

work with actual aged valves is required however. It should be noted here that area errors can also result from the inaccuracy of the valve actuation mechanism. Even if the proposed online calibration method can detect and correct for small area changes, the benefit of these corrections cannot be achieved if the resolution and accuracy of the valve actuation does not allow valve opening area control to the required precision.

7.2 Waste Heat Recovery

The second part of this work is focused on waste heat recovery (WHR) on SI engines using electric turbo-generation (eTG). While more than 30% of the fuel energy is lost though the engine exhaust, WHR studies show minor fuel economy (FE) improvement, if any, on light duty application. GT-Power simulations were performed to evaluate the WHR potentials on the Ford 1.6 L EcoBoost engine. Considerable relative system efficiency improvements up to 5% can be achieved. Unfortunately, such improvements are obtained at mid loads high speeds. Smaller, even negative, system efficiency changes are observed at the more frequently visited lower speeds and loads. Steady-state drive cycle analysis show FE improvements slightly higher than 1%. The projected FE gain can barely offset the impact of the eTG's added weight.

An engine ideal cycle analysis was performed to better understand the tradeoffs involved. While such analysis cannot capture negative impact of the eTG on high load knock due the higher trapped residuals, it can give useful insights into the main tradeoff between the additional engine pumping losses and the recovered exhaust energy present at highly visited engine operation points. For a given increase in exhaust back pressure at a given engine speed, the increase in pumping power is independent of load. However, the eTG power is an increasing function in load. An isentropic expander recovers sufficient power to offset the additional pumping losses at all loads. Unfortunately, the power from an expander with realistic efficiencies can only exceed the additional pumping at the mid to high loads.

Experimental validation of the simulation and analytical results were performed. Due to the unexpectedly low expander efficiencies ($< 20\%$) observed for provided prototype, the eTG was detrimental for most of the tested points. The largest improvement in system brake efficiency was only 0.4%.

7.2.1 Future Work

The analytical study performed along with the sensitivity analysis of the FE improvements to the expander efficiency show the need for higher efficiencies for WHR using eTG in series configuration for it to be a viable technology. Future research on this topic may focus on improving the current device efficiencies or on alternative WHR technologies and configurations that impose smaller pumping losses, or any other efficiency penalty, in the first place. Potential improvements with EGR resulting in the higher WHR expander flow rates are also worth investigating.

BIBLIOGRAPHY

BIBLIOGRAPHY

[1] "Federal vehicle standards," https://www.c2es.org/content/regulating-transportation-sector-carbon-emissions/, Accessed: 2018-04-03.

[2] "Sources of greenhouse gas emissions," https://www.epa.gov/ghgemissions/sources-greenhouse-gas-emissions, Accessed: 2018-04-03.

[3] "Greenhouse gas emissions from transport," https://www.eea.europa.eu/data-and-maps/indicators/transport-emissions-of-greenhouse-gases/transport-emissions-of-greenhouse-gases-11, Accessed: 2019-03-07.

[4] "Real-driving emissions in the euro 6 regulation on emissions from light passenger and commercial vehicles (rde3)," https://ec.europa.eu/info/law/better-regulation/initiatives/ares-2016-6339064_en, Accessed: 2019-03-07.

[5] T. Johnson and A. Joshi, "Review of vehicle engine efficiency and emissions," *SAE International Journal of Engines*, vol. 11, no. 2018-01-0329, 2018.

[6] S. Pischinger, "The future of vehicle propulsion–combustion engines and alternatives," *Topics in catalysis*, vol. 30, no. 1-4, pp. 5–16, 2004.

[7] A. Alagumalai, "Internal combustion engines: Progress and prospects," *Renewable and Sustainable Energy Reviews*, vol. 38, pp. 561–571, 2014.

[8] L. Teodosio, V. De Bellis, and F. Bozza, "Fuel economy improvement and knock tendency reduction of a downsized turbocharged engine at full load operations through a low-pressure EGR system," *SAE Technical Paper*, no. 2015-01-1244, 2015.

[9] D. Takaki, H. Tsuchida, T. Kobara, M. Akagi, T. Tsuyuki, and M. Nagamine, "Study of an EGR system for downsizing turbocharged gasoline engine to improve fuel economy," *SAE Technical Paper*, no. 2014-01-1199, 2014.

[10] K. Kumano and S. Yamaoka, "Analysis of knocking suppression effect of cooled EGR in turbo-charged gasoline engine," *SAE Technical Paper*, no. 2014-01-1217, 2014.

[11] B. Hoepke, S. Jannsen, E. Kasseris, and W. K. Cheng, "EGR effects on boosted SI engine operation and knock integral correlation," *SAE Technical Paper*, no. 2012-01-0707, 2012.

[12] M. Kaiser, U. Krueger, R. Harris, and L. Cruff, ""doing more with less"-the fuel economy benefits of cooled EGR on a direct injected spark ignited boosted engine," *SAE Technical Paper*, no. 2010-01-0589, 2010.

[13] T. Alger, T. Chauvet, and Z. Dimitrova, "Synergies between high EGR operation and GDI systems," *SAE Technical Paper*, no. 2008-01-0134, 2008.

[14] S. Potteau, P. Lutz, S. Leroux, S. Moroz, and E. Tomas, "Cooled EGR for a turbo SI engine to reduce knocking and fuel consumption," *SAE Technical Paper*, no. 2007-01-3978, 2007.

[15] S. Chu and A. Majumdar, "Opportunities and challenges for a sustainable energy future," *Nature*, vol. 488, no. 7411, p. 294, 2012.

[16] Y. Ismail, D. Durrieu, P. Menegazzi, P. Chesse, and D. Chalet, "Potential of exhaust heat recovery by turbocompounding," *SAE Technical Paper*, no. 2012-01-1603, 2012.

[17] R. Dijkstra, M. Boot, R. Eichhorn, D. Smeulders, J. Lennblad, and A. Serrarens, "Experimental analysis of engine exhaust waste energy recovery using power turbine technology for light duty application," *SAE International Journal of Engines*, vol. 5, no. 2012-01-1749, pp. 1729–1739, 2012.

[18] F. Westin, B. Grandin, and H.-E. Ångström, "The influence of residual gases on knock in turbocharged SI-engines," *SAE Technical Paper*, no. 2000-01-2840, 2000.

[19] J. P. Szybist, S. W. Wagnon, D. Splitter, W. J. Pitz, and M. Mehl, "The reduced effectiveness of egr to mitigate knock at high loads in boosted si engines," *SAE International Journal of Engines*, vol. 10, no. 5, pp. 2305–2318, 2017.

[20] L. Zhong, M. Musial, R. Reese, and G. Black, "EGR systems evaluation in turbocharged engines," *SAE Technical Paper*, no. 2013-01-0936, 2013.

[21] J. B. Heywood, *Internal combustion engine fundamentals*. Mcgraw-Hill New York, 1988.

[22] P. M. Azzoni, G. Minelli, D. Moro, and G. Serra, "A model for egr mass flow rate estimation," *SAE Technical Paper*, no. 970030, 02 1997. [Online]. Available: http://dx.doi.org/10.4271/970030

[23] F. Liu and J. Pfeiffer, "Estimation algorithms for low pressure cooled egr in spark-ignition engines," *SAE International Journal of Engines*, vol. 8, no. 2015-01-1620, 2015.

[24] T. Brewbaker, "Multivariable diesel low-pressure EGR controller designed by input-output linearization," in *American Control Conference (ACC), 2015*, July 2015, pp. 31–37.

[25] D. Pachner and J. Beran, "Comparison of sensor sets for real-time egr flow estimation," *SAE Technical Paper*, no. 2016-01-1064, 04 2016.

[26] F. Liu, J. M. Pfeiffer, R. Caudle, P. Marshall, and P. Olin, "Low pressure cooled egr transient estimation and measurement for an turbocharged si engine," *SAE Technical Paper*, no. 2016-01-0618, 04 2016.

[27] K. Siokos, R. Koli, and R. Prucka, "Short-term and long-term adaptation algorithm for low-pressure exhaust gas recirculation estimation in spark-ignition engines," *International Journal of Engine Research*, p. 1468087418758492, 2018.

[28] R. McKee, "Pulsation effects on orifice metering considering primary and secondary elements," *Proc. of the 22nd Gulf Coast Measurements Short Course*, pp. 112–118, 1989.

[29] A. Patterson, R. Tett, and J. McGuire, "Exhaust heat recovery using electro-turbogenerators," *SAE Technical Paper*, no. 2009-01-1604, 2009.

[30] D. Hountalas, C. Katsanos, and V. Lamaris, "Recovering energy from the diesel engine exhaust using mechanical and electrical turbocompounding," *SAE Technical Paper*, no. 2007-01-1563, 2007.

[31] D. A. Arias, T. A. Shedd, and R. K. Jester, "Theoretical analysis of waste heat recovery from an internal combustion engine in a hybrid vehicle," *SAE Technical Paper*, no. 2006-01-1605, 2006.

[32] G. He and H. Xie, "Fuel saving potential of different turbo-compounding systems under steady and driving cycles," *SAE Technical Paper*, no. 2015-01-0878, 2015.

[33] M. C. Brands, J. R. Werner, and J. L. Hoehne, "Vehicle testing of cummins turbocompound diesel engine," *SAE Technical Paper*, no. 810073, 1980.

[34] D. Wilson, "The design of a low specific fuel consumption turbocompound engine," no. 860072, 1986.

[35] A. Teo Sheng Jye, A. Pesiridis, and S. Rajoo, "Effects of mechanical turbo compounding on a turbocharged diesel engine," no. 2013-01-0103, 2013.

[36] B. David P, F. Ana C, R. Michael G, and S. Dean J, "Effectiveness of mechanical turbo compounding in a modern heavy-duty diesel engine," *International Journal of Automotive Engineering*, vol. 3, no. 2, pp. 69–73, 2012.

[37] I. Briggs, G. McCullough, S. Spence, R. Douglas, R. O'Shaughnessy, A. Hanna, C. Rouaud, and R. Seaman, "Waste heat recovery on a diesel-electric hybrid bus using a turbogenerator," *SAE Technical Paper*, no. 2012-01-1945, 2012.

[38] P. Lu, C. Brace, and B. Hu, "Explore and extend the effectiveness of turbo-compounding in a 2.0 litres gasoline engine," *SAE Technical Paper*, no. 2015-01-1279, 2015.

[39] A. M. Mamat, A. Romagnoli, and R. F. Martinez-Botas, "Characterisation of a low pressure turbine for turbocompounding applications in a heavily downsized mild-hybrid gasoline engine," *Energy*, vol. 64, pp. 3–16, 2014.

[40] P. Gajan, R. Mottram, P. Hebrard, H. Andriamihafy, and B. Platet, "The influence of pulsating flows on orifice plate flowmeters," *Flow Measurement and instrumentation*, vol. 3, no. 3, pp. 118–129, 1992.

[41] K. Doblhoff-Dier, K. Kudlaty, M. Wiesinger, and M. Gröschl, "Time resolved measurement of pulsating flow using orifices," *Flow Measurement and Instrumentation*, vol. 22, no. 2, pp. 97–103, 2011.

[42] E. M. Greitzer, "Surge and rotating stall in axial flow compressors Part I: Theoretical compression system model," *Journal of Engineering for Gas Turbines and Power*, vol. 98, no. 2, pp. 190–198, 1976.

[43] F. Nagao and M. Ikegami, "Errors of an indicator due to a connecting passage," *Bulletin of JSME*, vol. 8, no. 29, pp. 98–108, 1965.

[44] *GT-Power: Flow Theory Manual*, Version 7.5 ed.

[45] F. Bonatesta, B. Waters, and P. Shayler, "Burn angles and form factors for wiebe function fits to mass fraction burned curves of a spark ignition engine with variable valve timing," *International Journal of Engine Research*, vol. 11, no. 2, pp. 177–186, 2010.

[46] J. Livengood and P. Wu, "Correlation of autoignition phenomena in internal combustion engines and rapid compression machines," in *Symposium (International) on combustion*, vol. 5, no. 1. Elsevier, 1955, pp. 347–356.

[47] R. J. Middleton, O. G. H. Gupta, H.-Y. Chang, G. Lavoie, and J. Martz, "Fuel efficiency estimates for future light duty vehicles, part a: Engine technology and efficiency," no. 2016-01-0906, 2016.

[48] L. Guzzella and C. Onder, *Introduction to modeling and control of internal combustion engine systems*. Springer Science & Business Media Berlin, 2009.

[49] R. Holmbom and L. Eriksson, "Analysis and development of compact models for mass flows through butterfly throttle valves," no. 2018-01-0876, 2018.

[50] P. Andersson, *Air charge estimation in turbocharged spark ignition engines*. Department of Electrical Engineering, Linköping University, 2005.

[51] R. Kiwan, A. Stefanopoulou, J. Martz, G. Surnilla, I. Ali, and D. Styles, "Effects of differential pressure sensor gauge-lines and measurement accuracy on low pressure egr estimation error in si engines," *SAE Technical Paper*, no. 2017-01-0531, 2017.

[52] K. Botros, W. Jungowski, and G. Petela, "Gauge line effects and dp transmitter response to flow pulsation through orifice plate," *Flow Measurement and Instrumentation*, vol. 3, no. 3, pp. 130–144, 1992.

[53] S. Nazari, J. Siegel, and A. Stefanopoulou, "Control of hybrid boosting in highly diluted internal combustion engines," *Submitted to IEEE transactions on control systems technology*, 2018.

[54] R. J. Middleton, "Voronoi partitions for assessing fuel consumption of advanced technology engines: An approximation of full vehicle simulation on a drive cycle," *SAE Technical Paper*, no. 2018-01-0317, 2018.

[55] R. Kiwan, R. Middleton, and A. Stefanopoulou, "Thermodynamic and practical benefits of waste energy recovery using an electric turbo-generator under different boosting methods," *SAE Technical Paper*, no. 2018-01-0851, 2018.

[56] S. Nazari, R. J. Middleton, K. Sugimori, J. Siegel, and A. G. Stefanopoulou, "Assessing a hybrid supercharged engine for highly diluted combustion using a dynamic drive cycle simulation," *SAE Technical Paper*, no. 2018-01-0969, 2018.

[57] R. J. Middleton, J. B. Martz, G. A. Lavoie, A. Babajimopoulos, and D. N. Assanis, "A computational study and correlation of premixed isooctane air laminar reaction fronts diluted with egr," *Combustion and Flame*, vol. 159, no. 10, pp. 3146–3157, 2012.

[58] S. Nazari, R. Kiwan, J. Siegel, and A. Stefanopoulou, "Waste energy recovery through turbo generation: "unexpected fuel efficiency sweet spot for transient calibration."," in *American Control Conference (ACC), 2018*, 2018.